Superparamagnetic Beads as Self-Assembling Matter for Microfluidic Applications

Bielefeld University

Bernhard Eickenberg

February 14, 2014

Declaration of authorship

I hereby certify that the work presented in this dissertation is my original work and that all passages and ideas that are not mine have been fully and properly acknowledged.

Bielefeld, February 14, 2014 Bernhard Eickenberg

Reviewers

Prof. Dr. Andreas Hütten

Prof. Dr. Dario Anselmetti

"Teach thy tongue to say, 'I do not know,' and thous shalt progress."

Maimonides

"The most exciting phrase to hear in science, the one that heralds new discoveries, is not 'Eureka!' but 'That's funny...'"

Isaac Asimov

Contents

1 Introduction 5

2 Theory 13
- 2.1 Microfluidics . . . 13
  - 2.1.1 From the macroscopic to the microscopic . . . 13
  - 2.1.2 Fluid flow on the micro scale . . . 15
  - 2.1.3 Pressure-Driven Flow Profile . . . 17
  - 2.1.4 Mixing on the micro scale . . . 19
- 2.2 Magnetism . . . 21
  - 2.2.1 Magnetism on the nano scale . . . 22
  - 2.2.2 Beads . . . 23
- 2.3 Optical Detection . . . 31
  - 2.3.1 Absorption Spectroscopy . . . 31
  - 2.3.2 Raman Scattering . . . 32
  - 2.3.3 Surface Enhanced Raman Scattering . . . 35

3 Materials and Methods 41
- 3.1 Lithography . . . 41
- 3.2 Microfluidic Flow . . . 46
- 3.3 Optical Microscopy . . . 46
- 3.4 Magnetic Field . . . 46
- 3.5 Raman Spectroscopy . . . 51
- 3.6 Superparamagnetic Beads . . . 52

4 SPS Formation Dynamics 55
- 4.1 Materials and Methods . . . 56
- 4.2 Experiments . . . 56
  - 4.2.1 Evaluation of the Initial SPS Formation . . . 57

4.2.2 Evaluation of the Frequency Threshold 58
4.2.3 Reformation of Chain-like SPS from Clusters 58
4.3 Results and Discussion 59
4.3.1 Evaluation of the Initial SPS Formation 59
4.3.2 Evaluation of the Frequency Threshold 64
4.3.3 Reformation of Chain-like SPS from Clusters 69
4.4 Conclusion 73
4.5 Outlook 74

5 Utilizing SPS structures for colloidal separation and enhanced mixing 77
5.1 Materials and Methods 79
5.2 Experiments 81
5.2.1 Guiding and Separation Efficiency 82
5.2.2 Mixing Efficiency 83
5.2.3 Free-Flowing SPS for Particle Separation 84
5.3 Results and Discussion 84
5.3.1 Guiding and Separation Efficiency 84
5.3.2 Free-Flowing SPS for Particle Separation 97
5.3.3 Mixing Efficiency 99
5.3.4 Comparison with Magnetophoresis 100
5.4 Conclusion 102
5.5 Outlook 104

6 DNA Bridges as Bead-Bead Interconnections 105
6.1 Materials and Methods 109
6.2 Experiments 109
6.2.1 Binding DNA to the Bead Surface 110
6.2.2 Monolayer Formation 110
6.2.3 Evaluation of the DNA Binding Strength 111
6.3 Results and Discussion 112
6.3.1 Binding DNA to the Bead Surface 112
6.3.2 Monolayer Formation 113
6.3.3 Evaluation of the DNA Binding Strength 115
6.4 Conclusion 117
6.5 Outlook 117

7 SPS chains as Switchable Filtration Network 119
7.1 Materials and Methods . . . 121
7.2 Experiments . . . 121
7.2.1 Preparation of APTES spots . . . 122
7.2.2 Anchoring of Chains and Switching Procedure . . . 123
7.3 Results and Discussion . . . 123
7.4 Conclusion . . . 125
7.5 Outlook . . . 126

8 Beads for Surface Enhanced Raman Spectroscopy 127
8.1 Materials and Methods . . . 130
8.2 Experiments . . . 131
8.2.1 Fabrication of gold-nanoparticle covered beads . . . 131
8.3 Results and Discussion . . . 133
8.4 Conclusion . . . 144
8.5 Outlook . . . 144

9 Summary 147

Bibliography 155

List of Publications

Reviews

- B. Eickenberg, J. Meyer, L. Helmich, D. Kappe, A. Auge, A. Weddemann, F. Wittbracht, A. Hütten: *Lab-on-a-Chip Magneto-Immunoassays: How to Ensure Contact between Superparamagnetic Beads and the Sensor Surface.* Biosensors, **3** (2013), 327-340.

Paper

- B. Eickenberg, F. Wittbracht, P. Stohmann, J.R. Schubert, C. Brill, A. Weddemann, A. Hütten: *Continuous-flow particle guiding based on dipolar coupled magnetic superstructures in rotating magnetic fields.* Lab on a Chip, **13** (2013), 920-927.
- F. Wittbracht, A. Weddemann, B. Eickenberg, A. Hütten: *On the direct employment of dipolar particle interaction in microfluidic systems.* Microfluidics and Nanofluidics, **13** (2012), 543-554.
- F. Wittbracht, A. Weddemann, B. Eickenberg, M. Zahn, A. Hütten: *Enhanced fluid mixing and separation of magnetic bead agglomerates based on dipolar interaction in rotating magnetic fields.* Applied Physics Letters, **100** (2012), 123507.
- F. Wittbracht, B. Eickenberg, A. Weddemann, A. Hütten: *Towards a programmable microfluidic valve: Formation dynamics of two-dimensional magnetic bead arrays in transient magnetic fields.* Journal of Applied Physics, **109** (2011), 114503.
- A. Weddemann, F. Wittbracht, B. Eickenberg, A. Hütten: *Magnetic Field Induced Assembly of Highly Ordered Two-Dimensional Particle Arrays.* Langmuir, **26** (2010), 19225-19229.

Conference Paper

- B. Eickenberg, F. Wittbracht, A. Hütten, A. Weddemann: *Microfluidic gate - Utilization of Self-Assembling, Free-Flowing Superstructures of Superparamagnetic Beads for Enhanced Mixing and Colloidal Separation.* ICQNM (2011), Nice, France.

- F. Wittbracht, B. Eickenberg, A. Hütten, A. Weddemann: *Rotating magnetic field assisted formation of highly ordered two-dimensional magnetic bead arrays.* ICQNM (2011), Nice, France.

Poster Presentations

- B. Eickenberg, M. Bartke, F. Wittbracht, P. Stohmann, A. Weddemann, A. Hütten: *Superparamagnetic microbeads as reconfigurable, self-assembling components for Lab-on-a-Chip applications.* Fifth Seeheim Conference on Magnetism (2013), Frankfurt a.M., Germany.

- B. Eickenberg, F. Wittbracht, A. Weddemann, P. Stohmann, A. Hütten: *Superparamagnetic microbeads as reconfigurable, self-assembling components for Lab-on-a-Chip applications.* EMBL Conference on Microfluidics (2012), Heidelberg, Germany.

- B. Eickenberg, F. Wittbracht, A. Weddemann, A. Hütten: *Microfluidic gate using self-assembling superstructures of superparamagnetic beads.* PDG Spring Meetings (2011), Dresden, Germany.

Conference Talks

- B. Eickenberg, F. Wittbracht, A. Hütten, A. Weddemann: *Microfluidic gate - Utilization of Self-Assembling, Free-Flowing Superstructures of Superparamagnetic Beads for Enhanced Mixing and Colloidal Separation.* ICQNM 2011, Nice, France.

- F. Wittbracht, B. Eickenberg, A. Hütten, A. Weddemann: *Rotating magnetic field assisted formation of highly ordered two-dimensional magnetic bead arrays.* ICQNM 2011, Nice, France.

In Preparation

- B. Eickenberg, M. Bartke, F. Wittbracht, A. Hütten: *DNA-Mediated Stabilization of Self-Assembling Bead Monolayers for Microfluidic Applications.*

1 Introduction

For decades, science fiction authors and script writers have presented us with medical devices that are able to automatically analyse infections, genomes and cardiac conditions within seconds. Most of these devices can be handheld and offer multiple analysis functions so that they serve as an all-purpose device. In medical terminology, such a tool is referred to as point-of-care device - a machine that analyses samples taken directly from a patient, making a transport to a central laboratory obsolete. With such devices, medical treatment of an illness could start immediately subsequent to the check-up procedure. Patients wouldn't have to wait days for test results before medication can be adjusted or illnesses determined. Central laboratories with expensive technical staff could be exchanged for medical staff that visits patients at home. Medical examinations would be faster, cheaper and more readily available than it is currently the case. But how close is our society to actually constructing such a tool?

Over the last decades, in many fields of research and construction the actual development of the technology has been faster than initially imagined, e.g. in the field of computer technology. Today, tools like mobile phones, talking computers and touchscreens that were depicted in works of science fiction long before they were invented, exist as everyday devices. Miniaturization of electromechanical systems has been extremely rapid, leading to the development of *microelectromechanical systems* (*MEMS*) in the 80s. Although the scientific field of MEMS provided little advancement in the medical sector, it was the first big step towards system miniaturization. Within the following decade, mechanical, fluid, electromechanical and thermal systems in the size range of a few micrometers became available.

During the 90s, the miniaturization of fluidic devices grew into a separate scientific field called *microfluidics*, bringing with it the development of so-called *lab-on-a-chip* devices. These chip systems enabled the handling

and analysis of nanoliter liquid samples and gave rise to new methods for biochemical and biomedical analysis and research.

One huge step towards the realization of point-of-care devices was done in 1990, when Manz, Graber and Widmer proposed a so-called *miniaturized* (or *micro-*) *total analyis system* (*μ-TAS*)[1] that transforms chemical information into electronic information which can be read out by a computer software. In this chip-sized system, they envisioned, sampling, sample transport, chemical reactions, chromatographic separation and detection would be carried out automatically. Manz *et al.* predicted several advantages of such systems, e.g. reduced analysis times, increased separation performance for chromatography applications, faster diffusive mixing and the ability for simultaneous analysis in multi-channel systems. These advantages are mainly created by system miniaturization. Smaller volumes, areas and length scales significantly change the equilibrium between different forces like van-der-Waals, gravity or capillary forces and influence processes like diffusion and fluid flow.

The first μ-TAS device was realized in 1994 by Jacobson *et al.*[2] who succeeded in incorporating enzymatic reaction, separation and detection in a single etched glass microchip. Their system operated on a time-scale of a few seconds. Since then, further applications have been realized on-chip, such as DNA sequencing, polymerase chain reaction (PCR), electrophoresis, immunoassays, cell counting and cell sorting[3,4,5]. The initial use of glass as the chip material has been exchanged for polymer materials that allow for rapid prototyping and mass production, mainly polydimethylsiloxane (*PDMS*)[5,6,7,8].

Today, a large variety of separation and detection methods for a broad range of biomedical applications is available. Numerous large-scale analysis schemes have been successfully miniaturized. However, the number of lab-on-a-chip and μ-TAS [1] devices that has been successfully introduced into the market is still rather small[9,10,11,12]. There are two main reasons

1 The term lab-on-a-chip is often used synonymous for μ-TAS, although the field of lab-on-a-chip systems is much broader and also incorporates microfluidic devices that execute tasks other than analysis, e.g. mixing, separation or chemical synthesis.

why most microfluidic analysis devices are not suitable for mass production, yet:

- **On-chip sample preparation:** Sample preparation is a crucial step for all analysis procedures. As today's detection methods are extremely sensitive, every trace amount of a contamination will alter the analysis result. Thus, a careful preparation of the sample is necessary to ensure reliable results that are especially important for medical applications. For large-scale laboratory analyses, standard protocols exist. However, these protocols are often quite complex and are not easily transferred to lab-on-a-chip systems. Thus, sample preparation often has to be carried out off-chip. Furthermore, creating a suitable chip-environment interface is still a challenge, as real-life samples often include impurities that can obstruct micrometer sized channels. To achieve economically viable devices, solutions for suitable interfaces and on-chip sample preparation have to be found.

- **High production costs:** Most analysis schemes that can be carried out in lab-on-a-chip devices can be carried out in traditional large-scale setups as well. The facilities for these analyses already exist, thus µ-TAS have to offer specific advantages to replace them. The most important advantage would be a significant reduction in the costs of analysis. However, although the theoretical concept of µTAS offers this and further advantages, most state-of-the-art µ-TAS that exist now are complex structures that require 3D structuring and multiple assembly steps. As µTAS are usually single-use devices, the current devices are too expensive for mass production and therefore cannot commercially compete with established standard methods. Thus, a reduction in device complexity must be achieved to ensure the market success of µ-TAS[12].

Superparamagnetic beads offer a way to simplify sample preparation and reduce production costs at the same time and could thus help to make microfluidic systems viable for the medical market. Beads are micrometer-sized particles that consist of superparamagnetic nanoparticles that are incorporated in a polymer matrix (see Figure 2.4 for a sketch of the bead

structure). On the surface of this polymer matrix, ligands such as proteins, reactive chemical groups or oligonucleotides can be immobilized. This way, the beads can be used to bind to biomolecules, cells or other possible analytes present in solution.

The superparamagnetic character of beads (for details, see section 2.2) allows to switch the magnetic behavior of these particles on or off by applying or removing an external magnetic field. Thus, in the absence of a field the particles behave non-magnetically. In the presence of a magnetic field, they can be manipulated like magnetic material, i.e. they can be agglomerated or moved into the direction of a magnetic gradient (*magnetophoresis*).

So far, beads have been used for large scale laboratory and microfluidic applications. In standard large scale analysis they are usually used to label analyte molecules and then quickly separate them from a sample by the use of a magnetic field gradient, e.g. supplied by a permanent magnet. In lab-on-a-chip systems, they have mainly been used to act as a solid support for biochemical reactions[13,14,15] or to separate biomolecules or cells via magnetophoresis[16,17,18,19,20]. In the latter case, beads are bound to the analyte molecules, either on-chip within microfluidic systems or in an off-chip preparation vial. Magnetic gradient fields are then used to separate the analyte molecules from the remaining sample and analyze them with a suitable detection scheme, e.g. fluorescence spectroscopy. This way, beads can simplify the sample preparation off-chip or on-chip, as complex separation procedures like chromatographic separation become obsolete, thus lowering the device complexity.

Apart from separation *via* magnetophoresis, beads offer another advantage: They can be detected with magnetoresistive (MR) sensors. These highly sensitive sensors, typically tunnel magnetoresistance (TMR) sensors[21,22], giant magnetoresistance (GMR) sensors[23,24,25,26,27,28], spin valves[29,30,31] or Hall sensors[32], detect a change in resistance that is caused by a magnetic field. Due to recent technological advances and the invention of a GMR ink they can even be printed[33], making complex lithographic assembly steps unnecessary.

Through the use of MR sensors, beads can be used as labels for detection. Compared to classic fluorescent labels, beads offer a wide range of advantages:

- Unlike fluorescent labels, beads are stable over time. Effects equivalent to photobleaching do not occur.
- MR detection does not require complex off-chip instrumentation.
- There is no magnetic background from the sample.
- Magnetic fields do not influence the sample or the analyte molecules.
- The signal does not depend on parameters such as pH value or ionic strength.
- Aqueous media do not screen the signal.

The combination of beads and MR sensors has been successfully utilized for biochemical analysis multiple times[24,25,26,27,28,34,35,22,21]. However, beads have the potential to decrease the device complexity even further by using them as self-assembling matter in microfluidic systems.

Under the influence of magnetic fields, superparamagnetic beads assemble into one- or two-dimensional structures[36,37,38,39] within several seconds to minutes, depending of the parameters of the external field. The shape of these structures can roughly be influenced through the external field, i.e. the beads can be arranged in one-dimensional, chain-like structures (*chains*)[40,41,42] or two-dimensional, flat agglomerates (*clusters*)[43,44]. These structures have the potential to be used as self-assembling components within microfluidic devices. So far, such *supraparticle structures* (*SPS*)[45] have been utilized in lab-on-a-chip systems for the following applications:

- **Filter-like immunoassay substrates:** Lacharme *et al.*[38] used chain-like arrangements of beads as reaction substrates for sandwich immunoassays. They trapped the chains in grooves that were built in the channel walls and used these filter-like arrangements to capture target antibodies.
- **Particle flow control:** Weddemann *et al.*[46] utilized the orientation of 1D bead chains in magnetic fields to selectively block and open microfluidic channels for SPS flow.

- **Active mixing device:** Rida and Gijs[47] and Lee *et al.*[48] used agglomerates of beads for active mixing. In their setup, the particle agglomerates were rotated inside a mixing chamber through the use of external permanent magnets. Rida and Gijs used ferrimagnetic beads that were retained within a flow by a strong alternating magnetic field that induced rotational movement of the magnetic particles and therefore promoted mixing. While Lee *et al.* actually used ferromagnetic microparticles to act as stirring devices, the same principle could be applied to superparamagnetic beads.

- **Signal Enhancement:** Vuppu *et al.*[40] formed SPS chains in a rotating magnetic field. The beads had fluorescent markers bound to their surface. Using lock-in amplification of the fluorescence signal with the periodicity of the chain rotation, they were able to significantly increase the signal-to-noise ratio of the fluorescence detection.

- **Microfluidic pump:** Derk *et al.*[49] showed that magnetophoretic movement of beads and the resulting drag forces on the surrounding liquid can be used to induce fluid flow in narrow channels. On this basis, they developed a pumping mechanism for porous microsystems.

- **Extraction tools:** Karle *et al.*[17] used a combination of magnetophoresis and formation of rotating SPS in a rotating magnetic field for continuous DNA extraction. In their experiment, they had beads cross different parallel streams carrying the sample and diverse lysis, binding and washing buffer solutions. The rotational movement of the chains served primarily to keep beads from sticking to the channel walls.

- **Formation of monolayers:** Weddemann *et al.*[43] investigated the formation of highly ordered monolayers of beads under the influence of rotating magnetic fields. They exposed a concentrated bead solution to the rotating field of a permanent magnet. Under the influence of the magnetic field, 2D, disc-like SPS formed and combined into mm-sized monolayer sheets that showed very high, hexagonal ordering.

Although 1D, chain-like SPS have been extensively studied and used for microfluidic applications, as can be seen from the examples given above, 2D structures have hardly been investigated.

The objective of this work was to develop new applications for self-assembling SPS of superparamagnetic beads in microfluidic structures, with the aim of simplifying the device complexity and enable novel operations. In order to be able to achieve this goal, a deeper understanding of the formation process is necessary. For this, experiments revealing the formation dynamics of 1D and 2D SPS have been performed (chapter 4). In this context, a method to switch between the 1D chain-like shape and the 2D disc-like shape has been developed. Furthermore, possible applications of SPS in microfluidic systems have been designed and evaluated. In one of these applications, SPS have been utilized as free-flowing local mixing devices with simultaneous continuous-flow extraction (chapter 5). In another set of experiments, a method to reversibly solidify 2D monolayer structures *via* DNA double-strands that serve as bridges between the particles has been devised (chapter 6). In chapter 7, the formation of 1D chain-like SPS was used to create a switchable filtration network of chains anchored to the channel wall. Lastly, beads were used as solid support for surface-enhanced Raman scattering (SERS) detection with possible applications as local pH sensors (chapter 8).

2 Theory

In this chapter, the relevant theoretical background concerning the topics of this work will be given. Theoretical aspects of microfluidics, magnetism as well as absorption and Raman spectroscopy will be discussed. For a more detailed reading on these topics, the reader is referred to several reviews and books about the respective topics.

2.1 Microfluidics

In this section, the basic aspect of microfluidics - the miniaturization of flow conditions - and its implications will be presented. As modelling of microfluidic flows is not within the scope of this work, the Navier-Stokes-equation that describes the behaviour of flows will not be discussed here. For this, the reader is referred to other work [50,51,52,53]. However, a description of the most important characteristics of the flow behaviour within microfluidic systems, that can also be derived from the Navier-Stokes-equation, will be given.

2.1.1 From the macroscopic to the microscopic

Due to technical advances over the last decades, mechanical, electromechanical, thermal and fluid systems can be miniaturized down to a size scale in the micrometer or even nanometer range. As previously discussed, this has given rise to the development of microelectro-mechanical systems (MEMS) in the 80s and microfluidics in the 90s. However, MEMS and microfluidic devices are not simply a miniature version of their macroscopic counterparts. The miniaturization not only results in a reduced size, but also allows for better performance and new applications that are not achievable on the macroscopic scale [1].

The reason for this is not directly apparent: As molecules, intermolecular distances and intermolecular forces are generally on the size scale of nanometers, downscaling the device to a micrometric size should not change much in the behaviour of the scaled materials. Different from nanoparticles, where the properties of the material differ strongly from the bulk properties, micrometer systems can usually still be considered as bulk. The identity of single atoms or molecules can be neglected. Thus solid, fluid or even dense gaseous phases can be described as continuous phases in which properties like density, temperature and charge do not vary spatially. Even long-range interactions between surfaces, e.g. the electric double layer, can be considered localized as their length hardly exceeds 100 nm.

Instead, the relative importance of different forces changes from the macro- to the microscale[50,54]. As the size scale of the system decreases, the surface to volume ratio of the system increases significantly. Thus, forces that depend on the volume of the material, e.g. gravitation, lose importance, while surface forces such as capillary forces rapidly gain importance. Table 2.1 shows scaling laws for different forces[50,54]. These laws consider the general dependence of the force on the size scale l of the system[1]. As l declines, forces with a higher exponent lose importance compared to forces with a lower exponent.

For MEMS and microfluidic devices, these scaling laws have a strong impact on the device performance. Micropumps, for example, suffer from the increased influence of adhesion, as miniaturized valves tend so stick to the channel walls[54]. In general, the change in the influence of different forces may complicate or enable certain applications on the micrometer scale, thus making it necessary to tailor application-specific technology for miniaturized devices. A simple down-scaling of macroscopic devices does usually not suffice to ensure functionality.

1 In case of a microfluidic channel, l would depict the width and/or height of the channel, whichever is smaller.

Table 2.1: Scaling laws for different physical quantities[50,54]. l is the characteristic length scale of the system. The scaling law defines how strongly changes in l effect the given quantity. Quantities with a high exponent lose importance compared to quantities with lower exponents when the system is scaled down.

Physical quantity	Scaling law
Intermolecular Van der Waals force	l^{-7}
Capillary force	l^1
Hydrostatic pressure	l^1
Stokes drag	l^1
Reynolds number	l^2
Electrostatic force	l^2
Diffusion time	l^2
Area	l^2
Mass	l^3
Volume	l^3
Magnetic force with an exterior field	l^3
Magnetic force without an exterior field	l^4
Centrifugal force	l^4

2.1.2 Fluid flow on the micro scale

The reduction in channel size when going from macroscopic to microscopic channels has a very significant impact on the behaviour of the liquid flow. In general, two kinds of flow regimes can be distinguished: laminar flow and turbulent flow. The difference between these two regimes lies in whether viscous or inertial forces dominate the flow[54,55,56]. The ratio of these forces is generally expressed in form of the Reynolds number Re

$$Re = \frac{\rho u l}{\eta} \tag{2.1}$$

with ρ as the density and η as the viscosity of the liquid, u as the fluid

velocity and l as the characteristic length scale of the system.

Whether inertial or viscous forces are dominant significantly changes the flow behavior of the system (see Figure 2.1). If inertial forces dominate, i.e. Re is large, the flow becomes *turbulent*. Such a flow is characterized by a fluid particle movement that is random in both time and space. Hydrodynamic instabilities such as vortices result in a convective mass transport in all directions. If viscous forces dominate, i.e. Re is small, the flow becomes *laminar*. Fluid streams flow parallel and do not cross (see Figure 2.2). The velocity at a given location is constant in time, as long as the boundary conditions do not change. This results in a flow where convective mass transfer only occurs in direction of the flow. Thus, mixing between parallel streams can only be achieved through diffusion.

As can be seen from Table 2.1, the Reynolds number has a scaling law of l^2. Thus, miniaturization of a microfluidic system leads to a rapid decrease in Re. The result of this is that flows in microfluidic systems generally possess a $Re < 1$ and are therefore laminar. Turbulences like vortices do not occur, the fluid flow is smooth and stable over time. This leads to special requirements on microfluidic systems when mixing is concerned. These requirements will be discussed in section 2.1.4.

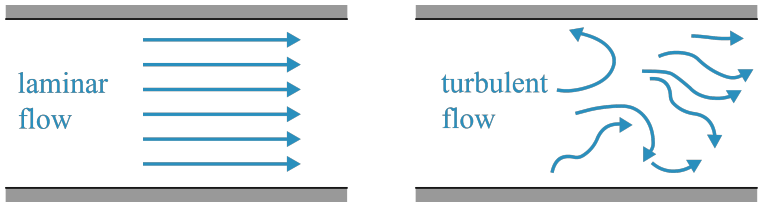

Figure 2.1: Flow regimes in liquid flow. In a *laminar flow* (left), viscous forces dominate. The flow is stationary and stream lines do not cross. In a *turbulent flow* (right), inertial forces dominate. Such a flow is characterized by a random movement of fluid particles and hydrodynamic instabilities like vortices. Note that the arrows do not indicate a velocity vector but pathways of fluid particles. The velocity profile of laminar flow will be discussed in section 2.1.3

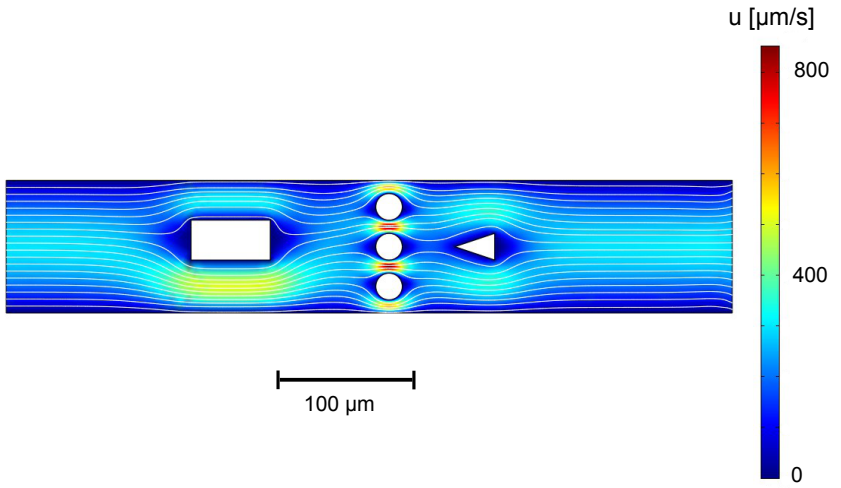

Figure 2.2: Streamlines in a laminar flow. This finite elements model shows the behaviour of a laminar flow in a microfluidic channel. Although obstacles partially block the flow, the streamlines do not cross but remain parallel.

2.1.3 Pressure-Driven Flow Profile

Under laminar flow conditions, incompressible Newtonian liquids can be described by the following simplified version of the Navier-Stokes equation:

$$\rho \frac{\partial \vec{u}}{\partial t} = -\vec{\nabla} P + \rho \vec{g} + \eta \nabla^2 \vec{u} \tag{2.2}$$

with ρ as the density, η as the viscosity and $\vec{u}$ as the velocity of the liquid. P and $\vec{g}$ denote the pressure and the gravitational acceleration, respectively. In simple terms, the equation can be understood as a force balance ($\rho \frac{\partial \vec{u}}{\partial t} = \frac{\text{force}}{\text{unit volume}}$) between the pressure gradient $-\vec{\nabla} P$, the gravitational force $\rho \vec{g}$ and the shear forces $\eta \vec{\nabla}^2 \vec{u}$.

In the case of a laminar flow between parallel plates (see Figure 2.3), the y and z components of $\vec{u}$ can be neglected, as the only relevant flow will be in x direction. Thus, $u_y = u_z = 0$. Only $u_x(y)$ is of interest. Therefore,

$\vec{\nabla}^2\vec{u}$ becomes $\frac{\partial^2 u_x}{\partial y^2}$. It can further be assumed that without any geometry changes, the pressure only varies in x-direction. If the length L of the system is large enough to assume equilibrium, the flow velocity does not change with time or in x-direction. Thus, $\frac{\partial \vec{u}}{\partial t} = \frac{\partial \vec{u}}{\partial x} = 0$. When gravitational forces are neglected, equation 2.2 becomes:

$$\frac{\partial P}{\partial x} = \eta \frac{\partial^2 u_x}{\partial y^2}. \tag{2.3}$$

This equation can be integrated and solved for $v_x(y)$. If the distance between the plates is d and $y = -\frac{d}{2}$ and $y = \frac{d}{2}$ are the locations of the plates, the no-slip boundary condition that the flow near the plates is zero becomes $v_x(\frac{d}{2}) = v_x(-\frac{d}{2}) = 0$. As the pressure gradient can be expressed

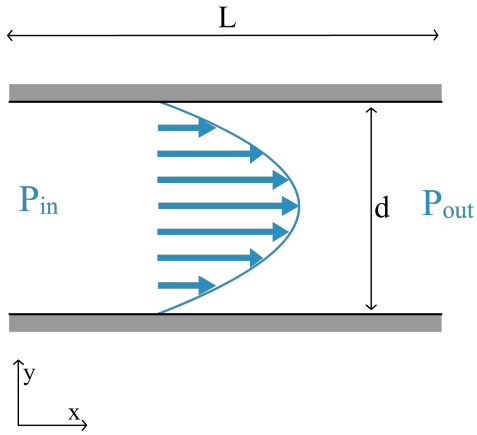

Figure 2.3: Parabolic flow profile. Laminar flows between two parallel planes assume a parabolic flow profile where the maximum velocity v_{max} is in the center between the plates. Friction at the walls usually leads to a vanishing velocity in the layers adjacent to the wall.

as $\frac{\partial P}{\partial x} = \frac{P_{in}-P_{out}}{L} = \frac{\Delta P}{L}$, the result becomes[1] :

$$v_x(y) = \frac{\Delta P}{2\eta L}\left(\frac{d^2}{4} - y^2\right). \tag{2.4}$$

As can be seen from equation 2.4, the flow velocity is a parabolic function with the maximum flow velocity v_{max} at the center between the plates. Figure 2.3 shows the schematics of such a flow profile.

If the geometry is a pipe or circular channel instead of the space between two plates, the flow becomes cylindrical with the v_{max} in the channel center and $v = 0$ at the channel walls. The solution to equation 2.3 then becomes:

$$v_x(r) = \frac{\Delta P R^2}{4\eta L}\left(1 - (\frac{r}{R})^2\right) \tag{2.5}$$

with R as the pipe radius.

Microfluidic channels are generally not circular but - in first approximation - rectangular. Thus, the symmetry of the flow profile is broken and equation 2.5 is not valid anymore. Nevertheless, the general phenomenon of v_{max} in the center of the channel and $v = 0$ at the walls is consistent.

2.1.4 Mixing on the micro scale

Due to the ubiquity of laminar flow conditions in microfluidic systems, mixing between parallel streams can only be accomplished through diffusion. However, for many biomedical analytes such as large proteins or DNA, the diffusion times are on the order of 1000 s, far longer than the residence times within the microfluidic channel system [54,57]. Should analysis or synthesis steps require the addition of reagents inside of the channel system, methods for improved mixing need to be integrated.

Basically, two types of micromixers designed for microfluidic applications can be distinguished [54,57].

1 A more detailed discussion can be found in the work of Bruus *et al.* [50].

The first type enhances the diffusion efficiency by diminishing the diffusion length [54,56,58]. Flow focussing with narrowing channel dimensions is one example for this mixing scheme [59]. Since diffusion length x and time t are connected by the relationship

$$\overline{x}^2 = 2Dt \tag{2.6}$$

with D as the diffusion coefficient, a decrease in the channel width significantly decreases the time required for diffusive mixing. Other micromixers utilizing a reduction in diffusion length are parallel lamination mixers using bifurcation-type feeds [60] or parallel interdigital-type feeds [61]. Details about these and further examples can be found in the literature [54,56,58].

The second group of microfluidic mixing devices utilizes streching and folding to segregate the liquid into small domains, thus increasing the contact area and decreasing the mixing path [54,56,57,58,62]. This requires chaotic trajectories [62] that can only be achieved through a three-dimensional flow (e.g. herringbone mixers [63]) or through a dependence of the flow velocity on time. Note, however, that although the flow trajectories become chaotic, the flow itself remains laminar, as the Reynolds number is not significantly increased by these devices [54].

Micromixers can further be differentiated into active and passive mixing devices [54,56,58,64,65]. Active mixers utilize external energy input to enhance mixing. Usually, these systems work with a time-dependant perturbation of the flow, e.g. ultrasonic vibration [66] or the induction of Lorentz forces in electrolyte solutions [67]. Although active micromixers have superior mixing efficiencies [68], their design requires complex structuring and integration, rendering the fabrication complex and expensive. In passive devices like the herringbone mixer [63], the channel is designed in such a way that the flow is restructured and therefore mixing efficiency is increased through either chaotic trajectories or flow focussing. Thus, passive devices do not require external power supply and are significantly easier to fabricate.

2.2 Magnetism

If a magnetic dipole is subjected to an external field, the potential energy E_{pot} of this dipole can be written as

$$E_{pot} = -\vec{m} \cdot \vec{B} \tag{2.7}$$

with $\vec{m}$ as the magnetic moment of the dipole and $\vec{B}$ as the magnetic flux density. The force $\vec{F}_{mag}$ acting on this dipole can be written as the derivative of the magnetic energy [69]

$$\vec{F}_{mag} = \vec{\nabla}(\vec{m} \cdot \vec{B}). \tag{2.8}$$

If the magnetic moment of the particle is not varying in space it can be assumed that $\vec{\nabla}\vec{m} = 0$ [45] and Equation 2.8 simplifies to

$$\vec{F}_{mag} = (\vec{m} \cdot \vec{\nabla})\vec{B}. \tag{2.9}$$

Note that this assumption is only valid if the moment is permanent or the magnetic moment of the particle is saturated by a strong magnetic field. For superparamagnetic nanoparticles in a non-magnetic medium, the magnetic moment can be expressed as

$$\vec{m} = V\vec{M} = V\chi\vec{H} = \frac{1}{\mu_0}V\chi\vec{B} \tag{2.10}$$

with $\vec{M}$ as the magnetization of the particle, $\vec{H}$ as the magnetic field strength and μ_0 as the vacuum permeability [45]. χ represents the magnetic susceptibility and gives the extent to which materials can be magnetized by external fields. It is defined as the derivate of the magnetization $\vec{M}$ with the field strength $\vec{H}$ of the external field[1]:

$$\chi = \frac{\partial\vec{M}}{\partial\vec{H}}. \tag{2.11}$$

1 Note that to obtain equation 2.10, the dipole is assumed to be point-like.

In most cases, for low field strengths, χ is a constant, resulting in a linear dependency of $\vec{M}$ on $\vec{H}$. However, when $\vec{H}$ increases, χ decreases as the material reaches it saturation magnetization, M_s (see Figure 2.5).

Combining Equation 2.9 and 2.10 leads to

$$\vec{F}_{mag} = \frac{V\chi}{\mu_0}(\vec{B} \cdot \nabla)\vec{B}. \tag{2.12}$$

This equation shows that in order to obtain high magnetic actuation forces, both the magnitude of the magnetic field and the magnetic field gradient need to be high. The magnetic field induces a large moment in the particle which is then influenced by the field gradient [16,45].

2.2.1 Magnetism on the nano scale

When the size of a ferromagnetic material is decreased below a critical threshold, the thermal energy starts to exceed the magnetic crystalline anisotropy energy of the particle [35,45,70,71?]. The particle then exhibits a random, fluctuating magnetization. An ensemble of these particles will therefore show an average net magnetization of zero, as the fluctuating magnetic moments of the particles average out over time and space. This magnetic state is referred to as *superparamagnetism* to denote its resemblance to the behavior of paramagnetic materials. Only under the influence of an external magnetic field, the magnetic moments of the individual particles align and the ensemble gains a net magnetic moment different from zero. Like a paramagnetic material, ideal superparamagnetic particles possess zero remanence, although in reality a small hysteresis is oftentimes visible. The critical limit for the particle size, the *superparamagnetic limit*, depends on the magnetic material, but is usually in the range of a few dozen nanometers. It can roughly be estimated as the radius r where

$$K \cdot \frac{4}{3}\pi r^3 < 10 \cdot k_B T \tag{2.13}$$

with K as the magnetic anisotropy constant of the material, k_B as the boltzmann constant and T as the temperature [45]. Table 2.2 shows some critical particle sizes for standard nanoparticle materials.

Table 2.2: Superparamagnetic limits of ferromagnetic particles of various materials. The limit is given as the diameter below which a particle becomes superparamagnetic. The data was taken from [72].

Material	Diameter/nm
hcp-Co	7.8
fcc-Co	15.8
bcc-Fe	16.0
Fe_2O_3	34.9
Fe_3O_4	28

2.2.2 Beads

Superparamagnetic particles allow to switch the magnetic properties on or off by changing the magnetic field within the surrounding medium. In the presence of an external field, the particles behave like (weaker) ferromagnetic matter. In the absence of a field, the particles behave like non-magnetic materials. This can be used to create switchable magnetic materials for microfluidic applications. For this, superparamagnetic nanoparticles are encapsulated in a polymer shell (typically on a size scale around 1 µm), usually created by emulsion or dispersion polymerization of polystyrene or silica [35]. Figure 2.4 shows the general structure of these microparticles, often referred to as *beads*. These beads then exhibit superparamagnetic behavior themselves (see Figure 2.5) and find application in various biomedical analysis methods [13,16,35,38,45]. Their surface can be coated with chemical functionalities like carbon acids or biomolecules such as antibodies or DNA. This way, they can interact with or bind to a wide variety of analyte molecules, either reversible or irreversible. Thus, they can serve as mobile substrates for bioanalysis, offering a far superior surface-to-volume ratio than any other surface in a micro channel.

Beads can be synthesized from various materials. The common choices, however, are polystyrene or silica as the encapsulating material. Beads made from polystyrene generally possess a very narrow size distribution

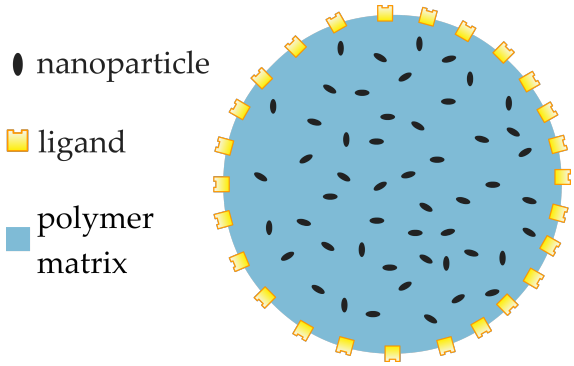

Figure 2.4: Structure of a magnetic bead. Superparamagnetic nanoparticles are encapsulated in a polymer matrix (e.g. polystyrene). The surface of the bead is functionalized with ligands such as streptavidin, biotin, DNA strands or antibodies. Through these ligands, biomolecules can be attached to the bead surface.

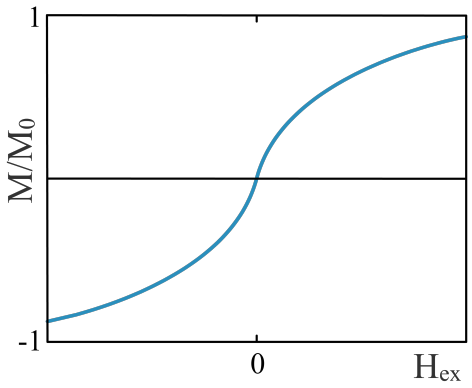

Figure 2.5: Hysteresis of an ideal superparamagnetic bead. In the absence of an external field H_{ex}, the bead does not show a magnetization. At high field strengths, the magnetization M approaches the saturation magnetization M_0.

and a nearly ideal spherical shape. Table 2.3 gives some detailed data about the beads (Dynabeads) that were used in the experiments of this thesis[73]. However, as their surface is hydrophobic, polystyrene beads tend to unspecifically bind proteins, antibodies, etc. This can significantly decrease their performance in bioanalysis. Thus, care has to be taken when designing the surface modifications so that the bead surface is not exposed to the analyte solution. Silica beads on the other hand, although equipped with a superior, hydrophilic surface, are hardly available in small size distributions and an ideal spherical shape.

When choosing the appropriate beads for specific experiments, further attention has to be paid to the interactions between beads. Different surface functions lead to changes in the bead-bead interactions, which are mainly due to van der Waals forces and electrostatic interaction. If the attractive forces outbalance the repulsive forces and the thermal movement of the particles, undesired agglomerates start to form and the device performance is decreased. As van der Waals forces are always attractive, electrostatic forces have to be used to keep beads from agglomerating. For this purpose, a surface modified with carbon acids with its negative charge in neutral or alcalinic media has proven to be useful.

Although beads are more dense than the surrounding liquid and will eventually settle on the bottom of a microfluidic device, the gravitational

Table 2.3: Physical properties of different superparamagnetic bead species (Dynabeads, life technologies). SD gives the standard deviation of the particle diameter. χ is the initial magnetic susceptibility at low field strength. M_0 is the mass saturation magnetization of the beads. The data was taken from Fonnum *et al.*[73].

Bead	Diameter $/\mu m$	SD /%	Density $/g \cdot cm^3$	$\chi \cdot 10^{-5}$ $/m^3 \cdot kg^{-1}$	M_0 $/Am^2 \cdot kg^{-1}$
M-280	2.83	1.4	1.4	54	10.8
M-450	4.40	1.2	1.6	102	19.6
MyOne	1.05	1.9	1.9	81	23.5

force is mainly cancelled by buoyancy. As gravitation and other volume effects loose their importance in microsystems (see section 2.1.1), the beads stay dispersed for several minutes, depending on their size and density. This time is usually longer than any residence time within the microfluidic structures.

If contact between beads and surfaces occurs, unspecific interactions, e.g. van der Waals forces, may lead to adhesion. To counteract this, surfactants like Tween20 can be used to prevent direct contact between the channel surface and the bead material.

Beads in μ-TAS

Outside of microfluidics, beads are widely used for MRI contrast enhancement, hyperthermia curing of cancer, drug targeting and magnetic separation[45]. In the fields of microfluidics, however, beads are mainly used as solid support or as magnetic labels for cells, antigenes, antibodies or DNA[35,45].

As previously mentioned, beads can be functionalized with various chemical and biochemical groups that enable specific or non-specific, irreversible or reversible binding between beads and analyte molecules. The beads can thus be used as mobile substrates with increased surface-to-volume ratio. As they can be agglomerated under the influence of a magnetic field, they can be easily recovered or exchanged from solution.

Under the influence of homogeneous magnetic fields, magnetic beads experience a force towards higher magnetic field densities (see Equation 2.12). This enables magnetic separation in inhomogeneous magnetic fields (*magnetophoresis*). While the dielectric response of most materials is strong enough to allow for dielectrophoretic effects, magnetophoresis only applies to magnetic materials, i.e. the beads. This allows for the selective transport[74,75,76,15] or separation[77,78,79,80,19,20] of bead-bound analytes. Additionally, since the controlling magnets can be external, no contact with the fluid is required.

Furthermore, with the help of GMR[23,24,25,26,27,28], TMR[22,21] or Hall sensors[32], the magnetic stray field of beads can be detected, making them an interesting alternative to “classic” labelling techniques in biomedical

research, such as fluorescent molecules, radioactive isotopes, catalytic enzymes or charged molecules. Their advantages are numerous: They are stable over time, not affected by the reagent chemistry or the sample matrix and the signal does not depend on parameters such as pH, ionic strength etc. Furthermore, there is usually no background signal from the sample, the signal is not screened by aqueous media and the detection devices are very sensitive and easy to integrate, different from optical setups that usually require complicated external systems. Thanks to recent technological advances, magneto-resistive sensors do not require complex structuring anymore, but can be printed onto a surface, either by the use of GMR-ink made from tiny flakes of GMR sheets [33] or in the form of GMR-gels utilizing the granular GMR effect of nanoparticles [81].

With the use of magnetic beads, nearly all relevant functions in a bioassay, namely sample purification, localization on a substrate, labeling, manipulation, transport, separation and detection, can be realized.

Suprastructure formation

In µTAS, superparamagnetic beads are usually used as solid support or magnetic labels for transport, separation and detection. For these applications, agglomeration of the beads is not desired (unless a complete separation of beads from the solution is required) as it would interfere with the device performance. Therefore, concentrations are usually kept in the low concentration regime, where interactions between beads are minimized due to large interbead distances. However, there has recently been an increasing interest in the behaviour of dispersions of superparamagnetic beads in the high concentration regime. Under these conditions, beads tend to form *supraparticle structures* (SPS) under the influence of magnetic fields (see Figure 2.6) [45]. In the absence of a magnetic field, the superparamagnetic beads possess a net magnetization of approximately 0. Thus, there is no magnetic interaction. The application of a magnetic field $\vec{B}$, however, creates a torque τ acting on the magnetic moment vectors $\vec{m}$ of the nanoparticles within the bead:

$$\tau = \vec{m} \times \vec{B}. \tag{2.14}$$

This torque leads to an alignment of the magnetic moment vectors, which in turn leads to the development of a stray field. If the magnetic field is homogeneous, it does not exercise a force on the magnetic beads (compare equation 2.9). However, if the interbead distance is small enough, the inhomogeneous stray fields of the beads will lead to attractive forces. In 1999, Furst and Gast [82] measured the magnetic attraction forces between adjacent beads in a linear arrangement with dual-trap optical tweezers. They measured forces on the order of 5-50 pN, depending on the external field strength.

The attractive forces caused by the stray fields result in an alignment of particles along the lines of the magnetic field. These one-dimensional agglomerates, further referred to as *chains* (see Figure 2.7), start to rotate if the magnetic field is rotated in-plane. With increasing rotation frequency, there is an increasing lag between the angular movement of the chain and the magnetic field [42]. Due to this lag, the magnetic moment vectors of the beads (which follow the magnetic field vector almost instantly) are not aligned with the chain axis anymore. The lateral magnetic force that leads to attraction between the beads in the chain is thus reduced. This results in a structural instability beyond a certain rotation frequency (or Mason number, see following section). The chains collapse, forming two-dimensional, disc-like structures (*clusters*). The magnetic configuration within these structures is not known in detail, but calculations performed by Weddemann *et al.* indicate the formation of magnetic domains of antiparallel orientation that span a few dozen beads [43].

Mason number

The behaviour of SPS chains under the influence of a rotating magnetic field depends on the *Mason number* (Mn) of the system [41,42,83]. This dimensionless number describes the ratio of viscous to magnetic forces. In this work, the definition of Petousis *et al.* [42] will be used, which is given as

$$Mn = \frac{16\eta\omega}{\mu_0\chi^2 H^2} \tag{2.15}$$

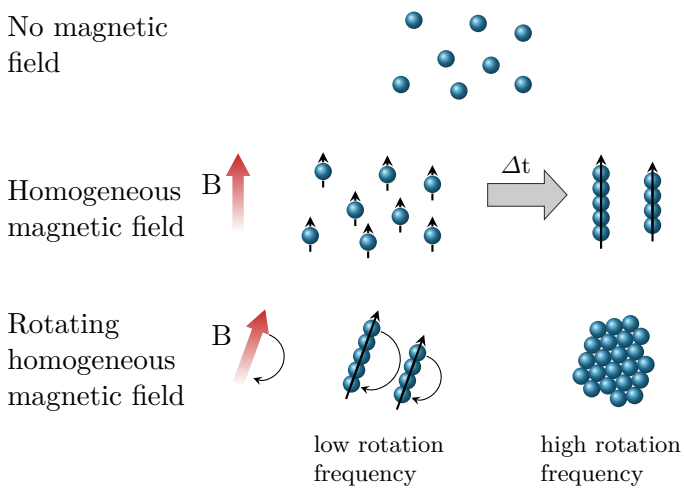

Figure 2.6: Formation of suprastructures (SPS) of superparamagnetic beads. In the absence of an external magnetic field, the beads show no net magnetization. Under the influence of an external, homogeneous magnetic field, the magnetic moment vectors of the particles are aligned. The resulting inhomogeneous stray field of each bead leads to attractive forces between adjacent beads, resulting in the formation of 1D agglomerates (*chains*) if the bead concentration is sufficiently high. If the external field is rotated at low frequencies, the chains rotate with the field. An increase of the rotation frequency will finally result in the collapes of the chains into 2D *cluster* structures.

with η as the viscosity of the liquid, ω as the angular velocity of the field, μ_0 as the vacuum permeability, χ as the magnetic susceptibility and H as the magnetic field strength.

The average length of SPS structures in rotating magnetic fields decreases with Mn, as viscous force dominate the magnetic forces. Both Petousis *et al.*[42] and Melle *et al.*[41] found a proportionality between the chain length L and the Mason number:

$$L \propto Mn^{-1/2}. \tag{2.16}$$

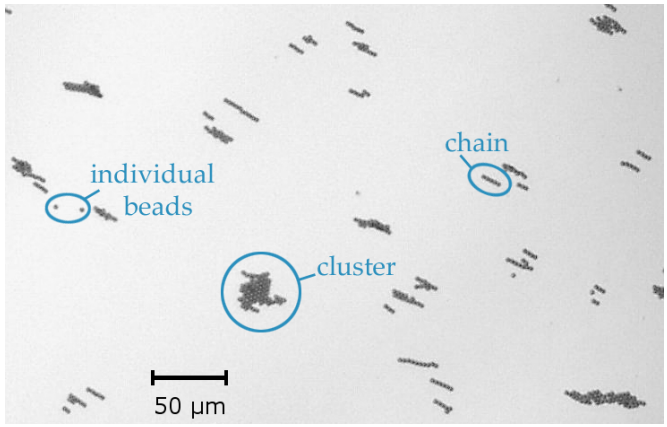

Figure 2.7: Microscopy image of beads under the influence of a rotating magnetic field. Apart from individual beads, one-dimensional *chains* and two-dimensional *clusters* can be observed.

If the Mason number exceeds a certain limit, the viscous forces dominate the magnetic forces. Then, the chain starts to deform slightly from the straight chain shape and assumes an S-like configuration (see Figure 2.8). If the Mason number is further increased (e.g. by an increase of the rotation frequency), the chain breaks up into shorter chain segments or folds into a two dimensional cluster.

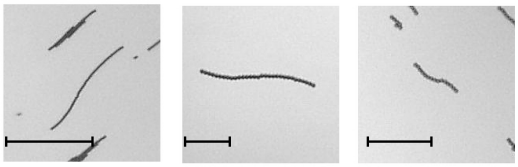

Figure 2.8: Chain deformation in rotating magnetic fields due to viscous forces. Before a break-up occurs, chains take on an S-shape if the Mason number becomes too high. The deviation from the direction of the magnetic field destabilizes the chain further, finally resulting in fragmentation. The scale bars indicate a length of 50 µm.

2.3 Optical Detection

In this work, both absorption spectroscopy and surface enhanced Raman scattering (SERS) were applied to analyse samples. In the following sections, the theoretical background of these methods will be introduced shortly. As Raman spectroscopy was a significantly more important part of this work than absorption spectroscopy, the former is introduced in more detail than the latter.

2.3.1 Absorption Spectroscopy

Absorption spectroscopy is a method that utilizes the frequency-dependent absorption of light by atoms and molecules. As the absorption at a specific frequency depends strongly on the energy levels within the molecule or atom, this gives rise to an analyte-specific absorption spectrum if the absorption is measured over a broad range of frequencies.

For a given molecule, light can only be absorbed if the energy of the photons corresponds to the energy difference between electronic, vibrational

or rotational states of the molecule[1]. The intensity of the absorption (*absorbance*) can be calculated by the Lambert-Beer-Law:

$$A = -lg(\frac{I}{I_0}) = \varepsilon cd \tag{2.17}$$

with A as the absorbance, I and I_0 as the intensity of the transmitted and the incident light, ε as the extinction coefficient, c as the concentration and d as the path length of the light within the absorbing sample. Thus, if the extinction coefficient and the pathlength are known, measuring the absorption of a sample yields the concentration of the absorbing molecule. For more details on this method, the reader is referred to other literature [84,85,86].

2.3.2 Raman Scattering

Raman spectroscopy is a form of vibrational spectroscopy[2] that was first observed by Sir C. V. Raman in 1928 [89]. It is based on the inelastic (or 'Raman') scattering of monochromatic light, usually supplied by a laser light source (see Figure 2.9). The basic mechanism behind Raman spectroscopy can be explained in a photon or a wave picture [90]:

Photon picture: The incoming photons collide with molecular bonds from the sample and can undergo elastic or inelastic scattering. Elastically scattered photons (*Rayleigh scattering*) retain their initial frequency. If a spectrum of the scattered light is collected, these photons give rise to the very intense *Rayleigh peak* (see Figure 2.10). However, there is a small chance for photons to collide inelastically, resulting in a certain, characteristic frequency shift. The energy difference between the incoming photons and the scattered photons corresponds to difference between the

1 To be more exact, selection rules such as the Laporte rule forbid certain transitions so that they don't show up in the absorption spectrum. For more information about selection rules, please refer to other work [84,85,86].

2 To be exact, it is also a rotational spectroscopy method, as each Raman signal is divided into several sub-peaks corresponding to differences in rotational energy levels of the probed molecule. However, this is of no further importance for this work and will therefore not be explained in detail. For further information, see the work published by other authors [87,88,85].

energy levels of vibration. In most cases, the frequency is shifted to a lower frequency. In this case, the probed molecule is excited from a lower to a higher vibrational state. The corresponding peak in the spectrum is called *Stokes-shifted Raman peak*. However, if a molecule in an excited vibrational state is probed, there is a finite chance for it to transfer energy to the photon and return to a lower vibrational state. The corresponding peak is called *anti-Stokes shifted Raman peak* and is shifted to higher frequencies. Although the Raman effect is often described as an excitation to a virtual energy state from which the molecule returns to an excited vibrational state, it is *not* an actual absorption and emission process but pure scattering.

Wave picture: The incident electromagnetic wave of the light induces a dipole moment in the molecule. Since the polarizability α that significantly influences the dipole induction is a function of the atomic arrangement inside the molecule, it is influenced by vibrations. The generation of the dipole moment is therefore modulated by molecular vibrations. Thus, the dipole oscillates not only at the frequency of the incoming field, but also at side bands that depend on the frequencies of the molecular vibrations. This leads to the appearance of Stokes and anti-Stokes peaks in the scattered light.

In contrast to infrared absorption, which also gives information about vibrational states, the frequency of the incident light in Raman spectroscopy does not have to correspond to the energy difference between vibrational levels, as Raman is not an absorption process. Usually, wavelengths in the visible or near-infrared range are used for Raman spectroscopy.

Raman spectroscopy supplies high structural information about the probed molecules. As the vibrational energy levels depend on the mass of atoms, the bond strengths and the spatial arrangement of the atoms of a molecule, the resulting spectrum is specific for each molecule - often termed a "molecular fingerprint". Since water is a very weak Raman scatterer, Raman spectroscopy can be used to look at molecular vibrations of molecules in aqueous media, e.g. biomolecules such as proteins. With infrared absorption this would not be feasible, as water has a broad absorption band in the near-infrared.

However, despite its advantages, Raman spectroscopy suffers from extremely weak signals, as Raman scattering is a rare process compared

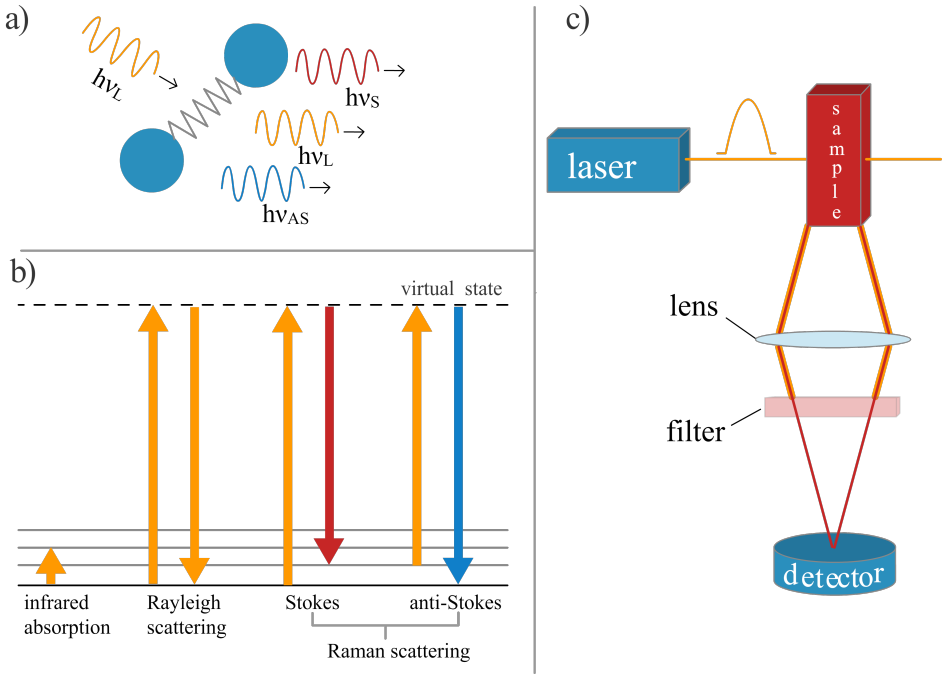

Figure 2.9: (a) Schematics of Raman scattering. Incoming light is scattered by a Raman scatterer. The scattered light can have the energy of the incoming light ($h\nu_L$) or it can be shifted to higher ($h\nu_{AS}$) or lower ($h\nu_S$) energies. (b) Energy diagram of the Raman effect. In normal IR absorption spectroscopy, molecules are excited from the ground state into a higher vibrational state. The energy of the light equals the energy difference between the states. In Raman spectroscopy, light of higher energy is used. Elastic scattering of the light can be understood as the excitation into a virtual high-energy state with an immediate disexcitation to the initial state (*Rayleigh scattering*). Note, however, that this is not a real absorption-emission process. In *Raman scattering*, the disexcitation leaves the molecule in a higher or lower vibrational state than the initial state. The scattered light is therefore shifted to lower (*Stokes*) or higher (*anti-Stokes*) energies. (c) Schematics of a Raman spectroscopy setup. A sample is placed in the path of a laser beam. The scattered light is focused onto a detector. A filter removes the light with the wavelength of the incident beam (Rayleigh scattering).

to Rayleigh scattering. The intensity of the Stokes-shifted Raman signal $P^{RS}(\nu_s)$ can be described by the formula [90]

$$P^{RS}(\nu_s) = N\sigma^R_{free} I(\nu_L) \tag{2.18}$$

with N as the number of probed molecules, σ^R_{free} as the Raman cross section and $I(\nu_L)$ as the intensity of the incident laser light. Cross sections in Raman spectroscopy are typically 12-14 orders of magnitude smaller than for fluorescence spectroscopy, making it necessary to find ways to enhance the Raman signal.

2.3.3 Surface Enhanced Raman Scattering

In the 1970s, Fleischmann *et al.* [93] and Jeanmaire *et al.* [94] found unexpectedly high Raman signals from molecules adsorbed on a rough silver electrode. This discovery led to the development of the *surface enhanced Raman scattering* (SERS) technique. If a molecule is adsorbed on or close to a suitable metal surface, the Raman signal of this molecule is significantly

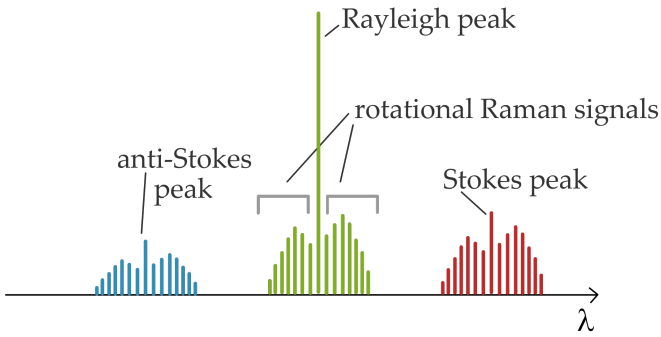

Figure 2.10: Schematic spectrum of a Raman scatterer in the gas phase. In the center at the wavelength λ_0 of the incident laser light, the Rayleigh peak appears in the spectrum. The Stokes peak is shifted towards longer wavelengths, while the anti-Stokes peak is shifted towards the shorter wavelengths compared to λ_0. In all peaks, rotational subsignals can be seen if the resolution is sufficiently high.

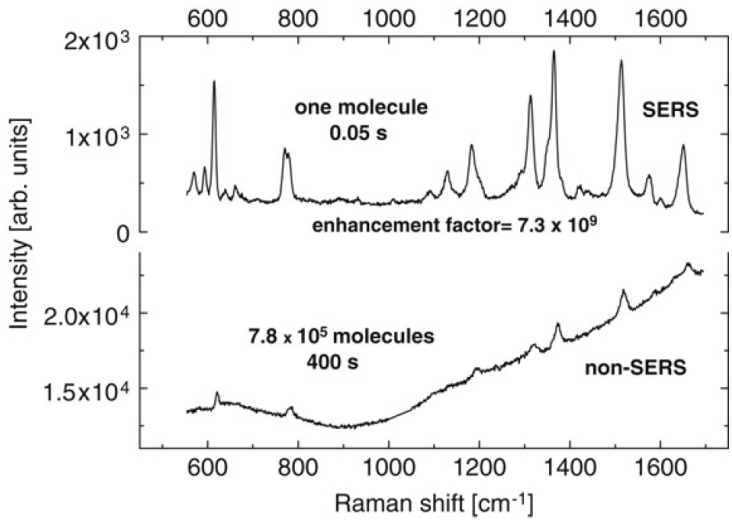

Figure 2.11: Raman (non-SERS) and SERS spectra of rhodamine 6G molecules (laser excitation with 3 mW at 633 nm). Even though only one molecule was sampled and the integration time was 8000 times shorter, the SERS spectrum is far superior to the Raman spectrum. More experimental details are reported in the work of Le Ru *et al.*[91,92] from which these spectra were taken.

enhanced, often by several orders of magnitude. Optimal circumstances can lead to enhancement factors of up to 10^{12}, making SERS a potential single molecule technique[95,96,97,98]. These trace analytical capabilities offer interesting opportunities for lab-on-a-chip systems. SERS combines the advantages of Raman spectroscopy (clear fingerprint spectra, application under biologically ambient conditions, absence of problems such as photobleaching or self-quenching) with cross-sections in the range of fluorescence spectroscopy. Figure 2.11 shows a comparison between a Raman spectrum obtained from an ensemble of molecules and a single molecule SERS spectrum.

The significant enhancement of the Raman scattering process is usually explained through two mechanisms, an *electromagnetic field enhancement*

and a *chemical* or *electronical enhancement*. However, the chemical/electronical enhancement effect is not fully understood in detail and there is yet some discussion about whether this is really a separate mechanism [99]. Due to the fact that different Raman modes may be enhanced by different mechanisms, SERS spectra can show deviations from normal Raman spectra - not only concerning the intensities of the peaks but also their positions, as interactions between molecules and metal surface can shift the peaks and change the line widths [90].

Electromagnetic Field Enhancement

If a molecule is exposed to an incident light beam while it is in the vicinity of a metallic structure, it experiences an electromagnetic field that is different from the one experienced by a free molecule in vacuum. The actual field E_M is a superposition of the incoming field E_0 which corresponds to the incident light and the field of a dipole induced in the metal, E_D. The dipole field is due to resonant excitations of surface plasmons in the metal structure. This increased field strength in the vicinity of the metal leads to a stronger interaction between the molecule and the light, resulting in a higher chance for Raman scattering. In an analogous way, the electromagnetic fields of the scattered Stokes or anti-Stokes light will be enhanced if they are in resonance with the surface plasmons. Therefore, if both the incoming and the scattered light are in resonance with surface plasmons, a very high Raman signal enhancement of $10^6 - 10^7$ is achieved. As this enhancement is caused by the electric field around the metal surface, no direct contact is required. However, the effect degrades with the distance d as $(1/d)^{12}$, so that the molecules will have to be close to the surface. Furthermore, the scattering requires the plasmon to possess a component that is perpendicular to the surface. This requires a rough surface, so that SERS substrates need to be fine structured, e.g. by laser lithography.

If clusters of colloidal nanoparticles are used as the metal surface instead, the dipole oscillators of the isolated particles couple and form a plasmon excitation that embraces the whole cluster. The range of the possible plasmon excitations then covers a broad range of frequencies, usually from the visible to the near infrared. However, the electric field is not

evenly distributed in such clusters. Instead, hot spots of the size of a few nanometers can be found where the field enhancement is significantly increased (up to enhancement factors of 10^{11}). Often, junctions between SERS active nanoparticles form such hot spot volumes.

Chemical/Electronic Enhancement

For the electronic enhancement effect, the molecule needs to be in direct contact with the metal surface and form an adsorbate-surface complex. The exact nature of the resulting enhancement is not fully understood, but it is presumed that there is a resonance Raman like effect that is responsible for the enhancement [90]. In resonance Raman spectroscopy, the energy of the incident laser light corresponds to electronic transitions within the molecule. Thus, rather than exciting into a virtual energy state, the molecule is excited into an actual electronic state. This results in an increase in the scattering intensity of modes associated with this electronic transition. In the adsorbed molecule, electronic levels are shifted and broadened by the interaction with the metal surface. New charge-transfer electronic transitions are possible as well. This results in a higher chance for resonance Raman events, thus increasing the Raman scattering by a factor of 10-100.

Substrates for SERS

The increased intensity of the SERS signal can be written as a modification of equation 2.18 [90]

$$P^{SERS}(\nu_S) = N^{SERS}\sigma^R_{ads}|A(\nu_L)|^2|A(\nu_S)|^2 I(\nu_L) \tag{2.19}$$

with N^{SERS} as the number of molecules involved in the SERS process, σ^R_{ads} as the cross-section of the adsorbed molecules, $A(\nu_L)$ and $A(\nu_S)$ as the enhancement factors for the incident and the scattered light and $I(\nu_L)$ as the intensity of the laser light. With careful fine-tuning of all parameters, enhancement factors of 10^{14} can be achieved. However, this requires a very well controlled morphology of the metal surface.

As previously mentioned, the enhancement is not distributed homogeneously over the whole metal surface. Instead, there exist hot spots in gaps

between surfaces and around sharp edges (*lightning rod effect*). Atomic-scale roughness is required to obtain such hot spot sites. A feasible way to obtain this is to use clusters of nanoparticles in the size scale of 10-100 nm, either in solution or dry on a surface. However, for common applications, reproducibility of the enhancement factors outweighs high enhancement factors. This can be achieved through well controlled nano-scale environments, as they are typically obtained by diverse milling procedures, or through averaging over a large number of active sites.

SERS has so far been achieved on metal surfaces made from silver [100,101], gold [102,103], copper [104,105], lithium, palladium, cadmium and nickel [106]. For the analysis of biochemical substances, however, gold is the preferred candidate, as high stability prevents degradation of the surface due to reactions with the biomatrix.

3 Materials and Methods

In this chapter, the general experimental methods and the materials that were used in the experiments will be presented. Setups, materials and parameters that were only applicable for certain experiments will be listed in the respective chapters.

3.1 Lithography

The microfluidic channels utilized in this work have been prepared by soft-lithography in polydimethylsiloxane (PDMS). The detailed process is also described in various articles[6,7,8,107,108]. The general fabrication steps are presented in Figure 3.1.

Soft-Lithography requires the design of a channel system in a CAD program. The design is then used to fabricate a mask in the form of a glass slide selectively covered with a UV radiation blocker, e.g. gold. This structured original is then used to selectively expose a photoresist layer to UV light, thus creating a master in positive relief photoresist. PDMS is then cast against the master to produce a replica containing the channel network. Finally, the channel system is sealed with a silicon wafer by plasma oxidation. In the following sections, these steps will be explained in more details.

Laser Lithography

After the initial design is written in a CAD program, the mask is written in a UV laser lithography system (DWL 66, Heidelberg Instruments).

For this, a thin glass slide of 2×2 cm^2 is cleaned by immersion in aceton and ethanol in an ultrasonic bath for 15 minutes, each. The glass slide

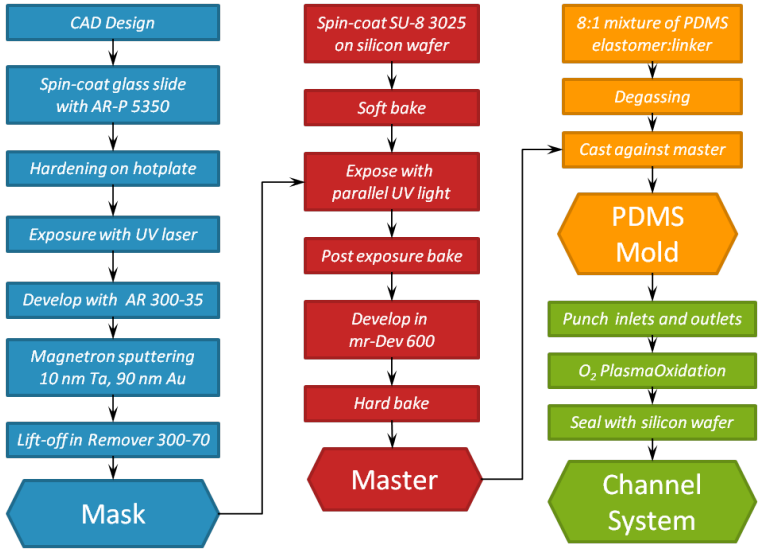

Figure 3.1: Soft lithography fabrication process. The figure shows an overview over the steps during different stages of soft lithography. First, a UV light blocking mask is fabricated. In a second step, this mask is turned into a polymer master. A mixture of PDMS elastomer and cross-linker is cast against the master to obtain a PDMS mold of the channel system. This mold is sealed with a silicion wafer after oxidation in an oxygen plasma.

is then spin-coated with a ~ 1 µm thick layer of the positive photoresist AR-P 5350, Allresist, under clean-room conditions.

Afterwards, the photoresist is hardend for 30 minutes on a hot plate (HAT-302D, AVT Technologie) at 85 °C.

The hardened photoresist is exposed in the laser lithography system, using a laser at a wavelength of 442 nm (Melles Griot). The laser output is set to 70 mW.

Subsequently, the exposed photoresist is developed with a 2:1 water-developer mixture of the developer AR 300-35 (Allresist) for 12 seconds.

The developed slide is sputtered with a 10 nm layer of tantal and a 90 nm layer of gold. Afterwards, the remaining photoresist with the metal layers on top is removed through immersion in a remover solution (Remover

300-70, Allresist) in an ultrasonic bath. During this lift-off step, only metal that directly contacts the glass surface remains (see Figure 3.2), yielding a mask for the mass-production of relief masters.

Master Fabrication

For the preparation of the master, the positive photoresist SU-8 3025 is used. This resist enables the production of stable structures with high aspect ratios. The photoresist is spin-coated onto a silicon wafer and subsequently exposed to UV light through the previously produced mask (see Figure 3.3).

A small silicon wafer (Si wafer with a 50 nm SiO_2 layer, Si-Mat) of approximately 2×2 cm^2 is cleaned by immersion in aceton and ethanol in an ultrasonic bath for 15 minutes, respectively. The cleaned wafer is then spin-coated with a layer of SU-8 3025 negative photoresist (Microchem). The layer thickness defines the final height of the micro channels. The coated wafer is then subjected to a soft bake procedure (5 minutes at 65 °C, 15 minutes at 95 °C, 120 minutes cooling-down) inside a programmable oven (Eurotherm HP-155, UniTemp).

The wafer is then exposed using a UV parallel exposure device with a mercury vapor lamp while relevant areas of the wafer are covered by the previously designed mask. The exposure time is 14 seconds, equivalent to an energy of about 500 mJ. Afterwards, the wafer is subjected to a post exposure bake (5 minutes at 65 °C, 15 minutes at 95 °C, slow cooling-down to room temperature) to enable the cross-linking within the photoresist.

In the last step, the wafer is developed for 6 minutes in mr-Dev 600 developer (Micro Resist Technology) and subjected to a hard bake (15 minutes at 160 °C, 120 minutes cooling-down) to harden the relief structure.

PDMS Channel System

In the next step, PDMS is cast against the fabricated master (see Figure 3.3). For this, a 8:1 mixture of PDMS elastomer and cross-linker (Sylgard 184 Kit, Dow Corning) is prepared. After 45 minutes, during which gas bubbles produced during the mixing step can escape from the mixture, the

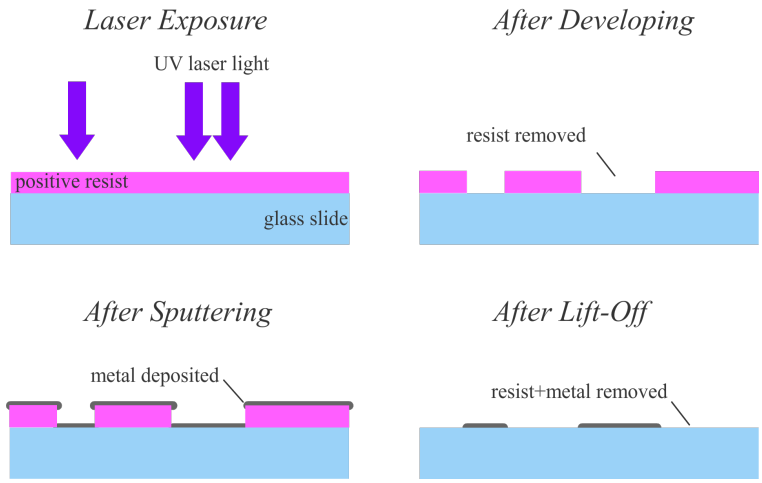

Figure 3.2: General steps of laser lithography for the production of an exposure mask. In the first step, a positive photoresist is exposed selectively with a UV laser. The exposed resist is removed and metal is sputtered on top of the remaining resist. In a lift-off process, the remaining resist is removed. Metal remains in the areas that were not covered by resist during the sputtering process, thus forming the exposure mask for the UV lithography.

PDMS is poured over the master. To support the PDMS curing, the sample is heated to 80 °C for 4 hours.

Afterwards, the PDMS can be peeled of the master. Inlet and outlet reservoirs are punched using a punch with a diameter of 1.4 mm. The resulting channel system is sealed with a silicon wafer by the means of plasma oxidation as described by Hellmich [109]. For these experiments, an oxygen plasma at 0.1 mbar was used. The duration was set to 30 seconds.

The plasma oxidation serves to both seal the PDMS to the silicon as well as change the surface characteristics of the PDMS channel walls. Untreated PDMS consists of repeating -$OSi(CH_3)_2$- units and is therefore hydrophobic. The plasma oxidizes the surface to hydrophilic silanol groups (Si-OH) [7]. However, molecular rearrangements within the PDMS return the surface to hydrophobic within half an hour unless the channel system is filled with water [7]. Thus, experiments should be performed immediately after the

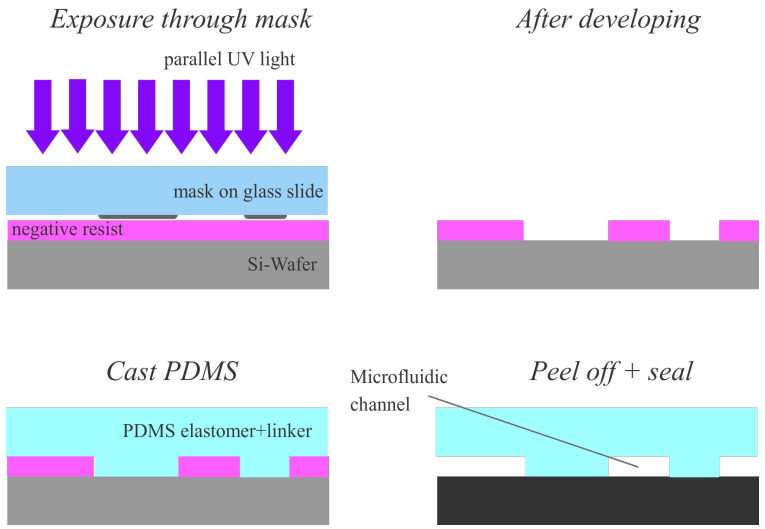

Figure 3.3: UV lithography and preparation of a PDMS mold. The previously fabricated mask is used to selectively expose a positive photoresist layer. After developing, the remaining photoresist can be used as a master against which a mixture of PDMS elastomer and cross-linker is cast. After peeling of the PDMS mold and sealing the open channels with another wafer, a sealed microfluidic channel system is obtained.

oxidation step.

3.2 Microfluidic Flow

The fluid flow in the experiments of this work was obtained through pressure differences caused by different fluid levels in the inlet and outlet reservoirs, only. A microfluidic pump (Nemesys, Cetoni) would have been available. However, in initial experiments the beads tended to settle inside the connection tubing. This prevented a steady supply of fresh bead dispersion and sometimes lead to clogging of the connection ports between tubing and microfluidic structure. Additionally, use of the pump required an additional lithography process to connect the microfluidic structure with the tubing. This process involved heating the structure, which resulted in a change in the surface properties of the PDMS channel system, which became hydrophobic. The hydrophobic surface increased the probability of beads sticking to the channel walls and thus hindered the experimental procedure. Therefore, use of the pump was avoided in all further experiments.

3.3 Optical Microscopy

The observation of the microfluidic experiments was performed using a reflecting microscope (VHX-600, Keyence, with a Z100-R lense). Videos were taken at 28 or 15 frames per second. The produced .avi files were transformed into a series of JPEG pictures using the Avidemux 2.4 software[110]. The individual pictures were then analysed with ImageJ[111] and the MTrackJ plugin[112].

3.4 Magnetic Field

The magnetic field for the experiments was supplied either through a IKA RCT basic magnetic stirring device (IKA), or by a Helmholtz coil setup that was developed by Peter Hedwig and Fabian Schmid-Michels.

Magnetic Stirrer

For experiments that required a strong magnetic field, the rotating permanent magnet inside a conventional magnetic stirrer as it is used in chemical

laboratories proved to be a very elegant way to supply a rotating, nearly homogeneous magnetic field. A photography of the total setup is shown in Figure 3.4 (a).

Two stirring devices, both of the type IKA RCT basic, were used for the experiments. The standard version produced a maximum magnetic field strength of approximately 330 Oe on the surface. A modified version where the permanent magnet was exchanged for a more efficient magnet produced a field of 690 Oe maximum. For both devices, the rotation frequency could be set to between 50 and 1500 rpm, in steps of 10 rpm. However, below 200 rpm, the motor was not rotating smoothly, resulting in occasional jumps from one angular position to the next.

Helmholtz coils

A smoother rotation was achieved in a setup of two pairs of Helmholtz coils, arranged in a 90° angle (see Figure 3.5). Each pair of coils was fed with a sinusoidal voltage signal. The signals were shifted by 90°, thus resulting in

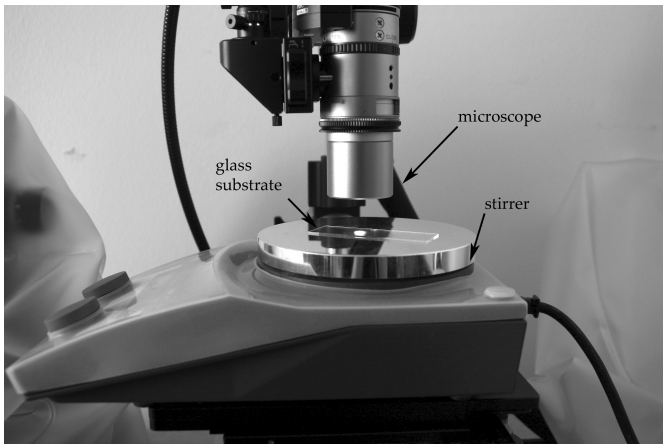

Figure 3.4: Setup for the magnetic stirring device. The IKA RCT basic was positioned underneath the Keyence VHX-600 reflecting microscope. Two different stirrers with maximum field strengths of 330 Oe or 690 Oe could be chosen.

a circular motion of the magnetic field direction in the center between the coils, where the sample was placed during experiments (see Figure 3.6). To prevent overheating the coils, they were cooled by a water cooling system. Each coil consisted of about 100 loops of copper wire with a diameter of 0.18 mm (Menting Mikroelektrik).

Since the maximum current flowing through the coils was limited due to Joule heating, the maximum field strength of around 120 Oe achievable with the coil setup was far inferior to the field strength provided by the magnetic stirrers. However, the smoother rotation and the ability to switch between field-on and field-off states made this setup the preferred choice for experiments where high field strengths were not required.

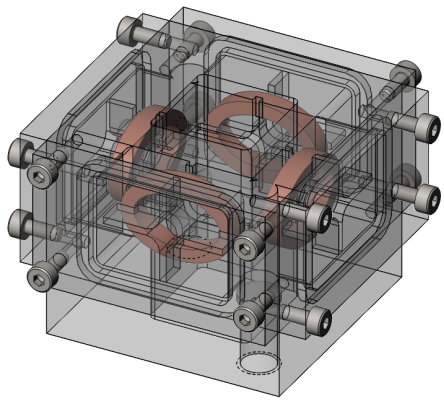

Figure 3.5: Design of the Helmholtz coil setup. Two pairs of coils are arranged at a 90° angle and incorporated into a water cooling system to counteract Joule heating.

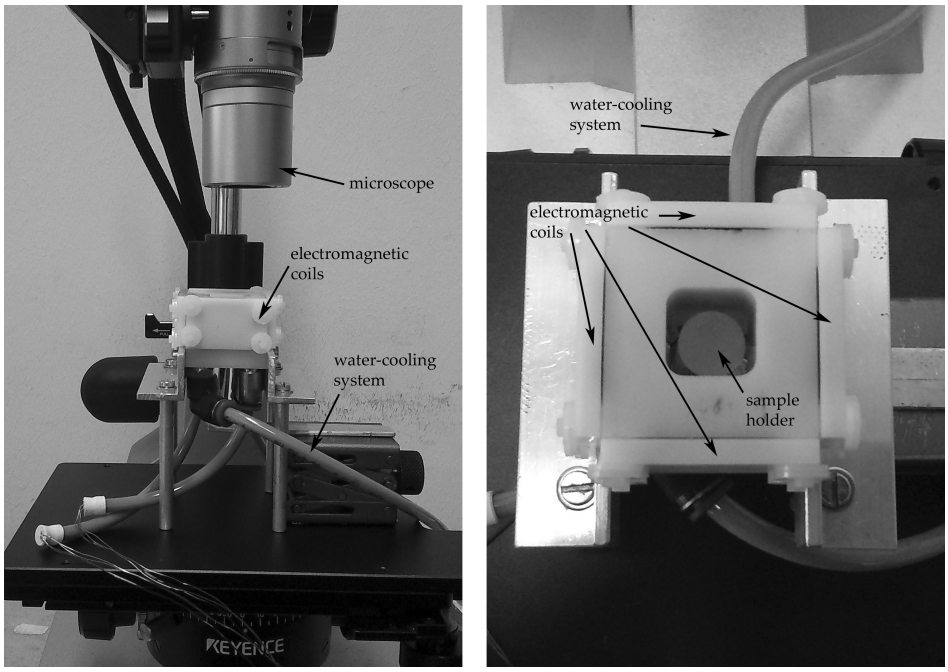

Figure 3.6: Setup for the magnetic stirring device. Left: Side view. Right: Top view. The electromagnetic coils (2 pairs of Helmholtz coils at 90° angle) were positioned underneath the Keyence VHX-600 reflecting microscope. The coils were cooled using a water cooling system. Maximum field strengths were on the order of 120 Oe.

3.5 Raman Spectroscopy

All Raman spectra presented in this work were collected by Elina Oberlander from the Biomolecular Photonics group of Bielefeld University. The setup used for these measurements is a home-made micro-Raman system (see Figure 3.7) with a laser diode (Innovative Photonic Solutions) emitting at a wavelength of 785 nm. The excitation wavelength is cleaned with optical band pass filters (Semrock). Light is then focused onto the sample with a 60x water-immersion microscope object lens (Olympus, 1.2 NA). The backscattered photons are collected by the same lens and directed to a dichroic beamsplitter. After passing the beamsplitter and a long pass razor-edge filter (Semrock) to block the Rayleigh-scattered photons, the light is coupled through a x10 air object lens (Olympus, 0.25 NA) into a multimode step-index fiber (Thorlabs, AFS105/125Y, 105 µm, 0.22 NA, 400-2400 nm) that leads to the monochromator (Acton 2300i, Princeton Instruments) with an air-cooled CCD-camera (Newton, DU 920P BR-DD, Andor). To prevent backscattered photons from reaching and thus damaging the laser diode, a Faraday rotator (IO-5-NIR, Optics for Research Caldwell) is positioned between the diode and the optical band pass filters.

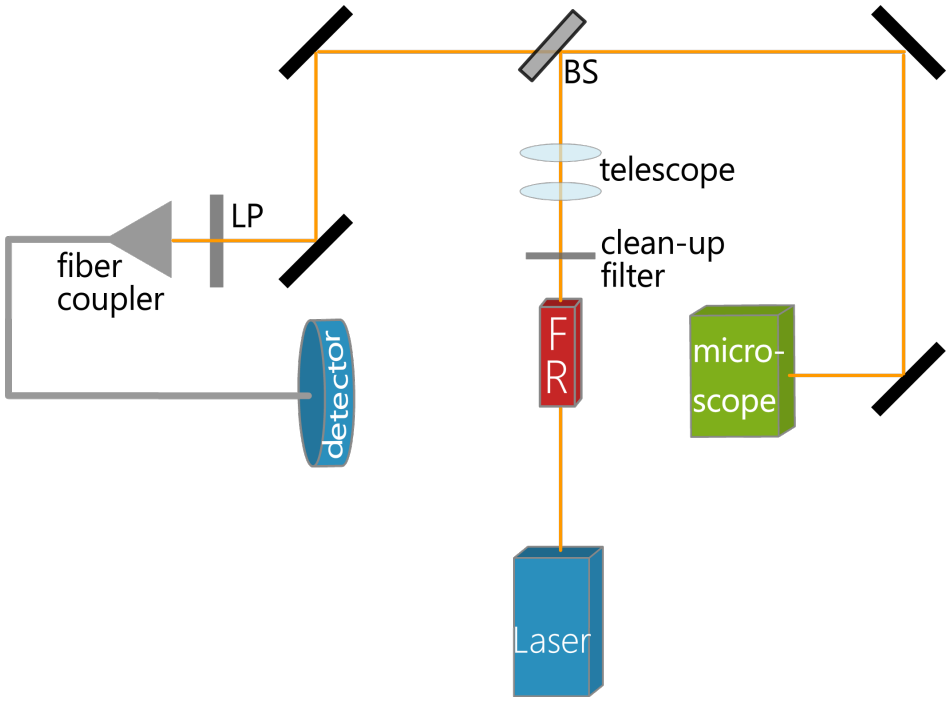

Figure 3.7: Setup of the micro-Raman system. The light of a laser diode (785 nm wavelength) is guided through a Faraday rotator (FR) and an optical band pass filter (clean-up filter). The light is focused onto the sample using a microscope. The backscattered light is collected by the microscope and passes the beamsplitter (BS) and a long pass razor-edge filter (LP) before being coupled into an optical fibre. The fibre guides the light into the detector, which consists of a monochromator and a CCD-camera.

3.6 Superparamagnetic Beads

For most of the experiments presented in this work, a low standard deviation of the bead size was required. If beads are to be agglomerated into ordered structures, the shape and size of each bead needs to be exactly defined, otherwise an ordered structure cannot be obtained. Furthermore, as discussed in section 2.2, unspecific interactions between beads hinder the experiments,

as agglomeration is supposed to be caused by magnetic interactions, not by van-der-Waals or Coulomb forces. Additionally, unspecific interactions can occur between beads and channel walls, leading to beads sticking to surfaces. Lastly, the volume of the beads - and therefore the magnetic moment - should be high enough to enable sufficient inter-bead forces under the influence of magnetic fields without causing a fast sedimentation on the bottom of the channel.

All these requirements are met by Dynabeads MyOne and M-280 SA, whose magnetic parameters have already been introduced in section 2.2. Thus, these were the preferred bead species selected for the experiments. The MyOne beads were available with a streptavidin or a carboxylic acid coated surface. As the carboxylic acid caused repulsive electrostatic forces between the particles, (mostly) preventing unwanted agglomeration, this functionalization was generally preferred over the streptavidin coating. However, when optical evaluation of single beads was necessary, the small size of the MyOne beads (1 µm diameter) posed a problem. Here, M-280 beads had to be used. As these are not available with a carboxylic acid coating, the streptavidin coated version was used.

4 SPS Formation Dynamics

When superparamagnetic beads are subject to a homogeneous magnetic field, they agglomerate into one-dimensional, chain-like suprastructures (see section 2.2.2). If the field is rotated in plane, the chains follow this rotation. Higher rotation frequencies lead to the formation of two-dimensional cluster structures. In many applications of these supraparticle structures (SPS) in microfluidic systems (see for example chapter 5 and 7), the shape and size of the agglomerates is a vital parameter. To control the shape and size of SPS, the dynamics of the formation process need to be understood. Ideally, a theoretical model would exist that can calculate the size, shape and formation velocity of SPS from the known material parameters of the beads. However, such a model is not easy to construct, as magnetic, fluidic and mechanical interactions need to be considered. To help in the construction of such a model, central questions about the formation process are approached experimentally. How does the initial formation of SPS depend on the parameters of the magnetic field and the bead concentration? What is the threshold frequency that separates the region of stable chains from the region of unstable chains that form clusters? To answer these questions, a series of experiments was performed to obtain information about the process dynamics. These experiments are presented in the following sections.

Furthermore, an experiment was performed where clusters were tried to be reformed into chain structures. This was necessary for the following reason: The significant advantage of the use of superparamagnetic beads as components in microfluidic systems is their ability to self-assemble into SPS under the influence of magnetic fields. A deactivation of the field leads to a decay of the structures. Thus, clusters and chains can be created and destroyed within, at most, a few tens of seconds. Furthermore, chains can be formed into cluster structures by an increase in the frequency with which

the field rotates. However, the reverse has, thus far, not been possible. A decrease in the rotation frequency does not return clusters to the chain form. Thus, a method to reform chain-like SPS from cluster agglomerates had to be developed.

4.1 Materials and Methods

The superparamagnetic beads used in the following experiments (Dynabeads MyOne and M-280) have been described in the theory chapter (section 2.2.2). The electromagnetic coil setup and the optical microscope have been introduced in section 3.4 and 3.3, respectively. Tween 20 surfactant was obtained from Sigma-Aldrich.

4.2 Experiments

In the following three experiments, central questions about the initial formation of SPS have been evaluated. In the first experiment, the initial formation of SPS under the influence of a magnetic field rotating at a fixed frequency was investigated. The varied parameters were the bead concentration, the field strength and the rotation frequency.

In the second experiment, the aim was to study the frequency threshold that separates the regimes of stable and unstable chain-like SPS. The frequency where chains become unstable and break or fold into clusters was evaluated based on the chain length.

In the final experiment, a method to reform cluster-SPS into chain-like SPS was developed. The purpose of this method is to complete the cycle of switching between free beads, chains and structures at will.

Note that the final size of clusters in concentration regimes such as the ones used in these experiments are usually significantly larger due to further agglomeration of clusters. However, studying the final clusters size was not the aim of these experiments. Therefore, the experiments only investigated the first few hundred seconds of SPS formation.

4.2.1 Evaluation of the Initial SPS Formation

In the first of the three experiments, a 2 µL droplet of a Dynabeads M-280 streptavidin (SA) dispersion (standard: 50 µg mL^{-1}, 0.1 % Tween 20[1]) was deposited on a glass substrate and placed within the electromagnetic coil setup described in section 3.4. As beads settle down on the glass surface over time during the experiment, a time period of two minutes was introduced prior to the activation of the magnetic field to ensure that all beads had settled on the substrate[2]. Otherwise, the overall amount of beads would have been time-dependent, as beads would continue to enter the area of focus just above the glass surface. After this waiting period, the rotating magnetic field (standard rotation frequency: 600 rpm, standard field strength: 90 Oe) was activated. Images were taken with the optical microscopy setup described in section 3.3 at a ×600 magnification after 0 s, 1 s, 3 s, 5 s, 10 s, 20 s, 40 s, 80 s and 160 s. Afterwards, the amount of SPS with X beads was counted, where X ranged from 1 to 10 beads, with every SPS larger than 10 beads being counted in the ≥ 10 category [3].

To test the influence of different parameters, the experiments were repeated varying the field strength (36 Oe, 63 Oe, 90 Oe and 117 Oe), the rotation frequency (60 rpm, 600 rpm, 6000 rpm and 60000 rpm) and the bead concentration (10 µg mL^{-1}, 20 µg mL^{-1}, 50 µg mL^{-1}, 75 µg mL^{-1} and 100 µg mL^{-1}).

Every experiment was repeated 10 times to increase the statistical significance of the resulting data.

1 The non-ionic surfactant Tween 20 (also called Polysorbate 20) was added to minimize unspecific, non-magnetic attractive forces between the beads.

2 Thus, the given concentrations of the bead dispersion differ from the actual concentration on the glass surface.

3 As SPS larger than 10 beads were not counted separately, an error in the total number of beads was created. This error is equal to (X-10)·$\#_{\geq 10}$, with $\#_{\geq 10}$ as the number of agglomerates of a size greater than 10 beads and X as the number of beads in such an agglomerate. However, as the amount of such agglomerates was always small compared to the total number of beads and such SPS hardly appeared earlier than 160 s into the measurement, the error was not significant.

4.2.2 Evaluation of the Frequency Threshold

A 0.5 µL droplet of a 1 % Tween 20 solution was deposited on a glass substrate. After 10 s, a 2 µL droplet of a Dynabeads M-280 streptavidin dispersion (125 µg mL^{-1}) was added. The substrate was put into the coil setup described in section 3.4. For 120 s, a constant, non-rotating field of 90 Oe was applied to the sample during which chain formation took place. Afterwards, a linear increase in the rotation frequency, going from 6 rpm to 600 rpm, was applied. The field strength (either 54 Oe, 90 Oe or 117 Oe) and the duration (either 180 s or 60 s) of this sweep were varied to test the influence of these parameters. During the experiment, the movement of SPS was observed (see section 3.3) at a ×600 magnification.

4.2.3 Reformation of Chain-like SPS from Clusters

In the third experiment, a 0.5 µL droplet of Tween 20 was deposited on a glass substrate and put into the magnetic coil setup (see section 3.4). 2 µL of a 100 µg mL^{-1} dispersion of M-280 SA beads *or* MyOne beads were added. Then, a constant magnetic field (50 Oe for the M-280, 40 Oe for the MyOne) directed in-plane was activated for a period of 90 s to form chain-like SPS (see Figure 4.9). After that, the rotation was activated, increasing the frequency linearly from a low rotation frequency (6 rpm) to a high rotation frequency (240 rpm), until small clusters were formed. Afterwards, the electronic signals for the coils were set so that one of the two sinusoidal signals had a constant offset (36 Oe for the M-280, 27 Oe for the MyOne), resulting in a superposition of a rotating field and a constant field[1]. This field lead to quick , jerky back-and-forth movements and fragmentation of the SPS (while rotational and constant field were orthogonal) and a reformation into chains (when the fields where parallel).

1 Note that the given parameters were the parameters that gave optimal results. The experiment was performed multiple times testing different values for each parameter.

4.3 Results and Discussion

In this section, the results of the previously described experiments will be presented and discussed in three separate sections. These results serve two purposes: For one, the M-280 beads are the model system on which many of the current applications are build. The results in the following sections provide a deeper understanding of the SPS formation in this model system, making it easier to develop further applications and to choose the optimum application parameters. Second, the obtained data can be used to build a theoretical model for the SPS formation that can be used to calculate formation rates, SPS sizes and shapes as well as SPS stability values. This would be very beneficial to tailor the SPS for specific applications. Such a model is not readily developed, as magnetic, fluidic and mechanical interactions need to be incorporated into the model. Possessing data to which the model can be fit is of great help for the development process.

4.3.1 Evaluation of the Initial SPS Formation

In this experiment, the time dependent development of the amount of SPS with a certain number of beads was evaluated. Figure 4.1 shows the results. The curve for SPS of 1 and 2 beads shows a decay that is exponential or hyperbolic at first glance, as it is characteristic for first or second order reactions, respectively. However, neither a first nor second order equation for the concentration can be fitted to this curve or the curve for single beads (which is not shown here). This shows that the rate law is - for unknown reasons - somewhere between first and second order. This is a surprising finding that can currently not be explained and requires further, theoretical study.

More information can be drawn from the curves for 3&4, 5&6 and 7&8 beads per SPS. They show the typical behaviour of intermediate states near the steady state condition. The steady state occurs when the intermediate is removed (through a reaction to products) faster than it is created (through a reaction by the reactants). In this case this means that the probability to build SPS from single beads is low and this event happens rarely, but once an SPS has been build it grows rapidly. This means that the process can be

described as being somewhat equivalent to the formation of crystal nuclei from monomers in a solution. There is a certain inhibiting threshold (in this case more kinetic than thermodynamic) that needs to be overcome. Once a nucleus is formed, it can grow rapidly until there is no more material in the vicinity that can be incorporated into the agglomerate. With further study, the system could possibly be used as a scaled-up model system for the formation of crystal nuclei.

In general, the rate of formation of larger SPS can best be seen from the development of agglomerates of one or two beads[1]. Thus, in the following sections, the figures show the development of the ratio of beads present as single beads and two-bead-agglomerates compared to the total number of beads.

Influence of the Rotation Frequency

According to the results of the experiments (presented in Figure 4.3), the rotation frequency has no significant influence on the rate with which SPS form. The differences between the four curves can be explained through statistical variations. This is supported by the fact that there appears to be no trend for different frequencies and the resulting ratio. Note, however, that although the initial rate of formation is obviously not affected, the shape of the resulting SPS is: Figure 4.2 shows two images taken at 160 s seconds at rotation frequencies of 60 rpm and 60000 rpm. It can clearly be seen that at low rotation frequencies the SPS form chains, while higher frequencies cause a reformation into cluster structures. Therefore, although the formation rate does not differ, the final SPS size and shape will.

1 Agglomerates of two beads were included as the initial sample in the absence of a magnetic field already contained up to 10 % of agglomerates of two beads. This was caused by unspecific attractive forces between the beads that could not be completely cancelled by Tween 20. The use of carboxylic acid coated beads would have solved this problem, but as the M-280 beads are not available with this functionalization and the MyOne beads would have been too small to resolve them optically, the use of M-280 SA beads presented the best available compromise.

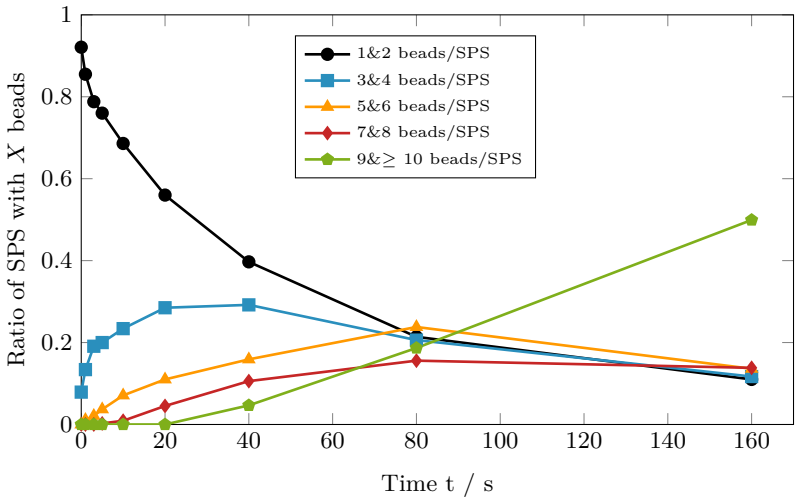

Figure 4.1: Formation dynamics of SPS structures under the influence of a rotating magnetic field. SPS consisting of X beads (see legend) form and are incorporated into larger SPS. The experiment was performed with a bead concentration of 100 µg mL^{-1}, a magnetic field strength of 90 Oe and a rotation frequency of 600 rpm.

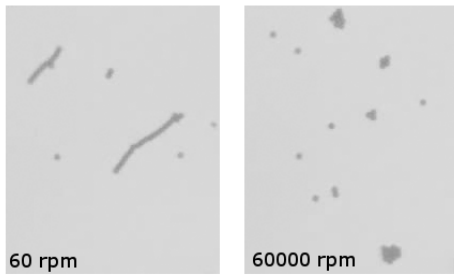

Figure 4.2: Microscopy image of the SPS shapes after 160 s at a rotation frequency of 60 rpm (left) and 60000 rpm (right). It can clearly be seen that at low rotation frequencies, the SPS remain in the chain formation.

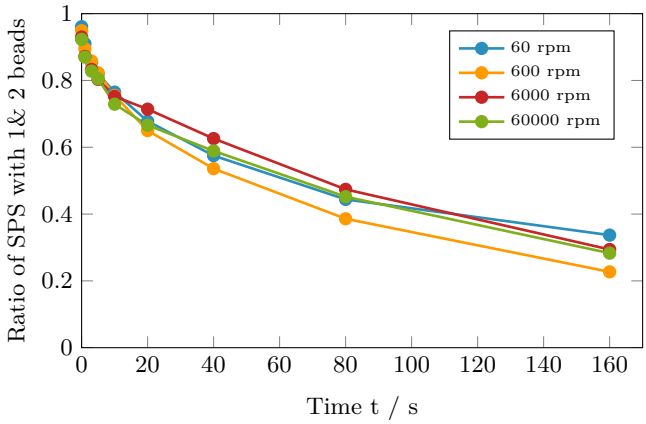

Figure 4.3: Influence of the rotation frequency on the SPS formation rate. The y-axis gives the ratio of beads that are present as single beads or 2-beads-SPS compared to the overall number of beads. The data was collected at a magnetic field strength of 90 Oe and a concentration of 50 µg mL^{-1}.

Influence of the Field Strength

A higher field strength induces a larger magnetic moment in the superparamagnetic beads, which in turn leads to an increase in the attractive forces between the particles (see section 2.2 for details). Thus, a higher field strength should favor the rate of SPS formation. This is reflected in the results of the experiment, presented in Figure 4.4. The higher the magnetic field strength, the faster beads form into SPS. However, the influence is not as strong as would be expected when considering that according to equations 2.15 and 2.16, the length L of an SPS chain is proportional to the field strength H. When the field strength is doubled (from 63 Oe to 117 Oe), the final ratio at 160 s only decreases from 30 % to 22 %[1]. However, equations 2.15 and 2.16 apply to SPS structures that are already

1 The results from the 36 Oe curve were not used for this comparison as the starting SPS composition differs strongly from the rest of the experiments, with only 78 % of the beads present as single beads or 2-bead-agglomerates.

formed and where interactions take place between adjacent beads. In this experiment, beads interact over a distance (single beads are attracted by other beads or SPS). As the magnetic stray field decays rapidly with the distance between the beads, it doesn't surprise that the influence of H is weaker than when considering the interactions between adjacent beads. Thus, although a trend is visible, it can be said that the field strength does not have a strong influence on the SPS formation dynamics.

Influence of the Bead Concentration

Compared to the magnetic field strength, the concentration of beads in the dispersion has a stronger influence on the SPS formation rate. As can be seen from Figure 4.5, doubling the concentration (from 50 µg mL^{-1} to 100 µg mL^{-1}) decreases the final ratio after 160 s from 61 % to 11 %. The complete set of curves shows a general trend for a faster formation at high concentrations, which doesn't surprise as a higher concentration means a lower interbead distance, thus increasing the chance that two magnetized

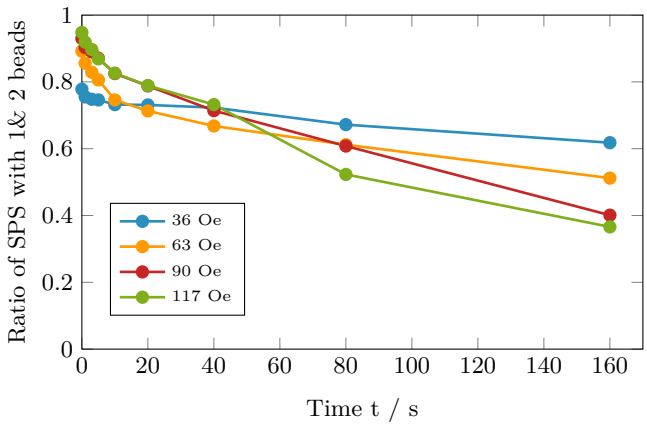

Figure 4.4: Influence of the magnetic field strength on the SPS formation rate. The y-axis gives the ratio of beads that are present as single beads or 2-beads-SPS compared to the overall number of beads. The data was collected at a rotation frequency of 600 rpm and a concentration of 50 µg mL^{-1}.

beads attract each other and agglomerate.

It is noteworthy that below a concentration of 20 µg mL^{-1} no noticeable SPS formation takes place within the 160 s. This shows that there is a lower threshold for SPS formation, below which SPS formation can be prevented. To evaluate this threshold for microfluidic applications and use it to prevent unwanted agglomeration, however, the experiment would have to be repeated measuring the SPS formation in the liquid volume, not on the glass surface.

4.3.2 Evaluation of the Frequency Threshold

SPS chains that formed in the initial formation step rotated at an increasing rotation frequency until the chain became unstable and collapsed. This collapse either took the form of a fragmentation of the chain or a folding into a cluster structure. The experiments showed that there is no definite, sharp frequency threshold at which the chains become unstable. However, a region of transition does exist. In this region, chains become metastable and

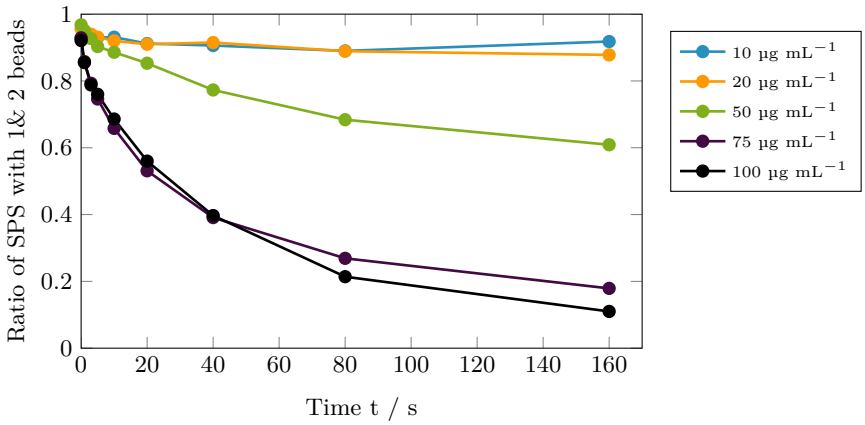

Figure 4.5: Influence of the bead concentration on the SPS formation rate. The y-axis gives the ratio of beads that are present as single beads or 2-beads-SPS compared to the overall number of beads. The data was collected at a magnetic field strength of 90 Oe and a rotation frequency of 600 rpm.

will finally fracture or form into clusters. In the experiment, chains were observed until this fragmentation or reformation occured. The frequency at which this event happened was recorded as the threshold frequency for this SPS. Figure 4.6 shows the mean frequency averaged over a few tens of SPS in dependence of the chain length for different field parameters. It can clearly be seen that although there is no *sharp* transition between the stable and the unstable configuration, the fracturing does occur in a region of specific frequencies that depends on the chain length. This region represents a *diffuse* threshold [1]. As can be seen from the graph, the threshold depends strongly on the magnetic field strength. Doubling the field strength from 54 Oe to 117 Oe increases the threshold frequency by an amount of between 80 % an 140 % [2]. A stronger magnetic field increases the magnetic moment of the beads. This, in turn, increases the attractive forces that restore the beads to their positions within the chain, thus making the chain more stable.

However, a dependency on the velocity of the frequency increase (*sweep velocity*) exists as well, as can be seen from the fact that the curve for a sweep time of 60 seconds (blue, dashed) is significantly above the curve for a sweep time of 180 s (blue, solid). At first, the reasons for this are not obvious. The threshold frequency should not depend on the sweep velocity. Chains should either be stable or unstable at a certain frequency. However, this experiment is a kinetically controlled experiment where chains enter a metastable state, from which they fracture or fold within an unknown time, somewhat resembling the kinetically controlled freezing of liquid droplets below the freezing point (*supercooling*)[113,114,115,116]. Like with supercooling, the sweep time becomes an important factor for the measured threshold of transition. In this case, there are two main effects that influence the measured frequency of transition:

1 Note, however, that the formation of clusters can take place at frequencies below this threshold. In this case, the clusters are not formed by instabilities of the rotating chains but through chain-collisions that result in cluster structures that do not reform into chain structures.

2 Although this suggests a direct proportionality at first glance, theoretical calculations predict it to be quadratic, as will be discussed later in this section.

An increase in the transition frequency is caused by the fact that, in this experiment, the frequency was not increased step-wise, but linearly. When chains become un- or metastable, they do not fracture immediately. Rather, they continue to exist for a certain time while gradually becoming more and more unstable. As this time is random within certain boundaries, the final frequency at which the chain fractures or folds is higher than the frequency at which the chain became unstable. This effect thus shifts the average threshold frequency towards higher values and is increased by a higher sweep rate. To negate this effect, the frequency would have to be raised by tiny steps, checking for unstabilities at each step, taking a suitable waiting period into account that ensures that metastable chains will fracture or collaps within this time. This, however, is impractical from an experimental point-of-view, as the evaporation of the droplet limits the duration of the experiment. Thus, a suitably long sweep time of 180 s was chosen for the experiments, after which the droplet started to significantly decrease in size due to solvent evaporation.

A decrease in the transition frequency is caused by another effect that is connected with the agglomeration of chains into larger SPS. For each SPS, there is a finite chance that it will collide with another SPS, thus forming a cluster structure. The longer the SPS exists, the higher the chance that it will have collided and agglomerated before undergoing a fracturing or folding event. Thus, long-living chains have a high chance of being removed from the experiment before they have a chance to fracture. For short-living chains, this probability is smaller. Due to the asymmetry of this probability effect, the average transition frequency is shifted towards lower values. A higher sweeping velocity negates this effect, as the duration of the experiment is significantly shortened, lowering the chance for SPS agglomeration. This then shifts the average frequency towards higher values if higher sweep times are employed.

Together, these two effects lead to an increase in the average threshold frequency with higher sweep velocities. This explains the trend found in the experimental data presented in Figure 4.6.

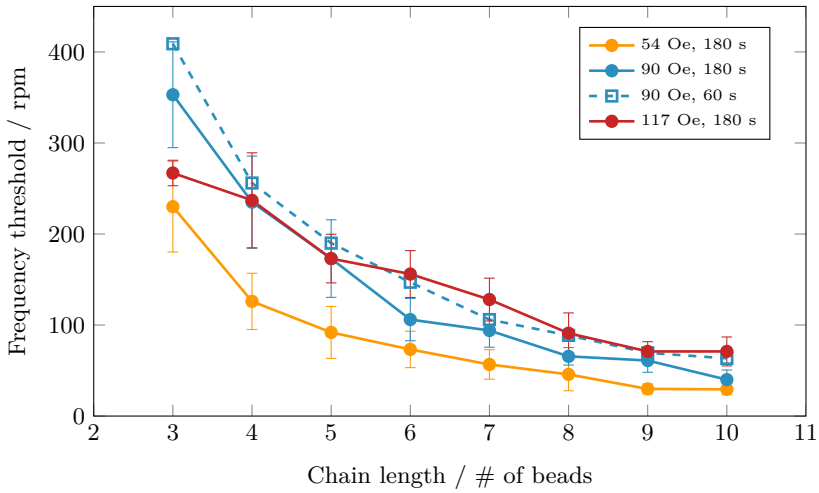

Figure 4.6: Average threshold frequency plotted against the chain length, given as the number of beads per chain. The threshold frequency gives the frequency at which chains of length X fracture or fold into cluster structures. Note that the error bars in the figure give the root mean square deviation calculated from the data, not the actual error of the measurements. The error bars for the 60 s curve were omitted for the sake of clarity.

Correlation between Rotation Frequency and Mason Number

According to the works of Petousis *et al.*[42] and Melle *et al.*[41], the length L of the SPS chains should be proportional to the inverse square root of the Mason number (see equation 2.16). Together with the definition of the Mason number in equation 2.15, this yields

$$L = \alpha \sqrt{\frac{\mu_0 \chi^2 H^2}{16 \eta \omega}} \tag{4.1}$$

with μ_0 as the vacuum permeability, χ as the magnetic susceptibility, H as the magnetic field strength, η as the viscosity of the liquid, ω as the angular velocity of the field and α as the constant of proportionality. Equation 4.1

can be solved for ω:

$$\omega = \alpha^2 \frac{\mu_0 \chi^2 H^2}{16\eta L^2} = \beta(\chi,H,\eta) \cdot \frac{1}{L^2}. \tag{4.2}$$

As long as the magnetic field is not strong enough to saturate the beads, χ can be seen as a constant (see the linear development of the magnetization curve in Figure 2.5 at low field strength). As the liquid itself is not changed, the viscosity η remains a constant as well. Thus, $\beta(\chi,H,\eta)$ becomes $\beta(H)$, with a quadratic dependency on H (see equation 4.2).

Figure 4.7 shows a plot of the obtained values of ω against L^{-2}. According to equation 4.2, this should yield a straight line with a slope proportional to H^2. As can be seen from the graph, this is indeed the case, with the exception of the 117 Oe curve, where the last data point significantly deviates from a straight line. This data point corresponds to the threshold frequencies of 3-bead-SPS, a value that is associated with a severe measurement error. Although Figure 4.6 shows a low standard deviation for this value, this is only true because of a low amount of data, as only three SPS of this structure could be evaluated in this experiment. The reason for this lack in data is the same reason that pushes the observed frequency below the expected one: 3-beads-SPS are very stable, especially at high field strengths, thus they fragment at high frequencies, i.e. at late stages of the experiment. The chance that they are subjected to an agglomeration with other SPS before becoming unstable is high. Thus, only unstable 3-beads-SPS that fragment early were observed. This problem was significantly less intense with 4-bead-SPS and, thus, didn't justify additional experiments to obtain more detailed data. To ensure that the influence of this data point doesn't reduce the data quality, it was excluded from the further evaluation.

To obtain $\beta(H)$, the lines were fit with linear functions with a set root of $y = 0$, as long chains (high L, low L^{-2}) should break at disappearing values of ω. The corresponding fit functions are presented in Figure 4.7. Table 4.1 shows the values that were obtained for $\beta(H)$. To further test the theoretical concept, it was tested whether $\beta(H)$ is indeed proportional to H^2. The resulting fit can be seen in Figure 4.8. If the data points are fitted with a line fit without further boundary conditions, the resulting function

is given as $\beta = (0.21051 \pm 0.0264)\ \mathrm{rpm/Oe^2} \cdot H^2 + (1605 \pm 247)\ \mathrm{rpm}$. This line fit represents the data very well and would thus confirm the hypothesis. However, for $H = 0$, $\beta(H)$ should also be 0. If this is taken as the boundary condition, the equation becomes $\beta = (0.36209 \pm 0.0579)\ \mathrm{rpm/Oe^2} \cdot H^2$. Although this curve is a significantly worse fit, it is still in line with the hypothesis, considering the range of error that is expected from these calculations.

4.3.3 Reformation of Chain-like SPS from Clusters

In this experiment, it was tried to reform clusters of M-280 and MyOne beads into chains by applying a superposition of a rotating and a static magnetic field. The experimental steps are presented in Figure 4.9. As previously mentioned, the parameters given for field strength, offset and rotation frequency were optimized to the values given in the experimental section.

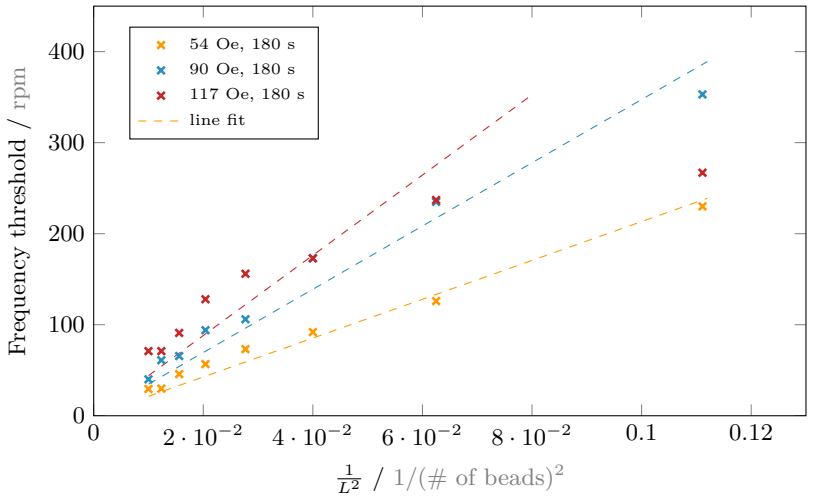

Figure 4.7: The threshold frequency plotted against the inverse square of the chain length. In accordance with the literature[42,41], the plot gives straight lines, showing that L is indeed proportional to the inverse square root of Mn.

Table 4.1: Values for $\beta(H)$, obtained through linear fits as shown in Figure 4.7. Note that L was not given in unities of a length, but as multiples of the length of a bead. This yields $[\beta]$=rpm.

Field strength/ Oe	$\beta(H)$/ rpm
54	2133
90	3474
117	4407

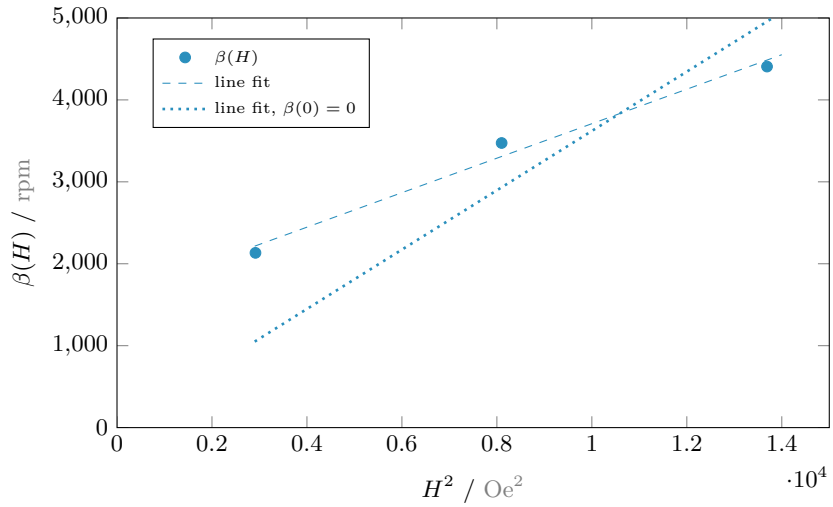

Figure 4.8: Plot of the obtained values for $\beta(H)$ against the square of the field strength, H^2. The lines represent the two different line fits with and without the boundary condition of $\beta(0) = 0$, as discussed in the text.

For the M-280 beads, the parameters resulted in an incomplete reformation. Although clusters are elongated and take on a chain-like shape, only a minor fraction returns to a state where the width is equal to one bead (see Figure 4.10). Furthermore, the tolerance for different values of the parameters is quite low. Changes of more than 5 Oe in the field strength or the offset for the reconstruction gave no reformation effect. Nevertheless, a change in the SPS structure is visible and is achieved within tens of seconds.

For the MyOne beads, the results are significantly more positive. Here, the experiments showed a very good reformation effect that is able to restructure clusters of a few tens of beads into chains within a few seconds (see Figure 4.11) with high efficiency. Although not every cluster is reformed, the low amount of remaining small clusters that end up attached to the ends of chains is negligible. Larger clusters of more than a few dozen beads, however, need to be disassembled through a deactivation of the magnetic field for a few seconds before reorganization into chains can take place.

It can be theorized that the lower attractive forces between the MyOne beads (compared with the M-280 beads) favor the successfull restructuring of the SPS. To reform clusters to chains, magnetic bonds between the particles must be broken. While the bonds are broken, the beads have to move into a different position so that when the field returns to the direction of the chain axis (during the reformation), the beads can arrange in a new way. Both processes favor the MyOne beads, as their magnetic

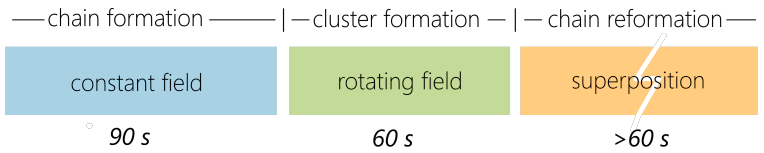

Figure 4.9: Schematics of the chain reformation process. In a first step, a constant magnetic field in-plane with the surface of the glass substrate is applied to form chain-like SPS. Then, the field is rotated to form cluster structures. In the last step, a constant offset is added to one of the two sinusoidal input signals that create the rotation, resulting in a superposition of a constant and a rotating magnetic field. This leads to a kind of jerking movement that regularly fragments and rebuilds the agglomerates, thus reforming the chains.

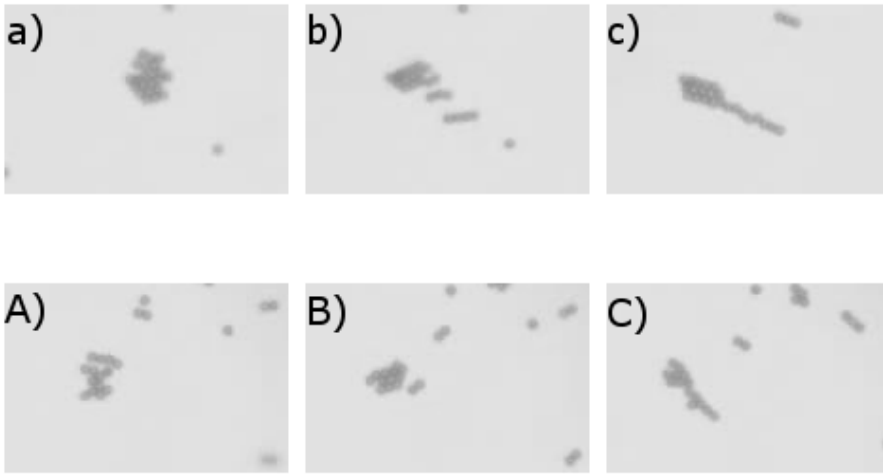

Figure 4.10: a),A) Initial state of cluster-like SPS made from M-280 SA beads after the rotational field is switched off ($t = 0\ s$). b),B) State of the SPS during the moment of approximately 90° angle between the fields ($t = 7.1\ s$). The SPS break apart due to the jerky movement of the magnetic field that the whole chain itself cannot follow in time. c),C) Chains reformed from the cluster structures under the influence of the superpositioned fields ($t = 14.9\ s$).

interaction is weaker while their movement is promoted by their lower mass. Thus, agglomerates of beads that are smaller than MyOne beads will probably be even more easy to restructure. The theory is supported by the fact that a restructuring of M-450 beads (higher mass and stronger magnetic interaction than the M-280 beads) was found to be impossible by the presented method.

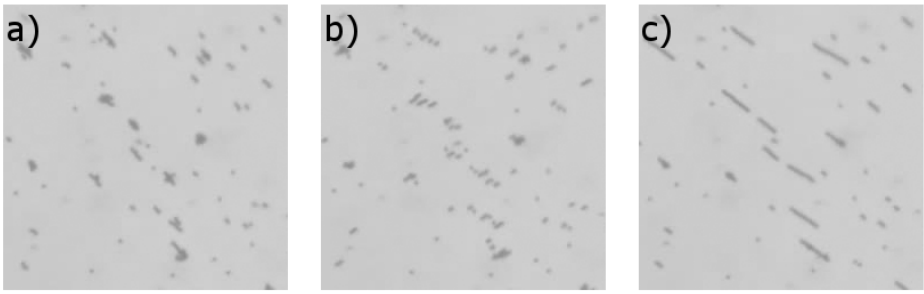

Figure 4.11: a) Initial state of cluster-like SPS made from MyOne beads after the rotational field is switched off ($t = 0\ s$). b) State of the SPS during the moment of approximately 90° angle between the fields ($t = 1.2\ s$). c) Chains reformed from the clusters structures under the influence of the superpositioned fields ($t = 3.6\ s$). Compared to the reformation of the M-280 chains, the MyOne beads restructure significantly faster. Furthermore, chain-reformation is nearly complete.

4.4 Conclusion

In the experiments presented in this chapter, the basic groundwork for further insight into the formation of SPS has been built. The basic parameters for the formation have been evaluated. The findings indicate that the frequency at which the field rotates only influences the shape of the SPS and not the rate of initial formation. The latter is influenced by the field strength (weak influence) and the bead concentration (strong influence). Furthermore, a diffuse frequency threshold was found, above which rotating chains become unstable and fracture or form into cluster structures. It was shown that the finding by Petousis *et al.*[42] and Melle *et al.*[41], that the SPS length is proportional to the inverse square root of the Mason number, could be reproduced in this experiment. The data gathered in this work can now be used as the basis of theoretical simulations that give further insight into the mechanism of SPS formation. Once a model for the behaviour of SPS under the influence of rotating magnetic fields in microfluidic channels has been developed, it can be applied to a variety of bead species, thus

giving a tool to choose the optimum bead species and working parameters for specific applications.

In addition, a reformation process that reforms clusters into chains has been developed. With this, superparamagnetic beads can be assembled into cluster or chain SPS within a microfluidic network without need for a disassembly in between. This makes the use of beads as self-assembling matter significantly more feasible and flexible.

4.5 Outlook

The next step would be to build a theoretical model of the formation process and use the data obtained in this work to calculate critical parameters. With such a model, it would be possible to predict the self-assembly of superparamagnetic beads in general and - ideally - under diverse conditions. This would be very helpful in developing microfluidic applications where the self-assembly of beads is utilized for specific functions.

Furthermore, the process of initial SPS formation from single beads could be used as a model system for the formation of nanoparticle nulei. Some of the basic mechanisms in the SPS formation match the mechanism of nanoparticle formation, namely the agglomeration of monomers into a nuclei and the existence of an energy difference between the free monomers and the agglomerated state. However, this would require further study, as a critical parameter of nuclei formation in nanoparticle chemistry is the detachment of monomer molecules from the nuclei, which results in the dissolving of nuclei that are below a critical size. A detachment of particles from SPS nuclei, however, has not been observed in the experiments. A way to obtain such a mechanism in the SPS experiments would have to be found to obtain a suitable, macroscale analogy. One possibility would be to use a dense dispersion of MyOne beads, in which larger M-280 beads would be introduced. The forces between the M-280 would be higher than between M-280 and MyOne beads, thus the M-280 would agglomerate. However, the total energy of single M-280 beads dispersed in the MyOne matrix would only be slightly higher than that of agglomerated M-280s. Thus, the energy barrier would be low and could be overcome by fluctuations in the

system, as introduced by the rotating field. Thus, there could be a finite possibility for an SPS nuclei to dissolve. Then, the system could serve as a 2D-analogon to further study the initial nuclei formation in nanoparticle chemistry.

5 Utilizing SPS structures for colloidal separation and enhanced mixing

As introduced in section 2.2.2, superparamagnetic beads form supraparticle structures (SPS) under the influence of magnetic fields. If the magnetic field is homogeneous and non-rotating, these SPS take the form of one-dimensional, chain-like structures. These structures can be rotated if the field rotates in-plane at small frequencies below a few hundred rounds per minute, depending on the bead species used. Above a critical threshold, the chains collapse due to shear forces during the rotation and form two-dimensional clusters.

The agglomeration of beads into SPS opens up interesting applications as self-assembling matter for the execution of tasks in microfluidic systems. In this experiment, the formation of SPS is employed to create a system capable of colloidal separation. Figure 5.1 shows a sketch of the basic mechanism. Superparamagnetic beads agglomerated into SPS are guided into one of two diverging channels by the sterical interaction between the rotating structures and the wall separating the two channels. Depending on the direction of rotation, the structures can be guided into the lower (clockwise) or upper (counter-clockwise) channel. Thus, the bead flow can be limited to one of the two channels if the guiding efficiency lies at 100 %. If no external magnetic field is applied, the beads will be distributed equally over both channels.

This effect can be used for a continuous-flow separation procedure. If two laminar flows meet at a T-intersection, they will continue as two parallel streams with a small boundary layer between them. Due to the laminar flow behaviour, thermal diffusion is the only driving force for mixing. Thus, if one of the streams contains large molecules with low diffusion coefficients, such as DNA or large proteins, these will not cross over into the other stream.

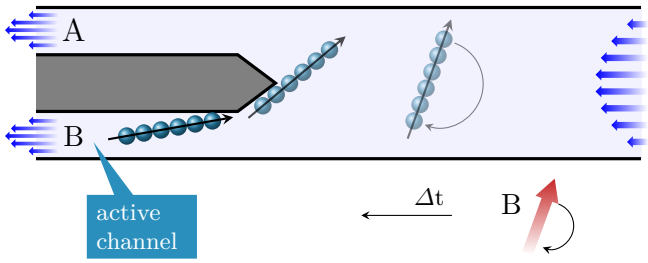

Figure 5.1: Basic principle of the guiding mechanism. Supraparticle structures of superparamagnetic beads rotate while flowing through the channel. As they interact with the separation barrier that separates two diverging channels, they are pushed into the lower channel. Thus, bead flow can be restricted to one of the two channels, depending on the direction of rotation. The figure was taken from Eickenberg *et al.*[117].

The SPS guiding effect can then be used to guide macromolecules that bind to the bead surface into the "clean" stream where no other biomolecules are present, thus separating the analyte molecules from the background matrix (see Figure 5.2 for a sketch of the basic principle of this separation procedure). Such a separation mechanism could be employed wherever a continuous-flow detection is necessary, e.g. when controlling the quality of a water supply. In contrast to non-continuous, batch-based methods, where the microfluidic chips are usually designed for single-use, this method would not require an exchange of the detection chip for each detection. Thus, it would be ideally suited for applications in remote locations, where an exchange of the chip supply is difficult or expensive.

To show that the proposed structure would be capable of the selective separation of DNA, beads or even cells, a proof-of-principle experiment for the separation application was performed. Superparamagnetic beads with streptavidin functionalization were used to bind biotin-functionalized non-magnetic particles in the main channel region and guide them into a selected channel.

As a side-effect of the rotation, it can be shown that the SPS act as local stirring devices, locally enhancing the mixing between streamlines in the upper and lower channel region by convection. In contrast to

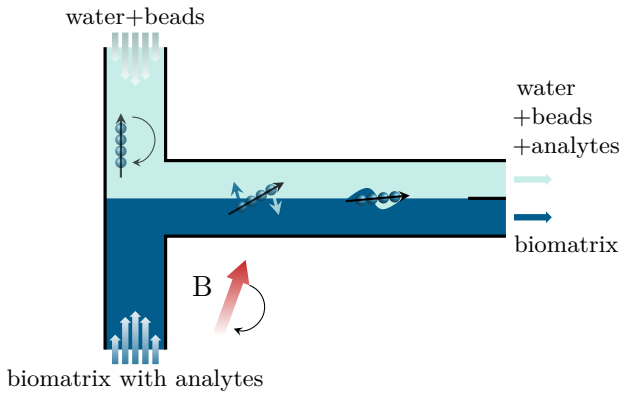

Figure 5.2: SPS guiding effect for bioseparation. Under the influence of a rotating magnetic field, the sample stream and the bead flow are joined at a T-intersection. The rotating bead suprastructures bind analyte molecules from the sample stream to their functionalized surface. At the separation barrier, the SPS with the bound analytes are guided into the aqueous flow and are thus separated from the sample stream.

common active mixing devices (see section 2.1.4), the proposed structure utilizes free-flowing, dynamically assembled SPS which are not restricted to a certain region of the device. This significantly lowers the device complexity, as neither specific mixing chambers nor on-chip power supplies (e.g. electromagnets) are required. As an alternative to the separation procedure described in the previous paragraph, rotating SPS could be used as free-flowing mixing devices. However, since the mixing effect is local, the SPS concentration in the dispersion has to be sufficiently high. Large volumes without SPS would decrease the mixing efficiency. To evaluate the degree to which rotating SPS enhance mixing, an experiment with two co-flowing streams of a bead dispersion and a dye was performed.

5.1 Materials and Methods

Using the soft-lithography methods described in section 3.1, a channel system consisting of two inlet reservoirs I_1 and I_2 and an outlet reservoir

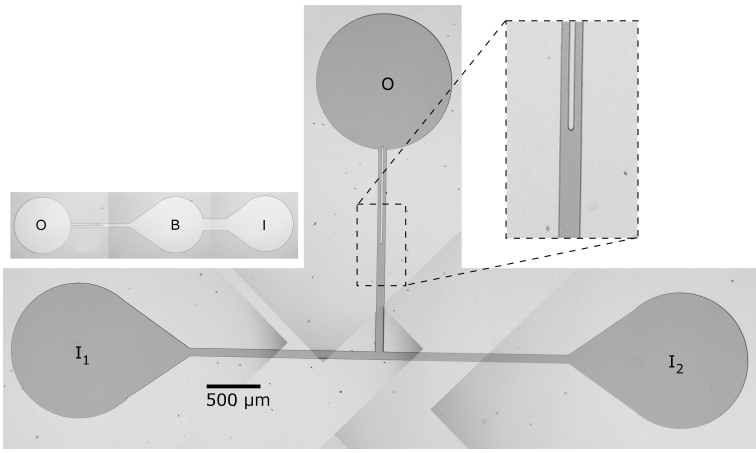

Figure 5.3: SU-8 3025 casting master for the microfluidic structure. Bead dispersions or aqueous solutions can be inserted into the inlet reservoirs I_1 and I_2. In the main channel between the T-intersection and the outlet reservoir O, a separation barrier splits the main channel into two parallel daughter channels. The guiding events take place in this separation area (right inset). For the basic evaluation of the guiding efficiency, a simpler design without the T-intersection was used. A demagnified image of this structure is shown in the inset on the left. The actual size of the reservoirs remained unaltered. In this design, beads were inserted into inlet B. As a permanent separation of the flows is not necessary for the evaluation of the guiding efficiency, the daughter channels were merged in the outlet reservoir. Fluid flow was achieved by adding water through the inlet reservoir I. The pictures are composed of several microscopy images and were taken from Eickenberg *et al.*[117].

O (each with a diameter of 1.4 mm) was designed. The basic design of the microfluidic structure is shown in Figure 5.3. Fluid flow between the inlets and the outlet was achieved through hydrostatic pressure. The bead dispersion was added *via* hand-operated µL pipettes. The inlet reservoirs are connected to a T-intersection by channels of 67 µm width. The subsequent main channel of the same width is split into two channels of 22 µm width that lead to the outlet reservoir. The overall channel height is 18 µm. To test the effect of an altered channel geometry, an alternative structure with a main channel width of 79 µm and a height of 14 µm was created. To

evaluate the device efficiency, a simpler design (see inlet in Figure 5.3) without T-intersection was prepared. Here, beads were inserted into a bead reservoir B. In all designs, the split channels were merged again downstream, as a permanent separation of the flows was not needed for the evaluation of the separation efficiency. Fluid flow was achieved by adding water through the inlet reservoir I in a way that the fluid flow swept the beads out of reservoir B.

The magnetic field for the experiments was supplied by the IKA RCT basic magnetic stirrers described in section 3.4. The reason for this was that strong attractive forces between the beads of an SPS are required to ensure stability during the interaction between the SPS and the separation barrier. Stronger magnetic fields increase the magnetic moment of the particles, which in turn creates stronger forces according to equation 2.12. Therefore, the IKA stirrers with their higher field strength were preferred over the smoother rotation of the Helmholtz coils.

The observation of the experiments was performed with the reflection microscope that was introduced in section 3.3.

Dynabeads MyOne (life technologies) with a carboxylic acid surface, a diameter of 1.05 µm and a standard size deviation of 1.9 % were used for the experiments. These beads were chosen for the properties of their functionalized surface. The negative surface charges help to prevent non-magnetic attractive interactions between the beads. To proof the applicability of the guiding effect for the separation of biomolecules or cells, MyOne beads with streptavidin surface and biotin coated polystyrene particles (Sphero Biotin, Spherotech 3.0-3.4 µm diameter) were used.

To evaluate the mixing performance of the SPS, a solution containing 65 mM flavin adenine dinucleotide (FAD) was prepared.

5.2 Experiments

Three different experiments were performed to test the efficiency of the proposed device. First, the dependency of the guiding and separation efficiency on the operation parameters was tested. For this, different parameters for flow velocity, magnetic field strength, channel dimensions

and rotation frequency were applied and evaluated for their efficiency[1].

In a second experiment, the enhancement of the mixing between two co-flowing streams by the rotation of SPS in the channel was tested using an FAD solution.

Lastly, the concept of SPS guiding was tested as a method of colloidal separation of non-magnetic particles. In this proof-of-principle experiment, biotin-coated particles were separated from their dispersion stream through interaction with SPS of streptavidin-coated MyOne beads.

5.2.1 Guiding and Separation Efficiency

A dispersion of MyOne beads with carboxylic acid coating at a concentration $c = 120$ µg mL^{-1} or $1.2 \cdot 10^8$ beads mL^{-1} was introduced into the inlet reservoir. After a time interval of two minutes, during which bead chains formed under the influence of the magnetic field of the permanent magnet inside the stirrer, the rotation of the magnetic field was started. A few seconds afterwards, a fluid flow was induced between the inlet and the outlet reservoirs by adding small amounts of water to the inlet reservoirs. The amount of water depended on the desired flow velocities and was usually on the order of 100 nL to 1 µL.

The experiment was observed optically. Videos of the SPS behaviour in the separation region were collected and evaluated using the following procedure: The amount and the visible surface area (in pixels) of chains *(=width of one or two beads, length>half the channel width)*, clusters *(=width of more than two beads, length>half the channel width)* and fragments *(length<half the channel width)*[2] passing through each channel were counted separately. If an SPS fractured at the separation barrier, it was categorized as *broken* and counted as flowing through both the upper and the lower channel. The area of these fragments was measured individually. The

1 A part of these experiments was performed by Patrick Stohmann within the frame of his Bachelor thesis. The corresponding results are indicated in the Results and Discussion section.

2 See Figure 2.7 in section 2.2.2 for more information on the definition of the *chains* and *cluster* shapes.

efficiency of the guiding effect was evaluated by calculating the ratio of the SPS pixel areas counted for channel A and B, assuming that the cluster structures were indeed two-dimensional monolayers [43]. For each flow velocity interval (see Results and Discussion for more detail on the chosen intervals), a few hundred SPS were observed to obtain statistical significance. The sample size was highest (500-1000 counted SPS) for flow rates where SPS fragmentation was an issue, as these showed the highest variation in guiding efficiency.

Due to the spatial variation of bead density in this experiment (caused by the agglomeration), the number of SPS passing the separation region per time varied strongly, not only depending on the flow velocity. However, this did not significantly affect the device efficiency, as clogging of the channels could not be observed. Even high bead densities could be handled by the device (see Figure 5.4).

To examine the influence of different parameters on the device efficiency, the experiment was carried out using two different magnetic field strengths (maximum field strengths of 330 and 690 Oe), two different geometries of the main channel (67×18 µm^2 and 79×14 µm^2; both channel geometries allow approximately the same volume flow rate at equal pressures), rotation frequencies between 50 and 250 rpm and flow velocities up to 600 µm s^{-1}.

5.2.2 Mixing Efficiency

To test the mixing efficiency of rotating SPS in microfluidic channels, the boundary between parallel flows of an FAD solution and a bead dispersion containing rotating SPS was observed. For this, the inlet reservoir I_1 was filled with a MyOne carboxylic acid disperion of $c = 120$ µg mL^{-1} or $1.2 \cdot 10^8$ beads mL^{-1}. The inlet reservoir I_2 was filled with a 65 mM FAD solution. Fluid flow and rotation of the magnetic field were activated after a time period of two minutes during which chain formation took place. The experiment was observed optically.

5.2.3 Free-Flowing SPS for Particle Separation

For this experiment, MyOne beads with a streptavidin surface functionalization at a concentration of $c = 1$ mg mL^{-1} or $9.7 \cdot 10^8$ beads mL^{-1} were introduced into the inlet reservoir I_1. Inlet reservoir I_2 was filled with a 0.5 % w/v dispersion of Sphero Biotin beads with a biotin functionalized surface. After a time interval of two minutes, during which bead chains formed in the reservoir I_1, the rotation of the magnetic field (330 Oe, 60 rpm) and the fluid flow (at a flow velocity of 650 µm s^{-1}) were started. Under equilibrium condition, two parallel flows developed in the main channel, one transporting the (rotating) SPS, the other one transporting the Sphero Biotin beads. The bead dispersion and the particle dispersion were flowing parallel with a flow boundary in the center of the channel (see Figure 5.2). During this state, the experiment was observed optically at the separation barrier.

5.3 Results and Discussion

In this section, the results of the previously described experiments are presented and discussed. The section is divided into four subsections. In the first three sections, the results of the previously described experiments are discussed. In the first section, the general influence of different device parameters on the guiding and separation efficiency is evaluated. The following section discusses the results of the bioseparation experiment in which non-magnetic biotinylized particles were captured and separated by magnetic streptavidin bead SPS. In the third section, the degree of mixing between parallel flows caused by the rotation of SPS is investigated. In a final section, the proposed mechanism of separation is compared with common magnetophoresis.

5.3.1 Guiding and Separation Efficiency

The rotation of the magnetic field leads to a rotation of chain, cluster and fragment SPS inside the channel system. When SPS contact the separation barrier while rotating, the steric interaction guides them into the activated

channel (channel B). This way it is possible to selectively guide the SPS into one of the two channels, separating them from the other flow. The experiments showed that even high local bead densities can be guided without clogging of the channel (see Figure 5.4).

Figure 5.5 shows a series of optical images taken during the experiment that illustrate the possible events when bead agglomerates pass the separation region: At low flow velocities below 100 µm s^{-1}, the majority of chains (Figure 5.5 (a)) and clusters (Figure 5.5 (b)) is successfully guided into the correct channel by interaction with the separation barrier. As the flow rate is increased, fracturing of chains (Figure 5.5 (c)) and later clusters (Figure 5.5 (d)) starts to decrease the separation efficiency. Additionally, events where SPS do not complete a 180° rotation before passing the separation region (see Figure 5.5 (e)) effect the efficiency at high flow velocities of a few hundred micrometers per second.

SPS that span less than half the channel width (*fragments*) usually do not interact with the separation barrier (see Figure 5.5 (e)) and are therefore not subject to the guiding effect. However, they do not significantly lower the separation efficiency as the amount of beads per fragment is rather low. The presence of fragments is caused by movement of clusters in the

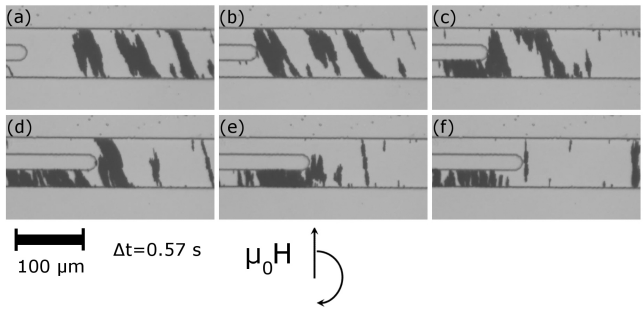

Figure 5.4: Optical images of the guiding effect at high bead densities. Even at high bead densities, large SPS structures are successfully guided into channel B by interaction with the separation barrier. The time interval between the images is 0.57 s.

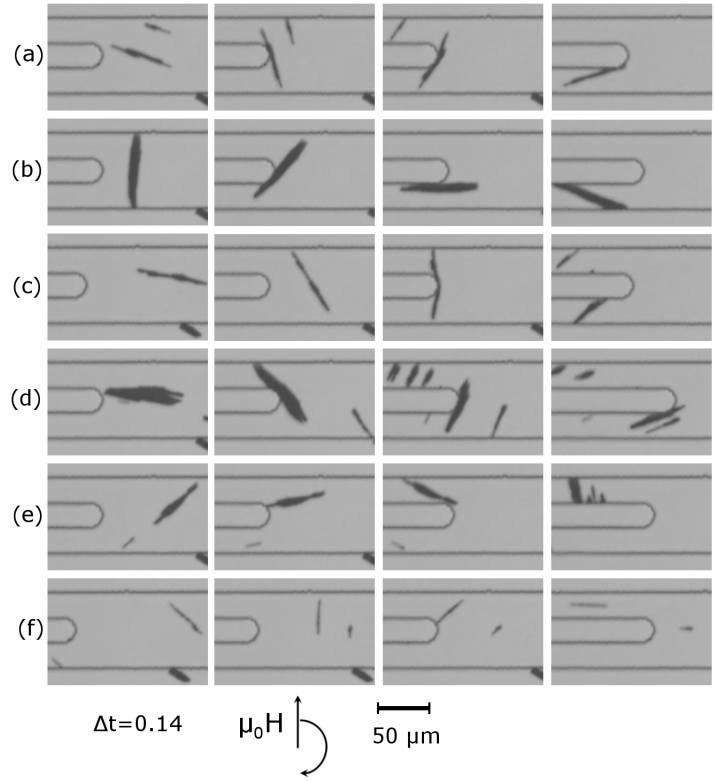

Figure 5.5: SPS behaviour in the separation region. Even at flow velocities of 274 µm s^{-1}, chains (a) and clusters (b) can be guided into the lower channel by clockwise rotation of the magnetic field. At these flow velocities, however, chains (c) and clusters (d) may fracture at the separation barrier due to shear induced stresses. Additionally, at high velocities of a few hundred micrometers per second, some superstructures pass the separation junction without interacting with the barrier (e). At all flow velocities, occasional fragments (f) with lateral dimensions smaller than the channel diameter pass the junction without being guided. The figure was taken from Eickenberg *et al.* [118].

reservoir that causes them to break and split into fragments[1]. As this effect is independent of the flow velocity, the slight decrease of the device efficiency is equal for all flow velocities. This contrasts with the effects of fracturing of SPS and incomplete rotation, as both these effects increase with the flow velocity.

The evaluation of the separation efficiency was performed for clockwise rotation only, as the system is fully symmetric along the main channel axis. The fraction of chains and clusters and the overall number of beads guided into the lower channel B were evaluated. For this, the device efficiency ε was defined as

$$\varepsilon = \frac{x - 0.5}{0.5} \tag{5.1}$$

with x as the fraction of beads that pass through channel B. Thus, possible values for ε range from 0 (statistical distribution of beads among both channels, no guiding effect) to 1 (every bead is guided into channel B).

The results for the channel with a width of 79 µm can be seen in Figure 5.6. At low flow velocities of 40 µm s^{-1}, the efficiency is very high (0.92) and 96 % of all beads are successfully guided into channel B. The ratio of guided clusters and chains lies at 97 % and 95 %, respectively, meaning that nearly every chain and cluster is guided into the correct channel. Only fragments are nearly equally distributed over both channels (56 % in channel B). The reason for this is the lateral dimension of the fragments, which is smaller than half the channel width, meaning that these SPS do hardly interact with the separation barrier. Thus, no guiding can occur.

With increasing flow velocity, the guiding effect decreases, thus ε and the ratios of guided SPS decline. At high flow velocities ($u = 270$ µm s^{-1}), the fracturing of SPS leads to a low efficiency of 0.26. Here, the guiding effect only leads to a slight favouring of channel B.

It is noticeable that the stability of clusters is significantly higher than that of chains. At a flow velocity of 120 µm s^{-1}, the cluster guiding ratio

1 Adjustment of the parameters for the chain formation inside the reservoir might further reduce the amount of fragments.

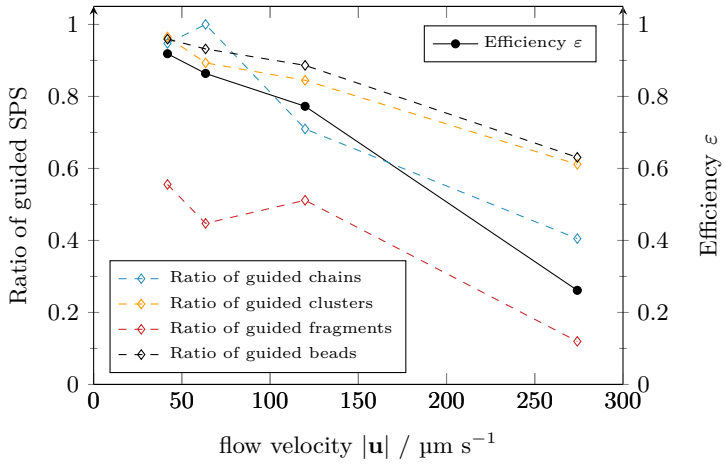

Figure 5.6: Efficiency of the guiding effect in dependence of flow velocity. The solid black line shows the dependency of the efficiency ε on the flow velocity. A definite trend for decreasing efficiency with increasing flow velocity can be seen. The dashed lines give the overall ratio of beads (*beads*) and SPS (*chains, clusters, fragments*) that were successfully guided into channel B. In these experiments, the magnetic field of 690 Oe was rotated at a fixed rotation frequency of 50 rpm. The used structure had a main channel width of 79 µm.

is still at 84 %, while the chain guiding ratio is decreased to 70 %. The additional stability of clusters can be attributed to the increased transversal width of these structures. More bead-bead connections result in a higher resistance to shear forces that try to pull the cluster apart. For an optimal device efficiency, therefore, a high ratio of clusters among SPS is desirable. This can be achieved by an increase in the rotation frequency (see section 2.2.2 and further results within the present section).

At a flow velocity of 270 µm s^{-1}, both the chain and the fragment guiding ratios show a value below 50 %, the minimum that would have been expected in the absence of any guiding effect. While the low chain guiding ratio can be explained by statistical uncertainty as the overall number of chains for this flow velocity was low, this does not explain the value of 12 % for the fragments. On first sight, the guiding effect seems to decrease the ratio

of these SPS in channel B. However, this is not true as there is another effect at work here: Due to their rotation in combination with friction at the walls, SPS move inside the inlet reservoir. This movement results in a higher SPS concentration in the upper half of the device. While chains and clusters rearrange inside the channel and move towards the channel center due to contact with the walls, fragments cannot reposition in such a way. Therefore, a higher number of fragments flows in the upper half of the channel. Thus, fragments are not distributed 50:50 over channel A and B. Taking this into account, the values of around 50 % at flow velocities below 120 µm s^{-1} can only be explained if a certain portion of the fragments are actually successfully guided. Otherwise, the ratio would be significantly below 50 % here, as well. Only at high flow velocities, the guiding becomes ineffective and the deficiency shows up in the statistics.

In further experiments, the dependency of ε on the rotation frequency was tested. To counteract the reduction in SPS length that comes with increased rotation frequencies, the main channel width was reduced to 67 µm.

Independent from the rotation frequency, a general trend for a decrease in ε with increasing flow velocity can be seen in the results (see Figure 5.7). The negative efficiency value at 250 rpm and a flow velocity of 445 µm s^{-1} can be explained through the previously mentioned bias in the fragment distribution. However, as can be seen from the low deviation of ε from zero, this effect hardly influences the device efficiency. A more controlled chain formation process and a different injection system for the beads would eliminate this effect.

The rotation frequency f strongly affects the device efficiency, as becomes visible in Figure 5.8. ε shows a maximum in the frequency range between 100 rpm and 200 rpm, independent from the flow velocity. Above 200 rpm, the device efficiency declines again. The trend can be explained through several counteracting influences that increase [+] or decrease [-] ε with increasing rotation frequency:

- [+] **Clusters stop bypassing the separation barrier.** At lower frequencies, SPS may pass the separation barrier without completing a 180° rotation. This gives a finite probability that no contact with the

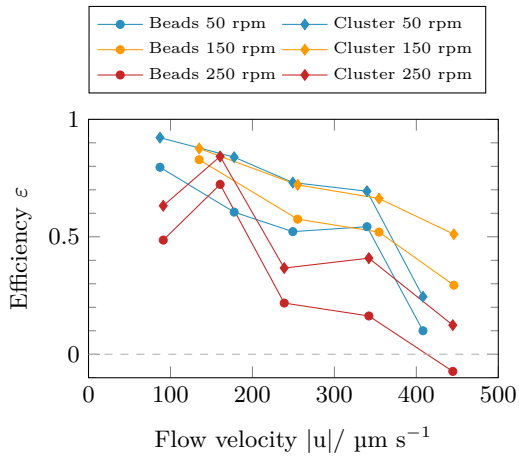

Figure 5.7: Guiding efficiency ε *vs.* flow velocity for different rotation frequencies at 330 Oe. The graph shows two separate sets of curves for the total amount of beads and the amount of beads in cluster structures. As can be seen, the cluster guiding efficiency is superior to the overall guiding efficiency, as chains and fragments are not guided as reliably as clusters. An overall trend for a lower efficiency with increasing flow velocity is visible. The main channel width of the structure was 67 µm. The figure was taken from Eickenberg *et al.*[117].

wall is made before the SPS pass the separation region, thus no guiding effect can occur (see Figure 5.5 (f)). The probability of this event increases with the flow velocity, as the residence time of SPS in the separation region is decreased. Higher rotation frequencies counteract this event. This is supported by the fact that the highest gain in ε is achieved when going from 50 rpm to 100 rpm at a flow velocity of 400-500 µm s^{-1}, the maximum flow velocity for the experiments. This clearly shows that at high flow velocities, where SPS have a high chance of bypassing the separation barrier without interaction, the rotation frequency is a critical parameter for successful guiding.

- [+] **Chains become clusters.** The ratio of clusters among the overall number of SPS changes with the rotation frequency f. At low

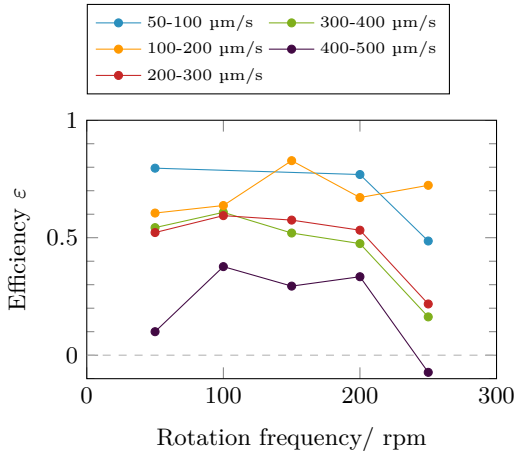

Figure 5.8: The efficiency ε plotted against the rotation frequency of the external magnetic field for different flow velocity intervals. The data suggests an optimum efficiency in the interval between 100 rpm and 200 rpm. At a magnetic field strength of 330 Oe, the main channel width of the structure was chosen to be 67 µm. The figure was taken from Eickenberg *et al.*[117].

rotation frequencies, a certain percentage of chains is present among the SPS (16 % at 50 rpm, see Figure 5.9). This value declines with higher f (to 3 % at 250 rpm), as chains become unstable, collapse and form clusters. As clusters are more stable than chains, there is a higher probability of successful guiding, thus ε is increased.

- [-] **Clusters become fragments.** The length of cluster structures depends on the rotation frequency, as Petousis *et al.*[42] showed. At higher frequencies, the length is - on average - smaller than at low frequencies (see section 2.2.2). At some point, the length of clusters is decreased below half the channel width, at which point they behave as fragments and an interaction with the separation barrier becomes less likely. Figure 5.9 illustrates this effect. The ratio of clusters among the SPS increases up to 69 % at 200 rpm. A further increase in the rotation frequency to 250 rpm decreases the cluster ratio to 63 % as the loss in SPS length moves a part of the cluster structures into the

fragment category. Smaller channel diameters counteract this effect.

- [-] **Increased angular momentum.** With increasing rotation frequency, the angular velocity and with it the angular momentum of the rotating chains are increased. This also means an increase in the linear momentum with which the SPS collide with the barrier. As linear and angular momentum are proportional to the rotation frequency, an increase in the frequency significantly increases the momentum. A higher momentum leads to a higher probability of SPS fracturing, thus lowering ε.

- [-] **Weaker magnetic forces.** At higher rotation frequencies the phase lag between the direction of the magnetic field (and the magnetization of the beads that follows the magnetic field) and the SPS axis increases (see section 2.2.2). With a higher deviation between axis and magnetization vectors, the dipolar coupling forces between the beads are weakened, resulting in a decrease in stability and therefore device efficiency. See text below for an estimation of the strength of this effect.

The *weaker magnetic forces* and *increased angular momentum* effects can be clearly seen in Figure 5.9. When increasing the rotation frequency from 50 rpm to 250 rpm, the ratio of broken clusters is raised by 180-220 % for flow velocities of 200-500 µm s^{-1}.

Taken together, these five effects lead to a maximum in the efficiency between 100 rpm and 200 rpm. The increase in ε at 250 rpm for the 100-200 µm s^{-1} curve is most likely a statistical anomaly.

The influence of the lag between the direction of the magnetic field and the magnetization of the beads can be estimated through the following calculations.

According to Petousis *et al.*[42], the forces acting between superparamagnetic beads aligned in a chain can be written as

$$F^r = \frac{3\mu_0 m^2}{4\pi r^4}(3\cos^2\alpha - 1) \tag{5.2}$$

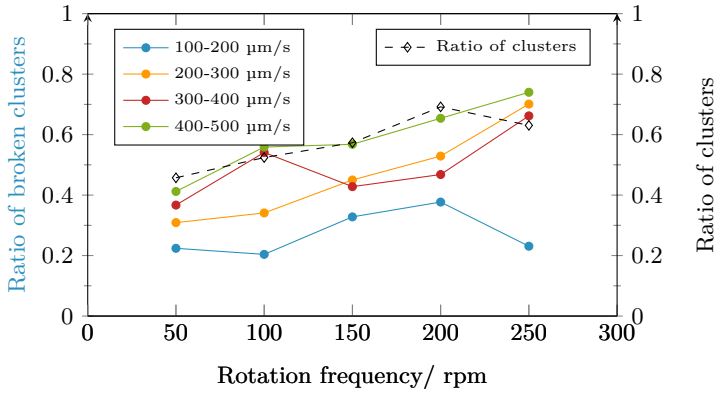

Figure 5.9: Cluster stability and ratio. The solid, coloured lines give the ratio of clusters that break when interacting with the separation barrier for different flow velocities. The probability for cluster fracturing increases significantly with the rotation frequency due to the increased momentum with which the clusters collide with the barrier and the weakening magnetic forces at a higher phase lag. The dashed line gives the ratio of clusters in the overall number of SPS, averaged over all flow velocities. The ratio increases until 200 rpm, where the loss in SPS length moves a part of the cluster structures into the fragment category. The data was collected at a field strength of 330 Oe. The main channel width of the structure was 67 µm. The figure was taken from Eickenberg *et al.*[117].

and

$$F^t = \frac{3\mu_0 m^2}{4\pi r^4} \sin(2\alpha) \tag{5.3}$$

if the particles are approximated as dipoles. Here, F_r and F_t are the radial and the tangential force component, μ_0 the vacuum permeability, m the magnetic moment of the particle, r its radius and α the angle between the axis of the chain and the magnetic moment of the particles (phase lag), respectively. The force component that holds the chain together is the radial force F_r, that becomes 0 at approximately 54.7°.

Under steady state conditions, the phase lag α converges to

$$\sin(2\alpha) \rightarrow \frac{\omega}{G} \tag{5.4}$$

with ω as the rotation frequency and $G = \frac{\mu_0 \chi^2 H^2}{16\eta} \frac{(N-1)\ln(N/2)}{N^3}$ as a constant that only depends on the nature of the beads, the solvent and the field strength H. Here, χ is the magnetic susceptibility, η the fluid's viscosity, and N the number of beads in a chain. As the phase lag becomes unstable at a value of about 45° and will then increase in time until it reaches the critical value of 54.7° that leads to a fragmentation, chains break at rotation frequencies below those required to obtain $\alpha = 54.7°$.

When equation 5.4 is solved for α and combined with equation 5.2, it yields

$$F_r = A(3\cos^2(\arcsin(\frac{\omega}{G})) - 1) \tag{5.5}$$

with $A = \frac{3\mu_0 m^2}{4\pi r^4}$. A plot of F_r/A can be found in Figure 5.10. As can be seen from the plot, the force is stable and independent of the rotation frequency over a very wide interval. Thus, the influence of the rotation frequency only becomes significant near the fragmentation point of the chain, where F_r becomes 0.

Note, however, that this calculation was based on the assumption of beads in a one-dimensional chain. The behaviour of two-dimensional clusters will be different, but is hard to predict, as the details about the magnetic configuration within the clusters are not know. For this reason, detailed calculations of F_r are not given here. However, the general trend concerning the trend of the dependency of F_r on ω should be the same.

In further experiments, the influence of the magnetic field strength was evaluated. Figure 5.11 shows a comparison of the efficiencies between devices under different magnetic field strengths, rotation frequencies and channel widths. As can be seen from the graph, a high magnetic field strength significantly increases the device efficiency. At a flow velocity of around 250 µm s^{-1} and a rotation frequency of 100 rpm, an increase of the magnetic field strength from 330 to 690 Oe increases ε from 0.59 to

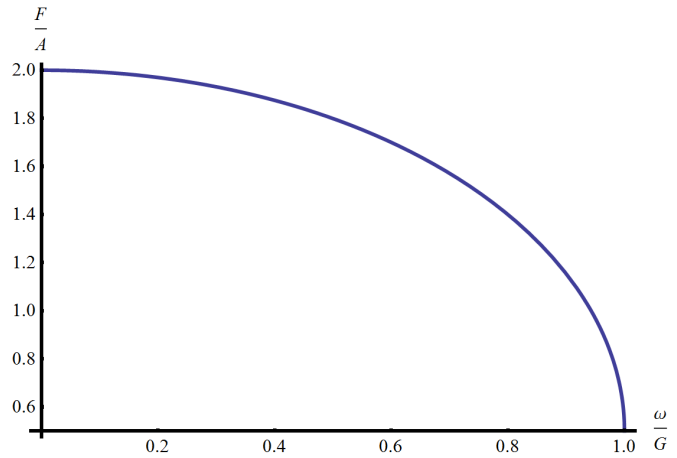

Figure 5.10: Plot of the normalized radial force F^r/A that retains the chain stability depending on the ratio of *omega*/G.

0.88. The reason for this influence lies in the superparamagnetic behaviour of the beads. As the magnetic field strength increases, the magnetization of the beads is raised. This, in turn, results in increased dipole forces between the particles of an SPS. Thus, SPS become more stable under the influence of strong magnetic fields until the magnetization of the beads nears its saturation magnetization, which is 23.5 M m^2 kg^{-1} for the MyOne beads[73].

As previously discussed, guiding becomes impossible if the lateral dimension of the SPS falls below half the channel width. Therefore, narrow channels should allow for increased separation efficiencies. The experimental results confirm this assumption. At a velocity of around 130 µm s^{-1} and a magnetic field strength of 690 Oe, the efficiency depends strongly on the main channel width. For a width of 79 µm, an ε of 0.77 was found, whereas a channel width of 69 µm resulted in an ε of 0.95. Additionally, in the range of flow velocities below 200 µm s^{-1}, the curve for the 79 µm channel at 690 Oe and the 67 µm channel at 330 Oe (both with an $f = 50$ rpm) are nearly identical. This means that the decreased channel width successfully counters the lower magnetic field strength.

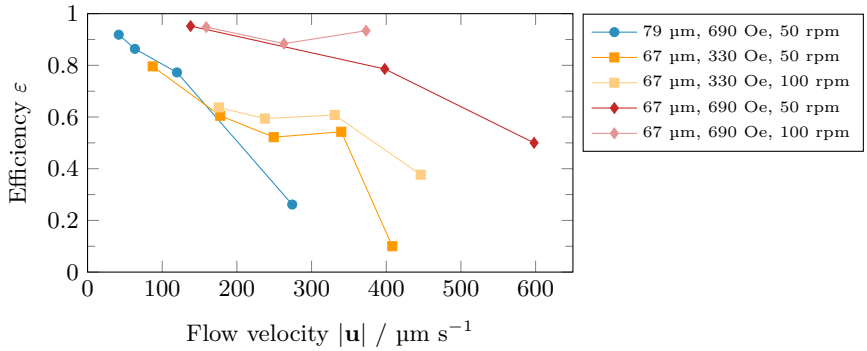

Figure 5.11: Effects of a higher magnetic field strength and a different channel geometry. At the same rotation frequency, a higher maximum field strength results in a significantly increased device efficiency. Additionally, narrower main channels lead to higher efficiencies. The figure was taken from Eickenberg *et al.*[117]. The data for the red curves (67 µm, 690 Oe) was obtained from measurements performed by Patrick Stohmann.

Even though the device efficiency is generally higher at low flow rates, for some applications the regime of medium to high flow rates might be more interesting. In these regions, the efficiency ε is lower, but the amount of guided beads per time may be higher due to the higher flow rate. To account for this, a mass separation rate ξ is defined as

$$\xi = \Gamma c_{\text{Bead}} \varepsilon \tag{5.6}$$

with c_{Bead} as the bead concentration and $\Gamma = |\mathbf{u}|a$ as the volume flow rate depending on the flow velocity $|\mathbf{u}|$ and the geometry parameter a of the channel. This geometry parameter depends on the area of the channel cross-section and includes the corrections for the parabolic profile of the flow. Figure 5.12 shows the results for this calculation for different magnetic field strengths, rotation frequencies and main channel widths. All curves show an increase in the mass separation rate with the flow velocity until the efficiency ε starts to be the limiting factor. At this point, ξ decreases with ε.

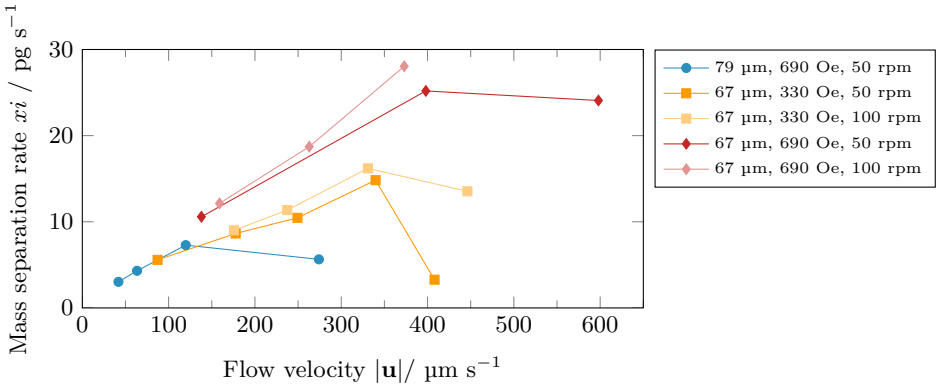

Figure 5.12: Mass separation rate depending on the flow velocity. Data is given for different magnetic field strengths, rotation frequencies and main channel widths. The graph shows that the optimum conditions are a small channel width, a high magnetic field strength and a flow velocity of about 300-400 µm s^{-1}. The figure was taken from Eickenberg *et al.* *The data for the red curves (67 µm, 690 Oe) was obtained from measurements performed by Patrick Stohmann.*[117].

5.3.2 Free-Flowing SPS for Particle Separation

The interaction of rotating SPS with a separation barrier can be used to separate colloidal particles, cells or macromolecules from a sample stream. For this, inlet I_1 is filled with functionalized beads that are able to bind the analyte from the analyte solution, which is inserted in inlet I_2. At the T-intersection, the bead SPS contact the sample stream and bind analyte molecules. As the mixing effect is of local character (see following section), the bead dispersion remains largely pure and the sample matrix is separated from the SPS at the separation barrier.

This mechanism of particle guiding was shown to work in a proof-of-principle experiment. In this experiment, biotin coated, non-magnetic particles were successfully captured by SPS consisting of MyOne beads with a streptavidin coating. The captured biotin particles were then guided into channel B together with the SPS, while unbound particles were flowing

into channel A (see Figure 5.13).

For future applications, the biotin particles could be exchanged for labelled cells. However, the binding efficiency needs to be enhanced. In the experiment described above, the biotin and MyOne particles were flowing at different heights in the channel, due to different densities and therefore differing buoyancy forces, making binding events rare.

In the case of cell separation, the density of cells and beads would have to be chosen or manipulated appropriately to allow for an optimal binding efficiency. One alternative option would be to use low-ceilinged channels so that beads and cells cannot pass each other in the z-direction. If electromagnetic coils were used to create an additional rotational component out-of-plane (in a plane orthogonal to the flow direction), the movement pattern of the SPS could be changed to a three-dimensional rotation, a sort of staggering movement. That way, the rotating SPS would cover a volume instead of an area, increasing the capturing efficiency.

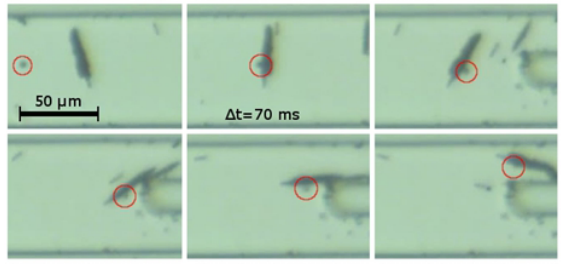

Figure 5.13: Utilization of the guiding effect for the separation of particles from a sample stream. At a flow velocity of about 650 µm s^{-1}, a biotin-coated polystyrene particle (red marking) is captured by a streptavidin-coated bead superstructure and guided into the upper channel. Field strength and rotation frequency were set to 330 Oe and 60 rpm, respectively. While flowing through the channel, the structure shows a rotation around its longitudinal axis, as can be seen from the movement of the attached particle. Note that the position of the polystyrene particle in the upper half of the channel results from previous mixing due to superstructure rotation.

5.3.3 Mixing Efficiency

The free flowing, rotating SPS disturb the boundary layer between the parallel flows of the bead dispersion and the FAD solution (see Figure 5.14 (a)). In the absence of SPS, the only driving force for mixing is thermal diffusion. In the presence of SPS, the shear forces of the rotating structures create a laminar flow around the SPS that leads to a convective flux of FAD solution into the bead dispersion region and *vice versa*.

In order to analyze the influence of the stirring SPS on the concentration distribution and the mixing efficiency, Frank Wittbracht [119,120] evaluated the intensity profiles of the FAD solution at a section 310 µm downstream from the T-intersection. He compared the data to the analytic solution of free diffusion across an interface:

$$p(x,t) = \frac{1}{2}\mathrm{erfc}\left(\frac{x}{\sqrt{4Dt}}\right) \tag{5.7}$$

with x as the distance from the channel wall, t as the time and D as the diffusion constant. By fitting the obtained concentration profile with the analytic solution (see Figure 5.14 (b)), two diffusion constants, D_0 for the undisturbed and D_{eff} for the stirred state, were calculated. For D_0, the diffusion coefficient in absence of stirring SPS, a value of $D_0 = 3.04 \cdot 10^{-10}$ m^2 s^{-1} was found, which is in good agreement with the finding of Radoszkowicz *et al.* [121] who found a D_0 of $D_0 = 3 \cdot 10^{-10}$ m^2 s^{-1} for the diffusion of FAD in water. In the presence of rotating SPS, Wittbracht found a $D_{\mathrm{eff}} = 4.02 \cdot 10^{-10}$ m^2 s^{-1}, corresponding to an increase in diffusivity of 32 %.

As the mixing effect of the SPS only occurs in the vicinity of the free flowing structures, the structure density strongly influences the degree of mixing between the parallel flows. Depending on the desired result, the device can be operated at high mixing efficiency (high SPS density, high bead concentration) or low mixing efficiency (low SPS density, low bead concentration). In the latter case, the mixing is restricted to the volume near the SPS structures.

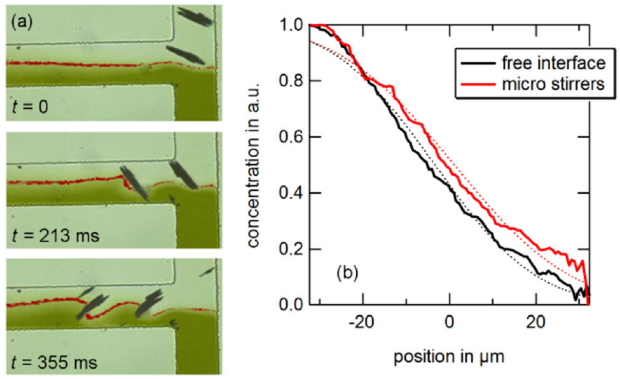

Figure 5.14: Clockwise rotating magnetic bead chains increase the mixing of FAD solution in water. (a) Distortion of the interface (highlighted in red) along the T-junction and (b) resulting concentration profile in comparison to a thermal reference. Data was evaluated by Frank Wittbracht. Data and figure were taken from Wittbracht *et al.*[120].

5.3.4 Comparison with Magnetophoresis

Separation of analytes (either cells or biomolecules) from a sample stream has already been achieved through the means of on-chip magnetophoresis[19,20]. For this, functionalized superparamagnetic beads are mixed with the sample either previous to injection or (rarely) on-chip. Inside the chip structure, the beads are then separated by applying a magnetic gradient field where the magnetic force acts orthogonal to the flow direction. This way, particles and the bound analytes can be guided from the sample stream into a buffer stream that is analyzed downstream. As the movement speed of the particles depends on the drag force (and therefore on the particle size) and the particle magnetization, particles can even be separated according to these two parameters. As this technique is well researched, the question might be asked what advantages the proposed SPS-based guiding mechanism possesses.

To answer this question, the following list names advantages [+] and disadvantages [-] of the SPS guiding mechanism compared to magnetophoresis.

- [+] **Higher filtering efficiency.** If magnetophoresis is carried out on-chip, the analyte molecules must come into contact with the bead surface. As diffusion is usually not efficient (as previously discussed), this usually requires a mixing stage prior to separation. This is usually done off-chip[20]. If it is performed on-chip, it requires additional mixing structures and increases the fabrication costs.
  In the SPS-based mechanism, the rotation of the SPS facilitates (local) mixing. The SPS sweep a wide arc around the SPS center, thus tapping a larger sample volume than a single particle could. Thus, the number of analytes that are collected without additional mixing steps is considered to be superior to magnetophoresis applications.

- [+] **Continuous-flow applications.** If beads and sample need to be mixed off-chip, which is often the case for magnetophoresis, the method does not compose a continuous-flow application. This is different for the SPS-based system.
  The advantage of a continuous-flow measurement is that sampling at locations where the microfluidic chips cannot easily be exchanged, e.g. in remote locations, becomes possible. It is also a necessity for applications where a constant supply of analytic data about a process, e.g. a chemical synthesis, is required.

- [+] **Less control over magnetic field required.** For magnetophoretic applications, the magnetic gradient needs to be fine-tuned. If the gradient is too high, beads get stuck to the wall instead of moving downstream in the buffer. If the gradient is too low, there is no separation effect. The SPS-based system, however, requires no fine-tuning, as can be seen from the experimental data. Although the field strength influences the device efficiency, a non-optimal field strength will still result in the separation of analyte molecules.

- [-] **Reduced reliability at higher flow rates.** In the current state, the separation efficiency of the SPS-based system at flow rates of a few hundred micrometers per second depends strongly on the shape and size of the SPS and varies with each experiment. This influences applications where quantitative measurements of the analyte

concentration are necessary. Here, magnetophoresis should be the preferred choice until this problem has been solved (see Outlook section).

- [-] **Higher bead consumption.** The SPS-based system requires more beads than magnetophoresis applications. As the surface of beads within a cluster is partially unavailable for binding, the surface per bead is decreased compared to single beads in dispersion. For the same amount of analyte, a higher number of beads has to be used.
- [-] **No separation of different bead species.** Unlike in magnetophoresis, the separation mechanism in the SPS-based system does not depend on the parameters of the beads (like size or magnetic moment). Thus, a separation of different bead species is not possible.

As can be seen from the list, the method possesses some significant advantages compared to magnetophoresis, but requires further development before it can really be used as an alternative separation procedure.

5.4 Conclusion

In the experiments described in this chapter, the rotational movement of SPS was successfully used to guide them into a specific channel by steric interaction with a separation barrier. At flow velocities of 40 µm s^{-1}, 96 % of all beads were guided, corresponding to an efficiency $\eta = 0.92$. At higher flow velocities, however, the efficiency decreased rapidly ($\eta = 0.26$ at a flow velocity of 270 µm s^{-1}), although changes in the channel dimensions or modifications of the magnetic field can be used to counteract this loss in efficiency (see below). In general, cluster structures can be guided with a higher efficiency than chain structures, owing to the higher structural stability of clusters. Fragments with a length smaller than half the channel width cannot be guided.

The guiding efficiency is furthermore influenced by the rotation frequency. Several counteracting effects were identified that increase or decrease the efficiency with increasing rotation frequency in the range of 50 rpm to

250 rpm. This results in an efficiency maximum between 100 rpm and 200 rpm.

Further parameters that influence the guiding efficiency are the magnetic field strength and the channel dimension. As higher magnetic field strengths increase the structural stability of the SPS, fragmentation events become less likely, thus yielding a higher efficiency. At a flow velocity of 250 µm s^{-1} and a rotation frequency of 100 rpm, the efficiency was increased from 0.59 to 0.88 by an increase in the magnetic field strength from 330 Oe to 690 Oe. The channel dimension is important as the SPS length must be higher than half the channel width to enable successful separation. The smaller the channel, the higher the chance that an SPS fulfills this criteria. Decreasing the channel width from 79 µm to 67 µm at a flow velocity of 130 µm s^{-1} therefore increased the efficiency from 0.77 to 0.95.

While the efficiency of the device decreases steadily with increasing flow velocity, the volume flow rate that defines how many beads are separated per time has a maximum in the region of medium flow velocities. The exact position of this maximum depends strongly on the remaining device parameters.

In a proof-of-principle experiment it was shown that the proposed separation mechanism is capable of separating biotinylized microparticles from their dispersion flow by catching and guiding them with streptavidin-covered, rotating SPS. This shows that the device would be capable of separating biomolecules from a sample prior to the detection step, thus preventing background signals from the sample matrix. The system could also be used to separate cells that are specifically targeted by functionalized beads. Cells that express a certain surface protein could be bound to the beads and separated from the cells that do not express this protein and therefore do not bind to the beads.

Calculations by Wittbracht further showed that the rotating SPS enhance the mixing of two co-flowing streams of water and an aqueous FAD solution by 32 % compared to diffusive mixing as they disturb the boundary layer by convection.

Compared to magnetophoretic separation, the proposed device offers substantial advantages. The increased mixing makes on-chip binding of analyte molecules faster and more efficient. This facilitates the use as a

continuous-flow method, which is often not possible with magnetophoretic applications that require off-chip mixing. As the device works with homogeneous magnetic fields instead of gradient fields, the device is less sensitive to deviations from the optimum field parameters. However, successfull applications of the device will require more fine control over the SPS formation process, as the shape and size of the SPS significantly influences the guiding effect (see following Outlook section).

5.5 Outlook

For future applications of the device, two main challenges need to be met:

1. The SPS stability needs to be increased to allow for higher flow velocities at decent separation efficiencies. Partly, this task has been completed with the development of DNA bridges between beads that add to the structural stability of SPS (see chapter 6). This method will have to be applied to the previously described guiding application to show that it works under continuous-flow conditions.

2. Currently, the SPS size varies strongly within one set of parameters. To optimize the device efficiency, a way to form defined bead 'packages' consisting of SPS of roughly the same size and shape needs to be developed.

As soon as these issues have been solved, the guiding effect needs to be applied to separate analyte molecules or cells from an actual sample like blood or saliva. For this, it would be helpful to increase the capture rate of the SPS. Apart from using low-ceilinged channels or optimizing the buoyancy of cells and beads, the capture rate could be increased by the addition of a rotational component orthogonal to the flow direction. The resulting three-dimensional movement of the SPS would cover a volume instead of an area, thus increasing the capture efficiency.

6 DNA Bridges as Bead-Bead Interconnections

For some applications like the guiding mechanism presented in chapter 5, the magnetic forces holding the SPS together are not sufficiently strong. For these applications, a way to enhance the SPS stability needs to be found. If possible, the method to enhance stability should be reversible, so that assembled structures can still be disassembled by changing the environmental conditions. Since most physical forces are weak compared to chemical bonds, but chemical bonds are hardly reversible, an intermediate state between the two extremes seems necessary. The hydrogen bond represents such an intermediate state, as it is a directed, very strong physical interaction that borders on a chemical bond, but can easily be broken by an increase in temperature. However, as the bond strength is significantly lower than for true covalent bonds, multiple hydrogen bonds are required. In addition, to maintain a specific melting temperature of the system, the number of hydrogen bonds between beads should be controllable with high precision. If the number can be varied arbitrarily between experiments, different melting temperatures of the bonds can be set.

These requirements - arbitrary numbers of hydrogen bonds that can be precisely controlled - are met by deoxyribonucleic acid (DNA) double strands. DNA is a polymeric chain made from a sequence of four different nucleotides that are composed of a nucleobase (guanine, adenine, thymine or cytosine[1] and a backbone consisting of deoxyribose sugar and phosphate. Hydrogen bonds can form between the guanine and cytosine and the thymine and adenine base pairs. Thus, DNA strands can combine (*hybridize*) to

1 The four nucleobases are often abbreviated as G,A,T and C, according to their first letter.

form DNA double strands, in which counter-directional single strands are held together by hydrogen bonds. The double strand can be melted by an increase in temperature. The melting temperature depends on the base sequence[1] and the nature of the base pairs[2, 3] [123]. Due to the rather stiff conformation of hybridized DNA, the double strands can also serve as spacers, defining the distance between particles by the length of the double strand.

Thanks to technological advances in the past decades, DNA strands of arbitrary sequences can be synthesized with high precision [124,125,126,127]. Furthermore, the ends of a DNA molecule can be functionalized with a variety of biomolecules or chemical functions, allowing to graft the DNA to other molecules, surfaces or - in this case - beads. This can be used to generate beads covered with a layer of DNA single strands that are complimentary to a linker strand in solution that interconnects beads, thus increasing the binding strength between beads of an SPS (see Figure 6.1).

Further Applications for Interconnected Beads

Although the motivation to produce interconnected bead SPS in this work has been simply to enhance the structural stability of the SPS, possible other applications for this method exist. A number of papers have been published on the arrangement of microparticles made from polymers, silica, metals or semiconductor materials into highly ordered, crystalline patterns in two [128,129,130,131] or three [129,132,133,134] dimensions. These arrays can be used as templates for the synthesis of nanostructured materials [135] or find application as (colloidal) photonic crystals [128,136]. Although there are plenty of methods for a top-down fabrication of photonic crystals [137,138,139,140,141]

1 As each base can only bind with its counterpart (the complimentary base), mismatches in the sequence do not increase the binding strength of the double strand.

2 Thymine and adenine form two hydrogen bonds while cytosine and guanine form three bonds. Thus, a higher GC content increases the overall number of hydrogen bonds and therefore the melting temperature.

3 To be more exact, environmental parameters like the salt concentration also influence the DNA melting temperature. More details on the dependency of the melting point of DNA-coated (nano)particles can be found in a paper by Jin *et al.* [122]

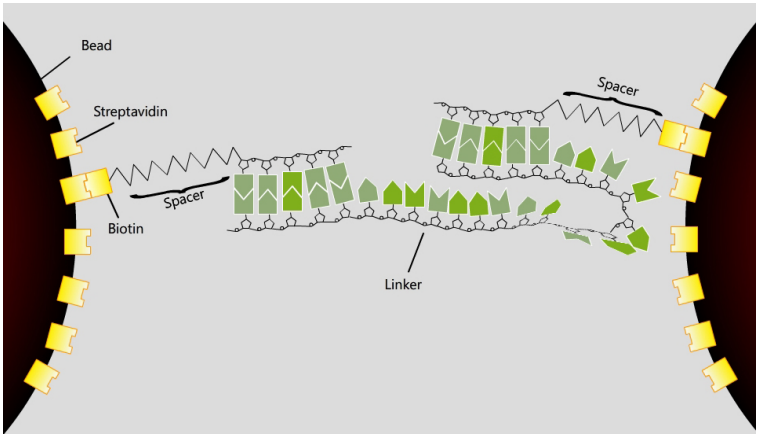

Figure 6.1: DNA-based interconnections between beads. DNA single strands of specific sequences can be synthesized and attached to a streptavidin-covered bead by biotinylized ends. If the sequence is complimentary to a linker strand present in the solution, the linker will attach to the strands immobilized on the beads, thus linking adjacent beads through a series of hydrogen bonds that have a very defined melting temperature. To ensure that the complimentary regions are far enough from the bead surface, spacer sequences that do not contribute to the binding are introduced into the surface-bound strands.

the required clean-room facilities and lithographic instrumentation make these methods complex and expensive. A bottom-up fabrication is therefore a preferable choice for bulk production. Typically, bottom-up methods include micro- or nanoparticles that are arranged into a crystalline structure by either non-specific binding between particles (e.g. van der Waals and electrostatic forces) or through specific binding between (bio-)molecules on the surface of the particles (e.g. avidin-biotin, antigen-antibody). Compared to non-specific binding, specific binding offers the advantage of a higher control over the shape of the arrangement [142]. However, specific binding is usually irreversible and therefore predominately kinetically controlled. The particles do not align in their thermodynamically most stable arrangement, but bind together in whatever sterical orientation they come into contact. This results in amorphous aggregates instead of ordered crystalline arrange-

ments. Several groups have reported a way to circumvent this problem through the use of DNA bridges between the particles[143,144,145,146,147]. The basic method is the same as the one described in the previous section. The main difference is that throughout the process the temperature is held just below the melting temperature of the DNA, thus allowing the beads to find a thermodynamically stable structure, usually a dense packing of spheres. The downside of this method is that this annealing takes one to several days and rarely results in highly ordered mono- or multilayers that contain more than a few dozen particles. To the knowledge of the author, Geerts *et al.*[148] were the only group that acquired ordered agglomerates spanning more than hundred microspheres in diameter. However, they did so by binding microspheres to a solid substrate through long DNA strands and not by direct binding between the spheres.

DNA-Bridged Monolayers Assembled from SPS

The experimental time needed to form dense, crystalline agglomerates of microparticles can be significantly reduced if magnetic fields are used for the assembly process. Cluster-like SPS of magnetic beads can be formed under the influence of rotating magnetic fields. If the bead density is sufficiently high, these clusters quickly assemble into highly ordered, two-dimensional monolayers[43]. These pre-arranged monolayers can then be passivated by DNA-bridges: Oligonucleotides bound to the bead surface bind to a linker strand in solution (see Figure 6.1). This method might pose a solution to the problems encountered in the formation of (2D) photonic crystals mentioned in the previous section.

In this experiment, biotinylated DNA was bound to Dynabeads M-280 with a streptavidin surface. Under the influence of a rotating field, bead monolayers were formed. It was then tested whether the monolayers could be passivated by the addition of a linker strand that is complementary to the surface-bound single strands. The process was furthermore tested for thermo-reversibility. The experimental work presented in this chapter has been performed by Marianne Bartke in her master's thesis and constitutes a work in progress.

6.1 Materials and Methods

DNA sequences (see Figure 6.2) were synthesized by eurofins. The chosen sequence was previously used by Biancaniello *et al.*[147]. It has a low amount of secondary structure and minimal sequence repetition with melting temperatures for all nondesigned conformations below 25 °C. The melting temperature for the binding to a complementary sequence is 47 °C. To test the binding between DNA and beads, a thymine base in the sequence (see red base in Figure 6.2) was marked with a fluoresceine molecule.

The phosphate buffered saline (PBS) used in these experiments consisted of 1.06 mM KH_2PO_4, 2.95 mM Na_2HPO_4 and 155 mM NaCl and was set to a pH of 7.4.

The magnetic field was supplied by the IKA RCT basic magnetic stirrer with the stronger magnet described in section 3.4. At the position where the experiments were conducted, a maximum field strength of 620 Oe was measured.

surface bound:
TCTCTAAAGTTCAATCTGCACACACACTTAGTTA-
-CCCGGAGCCTCTGACTATTACGACATCAATTCA-
Biotin
linker:
TTGAACTTTAGAGACTTGAACTTTAGAGA

Figure 6.2: DNA sequences of the strands connected to the bead surface (*surface bound*) and the linker strand that is used to connect two surface bound strands (*linker*). The complementary regions are marked in blue. The red base represents the thymine that was marked with fluoresceine for the binding test. The sequences are given in 5'-3' direction.

6.2 Experiments

The experimental section is divided into three separate experiments. In the first experiment, the binding between beads and DNA was tested *via*

absorption spectroscopy. In the second part, monolayers of M-280 SA beads were formed and hardened by the addition of a DNA linker strand. In the last experiment, the binding strength of the DNA bridges was tested with atomic force microscopy (AFM). Experimental descriptions are limited to the necessary information. For more details on the procedure please refer to Bartke's work[149].

6.2.1 Binding DNA to the Bead Surface

2 µL of the Dynabeads M-280 SA stock solution (10 mg mL^{-1}) were mixed with 3 µL of the coating-DNA solution (166 µM) and 95 µL of PBS buffer. Afterwards, the mixture was swirled for 24 hours. The beads were then separated with a permanent magnet that was held to the bottom of the Eppendorf vial to collect the beads. The supernatant was extracted and analyzed by UV-Vis spectroscopy to evaluate the binding efficiency. The spectroscopy measurements were performed by Lena Böhling from the PC1 group of Bielefeld University. A Shimadzu UV2501PC spectrometer was used, probing the wavelength interval between 200 nm and 700 nm in steps of 0.5 nm.

The obtained beads were washed twice with 20 µL of PBS buffer. Finally, the beads were suspended in another 20 µL of PBS buffer with 0.1 w-% Tween-20 surfactant to reduce non-specific interactions between the beads.

To test whether the binding between the streptavidin and the biotin would break when heated to the melting temperature of the DNA, thus releasing the DNA strands from the bead surface, samples of DNA-covered beads where heated to 70 °C for 5, 15, 30, 60 and 240 minutes. After this time, the beads were separated with a magnet. The supernatant was removed and analysed by UV-Vis spectroscopy, as described above.

6.2.2 Monolayer Formation

The experiment was performed inside a PDMS well that was prepared by cutting a hole of approximately 5 mm into a PDMS layer of $1.5 - 2.0$ mm thickness. The PDMS was then attached to a glass object plate and placed on an IKA RCT basic magnetic stirrer. A field rotating at 450 rpm (field

strength: 620 Oe) was applied. A droplet of 1.5 µL of the previously prepared DNA-bead solution (containing about 72000 beads) was deposited in the well. After 120 seconds each, during which cluster structures were formed, two more droplets were added to facilitate the growth of a dense monolayer. After the formation was complete, 3 µL of the DNA linker solution (166 µM) were added to the monolayer. Afterwards, the droplet was heated to 55 °C, above the melting temperature of the DNA, using the heating function of the magnetic stirrer. This was done to allow for defect repair within the monolayer due to bead rearrangements [43]. After five minutes, the droplet was allowed to cool down to room-temperature within a time period of 1 hour. Droplet evaporation during heating and cooling phases was prevented by a PDMS lit that was put over the PDMS well. The rotating magnetic field was sustained for the complete duration of the experiment. Note that during the cooling period no further cluster formation took place. By active cooling of the sample, the duration of this experiment could be shortened, on the premise that the linker DNA is given enough time to connect to the surface-bound DNA strands (which was estimated to be on the order of several minutes).

Images of the monolayers were taken with the microscope setup presented in section 3.3. Scanning electron microscopy (SEM) images were taken by Nadine Mill with a Leo 1530 (Zeiss).

To test whether the binding is thermo-reversible, the rigified monolayer was heated to 70 °C to melt the DNA bonds while the magnetic field was switched off. During the subsequent cooling phase, the monolayers were rebuild using the previously described rotating magnetic field. To ensure a decent reformation of the monolayer, a small addition of beads (1.5 µL) and linker DNA (1.0 µL) was necessary.

6.2.3 Evaluation of the DNA Binding Strength

To test the binding strength of the DNA bridges, a small part of the outer region of a monolayer was scanned with the cantilever tip of an AFM (MFP-3D-BIO Inverted Optical AFM, Asylum Research) in contact mode. This was done in the dried state, as the liquid state allowed for evasive movements of the monolayers when the cantilever applied a force on the

surface.

By pressing down on the region between two adjacent beads, it was tried to break the bonds and separate the two beads. The maximum force that could be applied this way was found to be 350 nN, at which the cantilever tip broke off. The AFM experiments were performed by Tamara Münnich.

6.3 Results and Discussion

In the following section, the results of the previously described experiments are presented and discussed. For a more detailed report on the findings please refer to the master's thesis of Marianne Bartke [149].

6.3.1 Binding DNA to the Bead Surface

The UV-Vis spectroscopy analysis of the supernatant revealed that the DNA quickly adsorbed on the bead surface. As can be seen from the values presented in Table 6.1, the binding is already nearly complete after 1 hour, where about 58 % of the DNA are immobilized on the surface. This is equivalent to $1.47 \cdot 10^8$ DNA strands per bead.

Table 6.1: Results of the UV-Vis spectrometry analysis of the binding efficiency between the streptavidin beads and the biotinylated DNA. The column *time* gives the time between the mixing of DNA and beads and the extraction of the supernatant. A_{495} denotes the absorption at a wavelength of 495 nm. c represents the concentration of DNA in the supernatant while X stands for the percentage of DNA strands that were successfully deposited on the bead surface. The data was averaged over two samples for each time step.

Time/h	A_{495}	c/µmol L^{-1}	X/%
1	0.0058	0.176	58
6	0.0058	0.176	58
24	0.0054	0.163	61

The analysis of the supernatant samples that were taken subsequent to the heating periods showed that in no case more than 10 % of the DNA went into solution. There was no correlation between the heating period and the amount of detached DNA. A possible explanation might be that some DNA molecules adsorbed unspecifically on the surface of the beads without forming a streptavidin-biotin bond. However, the experiment shows that the bond is stable at elevated temperatures, meaning that only the bond between the surface-bound DNA strand and the linker strand can break during the heating periods, thus making a reversible thermal disassembly of the stabilized monolayers possible.

6.3.2 Monolayer Formation

Under the influence of the rotating magnetic field (see Figure 6.3 for a schematic of the experimental steps), the beads quickly form dense clusters that agglomerate into large monolayers of sizes in the millimeter range. Figure 6.4 shows optical microscopy images of the formation process. During the agglomeration, beads at the outer surface of the clusters are still rearranging. While the core of a cluster remains stable, beads at the surface constantly separate and reattach and move around the cluster surface. This behavior of the beads results in a self-repair mechanism of defects. Whenever two clusters agglomerate, the reordering slowly removes defects

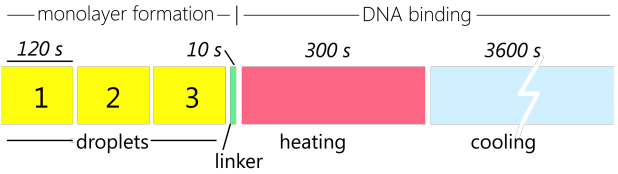

Figure 6.3: Overview over the length of the different experimental steps involved in the formation of interconnected bead monolayers. Different from common annealing procedures that take dozens of hours, the magnetic field assisted process forms monolayers within several minutes. The heating and cooling periods represent the most time-consuming steps and could be minimized, should shorter time scales be required.

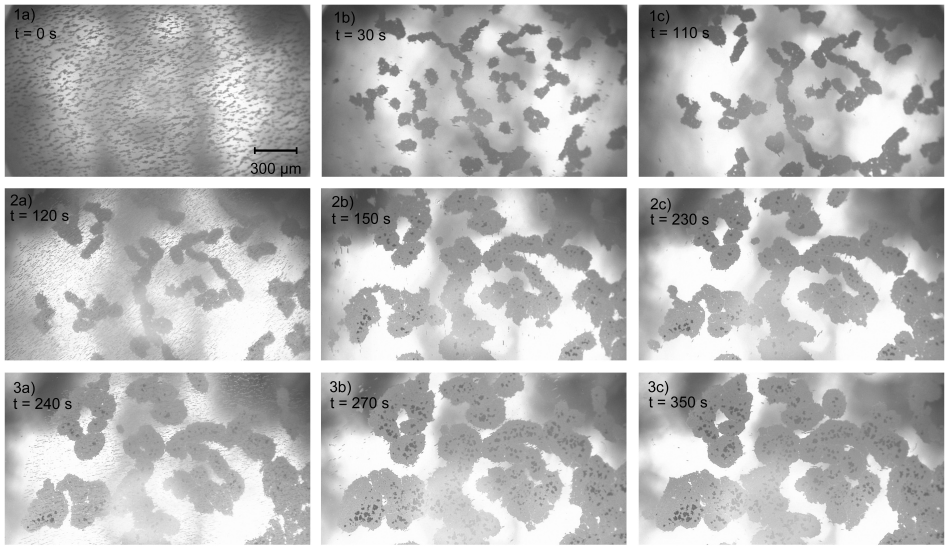

Figure 6.4: Monolayer formation. Under the influence of a rotating magnetic field, superparamagnetic particles form into cluster structures within tens of seconds (1). After 120 s each, more droplets of the particle suspension are added (2 and 3). The additional beads quickly attach to the existing clusters, thus forming a highly ordered monolayer after the addition of several droplets.

such as vacancies or line defects (which result from different orientations of the two clusters). This behaviour and the dependency of the monolayer quality on different experimental parameters has been reported in previous work[43] and was not further evaluated in this experiment.

The hybridization between the DNA single strands on the surface of the beads and the linker strands leads to a solidification of the monolayer. In absence of the linker DNA the removal of the magnetic field results in the decay of the monolayer as the stray field of the beads collapses and they begin to diffuse apart (see Figure 6.5, right). In the presence of linker DNA, however, the layer remains perfectly stable (see Figure 6.5, left).

Heating the solution to a temperature above 70 °C melted the DNA bridges and disassembled the monolayer. During the cooling phase, it was possible to rebuild the monolayer by a reactivation of the magnetic field,

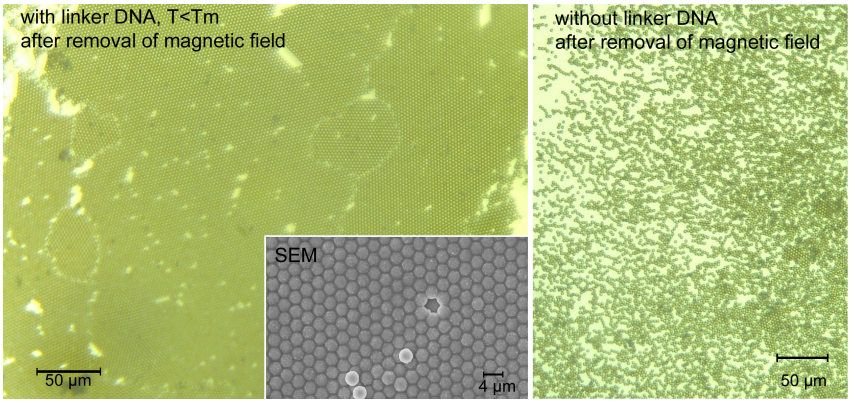

Figure 6.5: Images of monolayers with (left) and without (right) stabilizing DNA bridges in the absence of a magnetic field. While the monolayer remains stable when beads are connected by DNA strands, it decays rapidly (within tens of seconds) if beads can diffuse apart without being bound by the DNA. The inlay shows a scanning electron microscopy (SEM) image of the highly ordered monolayer with a few beads in a second layer.

but with significantly more defects (see Figure 6.6). The process resulted in an increased amount of beads in a second layer and decreased cluster size, whether additional beads and linker were added or not. However, monolayers could be successfully reassembled two times in a row.

6.3.3 Evaluation of the DNA Binding Strength

The AFM experiments showed a high stability of the bead-bead DNA connection. A force of 350 nN, the maximum force that could be applied before breaking the cantilever tip, was not able to separate the beads. Figure 6.7 shows an AFM image of the cluster structure that was used in these experiments. Although exact measurements of the binding strength could not be performed, yet, this result shows that the monolayer stability is significantly increased by the presence of the DNA bridges.

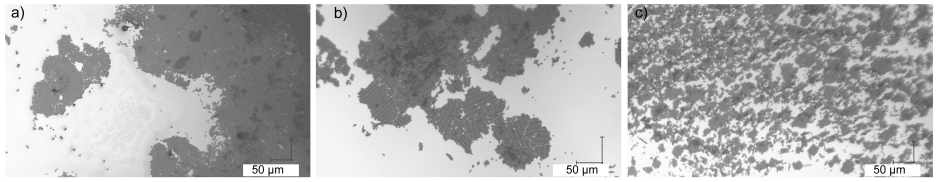

Figure 6.6: Reversible reformation of the monolayers. Bead clusters assembled via rotating magnetic fields and fixed with DNA bridges (a) can be disassembled by elevating the temperature. Afterwards, the assembly can be restored by lowering the temperature while the magnetic field is active. However, even though additional beads and linker DNA were added, the clusters became smaller with every reassembly step. (b) and (c) show cluster structures after the first and second reassembling step, respectively. In all pictures, the magnetic field is inactive, so that the beads are only held in place by DNA bridges.

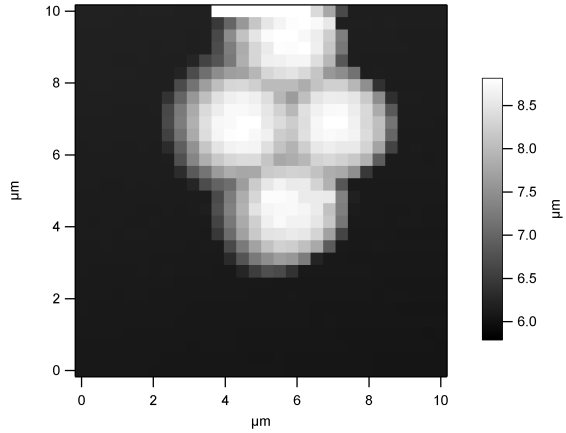

Figure 6.7: AFM images of beads connected by DNA bridges. The images were taken in contact mode with a force of 300 nN.

6.4 Conclusion

Monolayers of beads that were functionalized with single-stranded DNA were successfully solidified by the addition of a linker strand. The DNA bridges that formed when linker and surface-bound DNA strands hybridized were able to stabilize the monolayers when the magnetic field was removed. AFM measurements showed a high stability of the linked bead agglomerates. A force of 350 nN applied with an AFM cantilever tip was not able to push linked beads apart. Furthermore, the solidification was shown to be reversible. Heating the sample to a temperature above the melting temperature of the DNA double strands disassembled the monolayers. Reapplying a rotating magnetic field lead to the reformation of the clusters, although the overall cluster size and quality was reduced with each reformation.

The process presented in this work significantly reduces the time in which highly ordered monolayers of beads interconnected with DNA can be arranged from one to several days down to less than an hour. With this method it is possible to stabilize SPS structures within microfluidic channels or form mechanically stable, self-assembling monolayers. Furthermore, the production of such arrangements might be used for the production of 2D photonic crystals.

6.5 Outlook

The presented method yields 2D systems of beads, only. 3D agglomerates cannot be formed at the moment. If 3D structuring is required, modifications of this method have to be developed in which one layer of beads is built upon an existing one, one step at a time. This will be the aim of future work.

Furthermore, additional AFM measurements to obtain quantitative data about the binding strength between the beads are required. This could be done by binding one bead to the surface while attaching the other one to the cantilever tip. When the cantilever is pulled away, the force that is required to break the bead-bead-bond can be measured.

The process of interconnecting beads with DNA bridges might be used to

form agglomerates of specific shapes, provided that appropriate combinations of DNA strands are used. It might be possible to utilize the method for the formation of 2D or 3D smaller agglomerates of reduced symmetry, such as tetrahedrons or octahedrons.

Lastly, the self-assembling monolayers need to find application within microfluidic systems. Future experiments will show whether clusters assembled within a microfluidic channel can be used to block the channel for particle flow, thus creating a particle valve. Alternatively, multiple clusters that are turned orthogonal to the flow direction by a magnetic field can be stacked and used as a filtration net or a microfluidic chromatography column with a very narrow pore size[1].

1 The narrow pore size does not result from the spacing between the beads but is instead due to the DNA double strands that are positioned in the gaps between the beads

7 SPS chains as Switchable Filtration Network

The formation of chain-like SPS in microfluidic systems has previously been employed by the group of Lacharme *et al.*[38] to create a type of filtration device . In their experiments, they formed SPS chains of superparamagnetic beads that were caught in grooves in the channel walls (see Figure 7.1). The surface of the beads was utilized as the solid support for a sandwich immunoassay. A solution containing the analyte was flushed through the channel, passing the trapped SPS chains which captured analytes with their functionalized surface. The presence or absence of analyte could later be determined by fluorescence spectroscopy.

In this experiment, it was tried to create an enhanced mechanism for filtration by SPS chains. Instead of capturing chains in grooves where they remain statical throughout the experiment, chains were to be anchored on the wall and folded into or out of the channel by a reorientation of

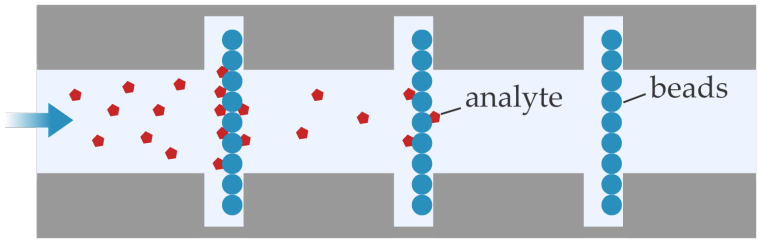

Figure 7.1: On-chip sandwich immunoassay procedure developed by Lacharme *et al.*[38]. SPS chains that were caught in groves in the channel walls were used as a filtration device. Analyte molecules from the sample were caught on the functionalized surface of the chains and later detected with fluorescence spectroscopy.

the magnetic field. A sketch of this method is shown in Figure 7.2. At a high density of SPS chains, a network capable of thorough filtration is created that can be activated or deactivated by influencing the external (homogeneous) magnetic field.

To anchor beads to the channel walls, the wall was functionalized with (3-Aminopropyl)triethoxysilane (APTES, see Figure 7.3 for information on the chemical structure). Under neutral or acidic pH conditions, the NH_2 group of APTES is protonated to NH_3^+, resulting in a positive surface charge. As streptavidin beads have a negative surface charge under neutral pH conditions[1], streptavidin beads are electrostatically attracted to and adsorbed by the surface. This method has already been successfully applied by Sivagnanam *et al.* [151].

Although the according experiments show promising results, this is still a work in progress. Therefore, the results given in the following sections represent intermediate results. The project has been performed by Patrick Stohmann in his Master thesis.

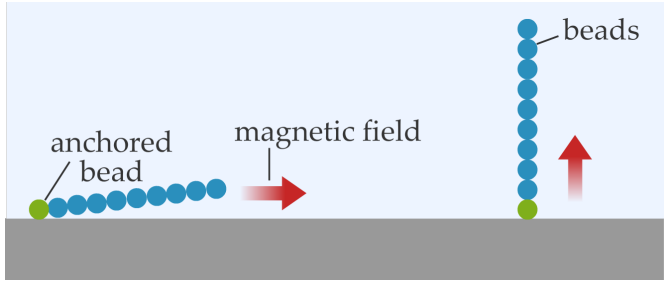

Figure 7.2: Schematics of the switchable filtration network. A single bead is bound to the surface of the channel walls and serves as a magnetic anchor for an SPS chain. By reorienting the direction of the external homogeneous field, the chains can be moved into or out of the liquid flow in the channel, thus activating or deactivating the filtration function.

1 The iso-electric point of streptavidin is around 5.0 [150].

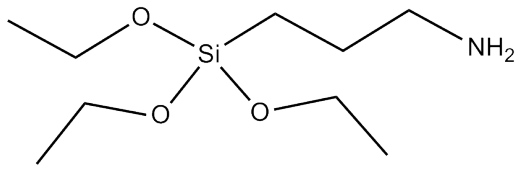

Figure 7.3: Chemical structure of (3-Aminopropyl)triethoxysilane (APTES).

7.1 Materials and Methods

Two different electromagnetic coil setups have been used in this experiment. For the field in flow direction, the coil setup discussed in section 3.4 was utilized. The field in z-direction (orthogonal to the substrate surface) has been supplied by a cylindrical Helmholtz coil with an inner diameter of 7.5 cm, an outer diameter of 13.5 cm and a height of 7.5 cm. The coil gave a magnetic field strength of 55 Oe/A.

The preparation of PDMS channels was performed through soft-lithography, as described in section 3.1.

The observation of the SPS behaviour has been performed with the microscopy setup described in section 3.3.

APTES was obtained from Sigma-Aldrich.

7.2 Experiments

For this experiment, single beads (Dynabeads MyOne SA or M-280 SA) were bound to APTES spots located on the bottom of the channel, as previously described by Sivagnanam *et al.*[151]. Afterwards, a bead dispersion was flushed through the channel while a homogeneous magnetic field was applied in z-direction (orthogonal to the surface on which the anchor beads were bound). Beads were attracted towards the anchor beads and aligned in SPS chains along the direction of the magnetic field. After the chains were formed, the signals received by the coils were changed to the pattern shown in Figure 7.4. This lead to a rotation of the magnetic field vector from the x- through the z- to the -x-direction, with x as the direction of the flow.

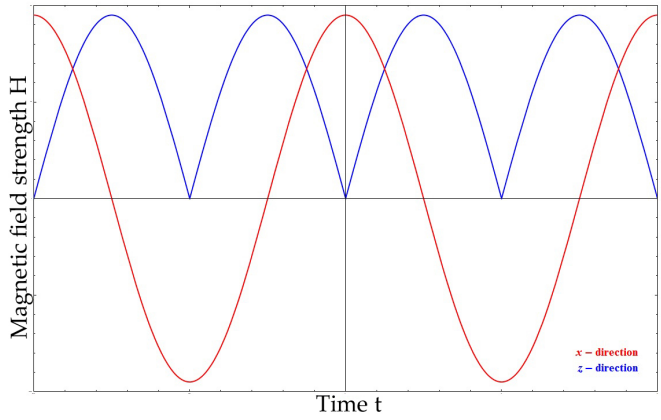

Figure 7.4: Schematics of the signals supplied to the electromagnetic coils. The red curve gives the signal for the field in x-direction, the blue one for the z-direction. Switching times (from x to -x) were on the order of tens of seconds.

7.2.1 Preparation of APTES spots

AR-P 5350 was spin-coated on a silicon wafer substrate and exposed with a UV-laser (as described in section 3.1) to create a structure with circular resist-free spots of between 2.0 µm and 4.0 µm diameter for the M-280 beads and 2.0 µm for the MyOne beads. The distance between the spots was set to 50 µm in flow direction and 15 µm orthogonal to the flow direction. The slide was developed and oxidized for 30 s in an oxygen plasma at 0.1 mbar. A 1.0 vol.-% solution of APTES in distilled water was spin-coated on the substrate at 5000 rpm for 30 s. Afterwards, the substrate was heated to 100 °C for 2 minutes to enable a covalent binding of the APTES molecules to the Si surface. This process yielded APTES-spots of 2.0 µm to 4.0 µm diameter. To remove the remaining resist, the substrate was cleaned with acetone in an ultrasonic batch for approximately one minute. This process did not detach the covalently bond APTES molecules.

To incorporate the spots into a microfluidic channel, a PDMS channel system of 100 µm width was prepared. The PDMS and the Si-wafer with the APTES spots were oxidized in an oxygen plasma at 0.1 mbar for a duration

of 30 s. During this time, the spots were covered by a glass cover slide to prevent oxidation of the APTES. Afterwards, the PDMS channel was positioned over the APTES spots and pressed onto the wafer to facilitate bonding between PDMS and the oxidized wafer surface.

7.2.2 Anchoring of Chains and Switching Procedure

Aqueous dispersions of Dynabeads MyOne SA and M-280 SA at a concentration of roughly[1] 400 µg mL^{-1} containing 0.5 % Tween 20 were prepared and injected into the channel system. After beads bound to the APTES spots, a homogeneous magnetic field oriented in z-direction (orthogonal to the wafer surface) was applied by an electromagnetic coil to form SPS chains inside the channel. The field strength was adjusted to 100 Oe. An additional coil allowed to switch to a homogeneous magnetic field facing in flow direction. The switching was performed with sinusoidal signals as depicted in Figure 7.4 to obtain a smooth transition between the x- and the z-direction. Thus, the magnetic field vector was constantly switched from the +x to the +z and then to the -x direction, followed by an inverse switch back to the +x direction. The total magnetic field strength (independent of direction) for this experimental procedure was increased to 250 Oe.

The experiment was performed at different flow velocities. The velocity was evaluated by tracking magnetic beads that were subject to the liquid flow.

7.3 Results and Discussion

The experiments showed that Dynabeads MyOne SA and Dynabeads M-280 SA could both be successfully anchored on the APTES spots on the bottom of the channel (see Figure 7.5). Different spot sizes did not yield significantly different results. The only difference was found to be in the

1 The actual concentration of the dispersion is not relevant for the experiment, as the local concentration of beads changes significantly due to the retention of beads over the APTES spots. Within these experiments, concentrations in the range of 100 µg mL^{-1} to 400 µg mL^{-1} were tested.

number of beads that were anchored to one spot. A thorough investigation of this influence, however, has yet to be performed.

When a magnetic field was applied in z-direction, the dipolar interactions of the magnetic fields of the beads lead to the formation of chain-like SPS that were positioned on top of the APTES spots, with the lowest bead being anchored to the spot. The chains could successfully be switched from the z-direction to the +x- or -x-direction (see Figure 7.5). However, at flow velocities of about 100 µm s^{-1}, the chains could not be turned into the -x-direction (against the flow), as the shear forces worked against the movement into this direction. Chains fractured when the magnetic field was turned out of the direction of the axis of the chain structure. The reason for this is that the attractive forces between the particles decrease when the magnetic field vectors of the beads deviate from the chain axis [36,42]. However, turning the chains into the +x-direction and the z-direction was possible.

Fracturing of chains always occured between the anchor bead and the first magnetically attracted bead, never between the anchor bead and the APTES field, showing that the electrostatic forces between APTES and beads are indeed strong enough to ensure a sufficient binding strength.

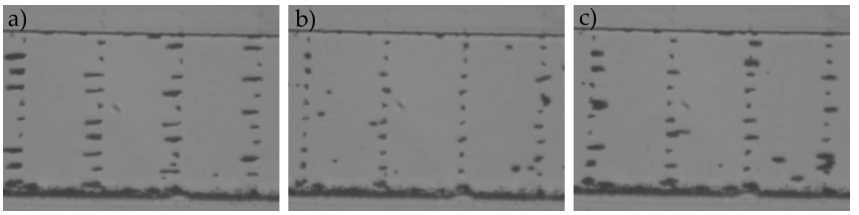

Figure 7.5: SPS chains captured on APTES spots in a microfluidic channel of 100 µm width. (a) Under the influence of a magnetic field orthogonal to the image plane (z-direction), chains of beads agglomerate on top of anchor beads that are bound to ATPES spots on the channel surface. Switching the direction of the magnetic field into the flow direction turns the chains so that they come to lie flat on the surface. (b) If the field is returned to the z-direction, the chains follow. (c) Turning the chains against the flow direction only works partially, as the fluid flow pushes against this motion. This results in chains that come to rest at an angle α between 90° and 0°. The switching times for the experiments were on the order of seconds.

7.4 Conclusion

In this experiment, SPS chains were successfully self-assembled on top of anchor beads that were bound to APTES spots on the bottom of the channel. Using electromagnetic coils that provided a homogeneous magnetic field whose direction could be changed between the x- and the z-direction it was possible to switch between three states where the chains were facing in +x-, -x- or z-direction. However, the system requires flow velocities below 100 µm s^{-1} to turn chains into the -x-direction. Above this velocity, chain fracturing becomes a problem. Critical flow velocities for the +x-direction need yet to be determined.

As the chain network can be activated or deactivated by a reorientation of the external field, the system is a much more flexible filtration device than the one designed by Lacharme *et al.*[38]. As a downside, it requires additional structuring of APTES spots on the bottom of the channel.

7.5 Outlook

The next step is a further evaluation of the stability of the bead chains to find threshold flow velocities above which the chains detach from the anchor beads. Additionally, different bead species should be tested to determine the optimum balance between magnetic force and drag force acting on the beads.

To prove that this system can be used as a filtration network, biotinylized sample molecules need to be introduced into the system. The streptavidin-covered beads would then capture the sample molecules from the solution. The presence of the molecules would have to be proven by a suitable detection method, e.g. fluorescence spectroscopy, depending on the characteristics of the sample molecules.

In the next step, the system could be used to filtrate arbitrary analyte molecules from solution. For this, the beads constituting the SPS chains (not the anchor beads) would have to be functionalized so that they specifically capture the analyte.

8 Beads for Surface Enhanced Raman Spectroscopy

As sample volumes within µ-TAS are on the order of nano- to picoliters, sensitive detection methods are required to obtain reliable analysis results. These detection methods have to be able to work under aqueous conditions and should require no contact between a sensor surface and the sample, as biofouling[1] will quickly deteriorate the surface and change the sensor response with time. If surface contact is required, the surface should clean or replenish itself to sustain a constant sensor signal.

While surface-enhanced Raman spectroscopy (SERS) is a very sensitive detection method with the potential for single-molecule analysis [95,96,97,98], it does not satisfy the no-surface condition. SERS requires a metal surface such as gold or silver to obtain an enhancement of the Raman signal, usually in the form of metal-coated channel walls or metallic nanoparticles. However, while surface-coatings suffer from biofouling and high fabrication costs, metal nanoparticles are hard to retain inside of a certain detection volume due to their low size and their large diffusion coefficient. Thus, both approaches possess severe disadvantages for application within microfluidic systems.

The use of gold-covered superparamagnetic beads may serve as a feasible alternative. The surface of the beads, covered with a SERS active gold layer, could be used as a sensor surface. Using magnetic fields, the beads could be held in place at the site of detection. By using rotating magnetic fields, the

1 The term biofouling refers to the accumulation of biological material on surfaces within the microfluidic system. When biological samples like blood or saliva are analysed, proteins, DNA or even whole cells can attach to sensor surfaces and thus decrease the sensing quality.

process of forming tightly packed monolayers of beads that was developed by Wittbracht *et al.*[43] and has already been presented in chapter 6 can be used to form islands of SERS active beads that serve as the sensing surface (see Figure 8.1). To counteract biofouling, the islands can be disassembled at regular intervals by deactivating the magnetic field. New islands can be formed rapidly, thus ensuring that the metal surface remains free of contaminants.

In this work, gold-covered superparamagnetic beads were synthesized and used as mobile substrates for SERS detection of 4-mercaptobenzoic acid (4-MBA, see Figure 8.2). The beads were fabricated by binding gold nanoparticles to thiol-functionalized silica beads (see Figure 8.3). The thiol-groups formed chemical bonds with the gold surface, thus immobilizing the nanoparticles on the bead surface. 4-MBA was deposited on the gold surface *via* its thiol-groups and detected with SERS.

Talley *et al.*[152] showed that 4-MBA molecules immobilized on silver nanoparticles could be used as local pH sensors: Vibrations of the deprotonated carboxylic acid group can be found in the Raman spectrum of the molecule. The signal intensity depends on the amount of deprotonated molecules, which in turn depends on the pH value of the solution. Thus, the spectrum can be used to determine the pH of the medium. To test whether the SERS active beads with 4-MBA covering could be used as magnetically guidable, local pH sensors, their SERS spectra in solutions of different pH values were collected.

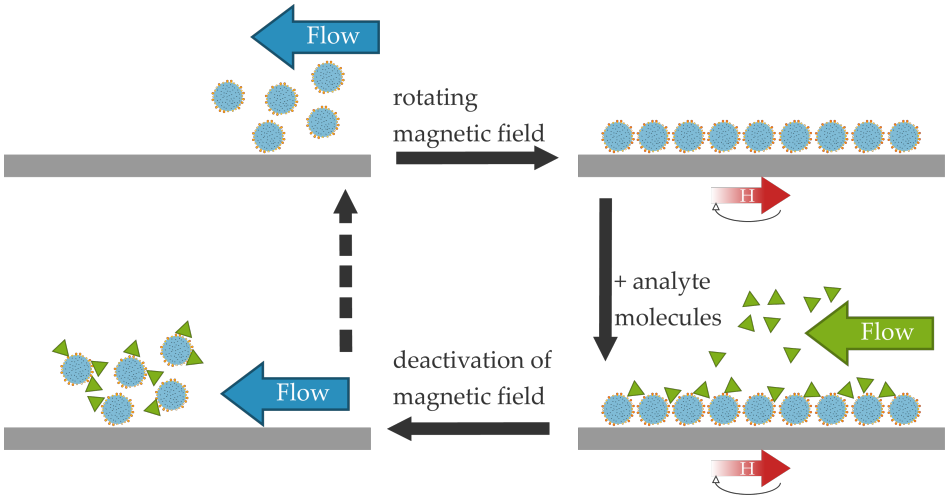

Figure 8.1: Schematics of the formation of a SERS sensor surface from gold-coated beads. In the absence of a magnetic field, the beads are introduced into the system. Under the influence of a rotating, homogeneous magnetic field, they assemble into an ordered monolayer. When analyte molecules are introduced, they attach to the gold surface and can thus be detected *via* SERS measurements. Subsequent to the measurement, the magnetic field is switched off and beads as well as the attached analyte molecules are released. A new sensor surface can be prepared by repeating the steps, thus supplying an uncontaminated surface for the measurement.

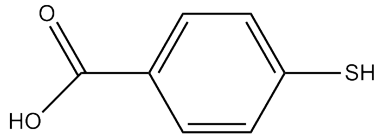

Figure 8.2: Chemical structure of 4-mercaptobenzoic acid.

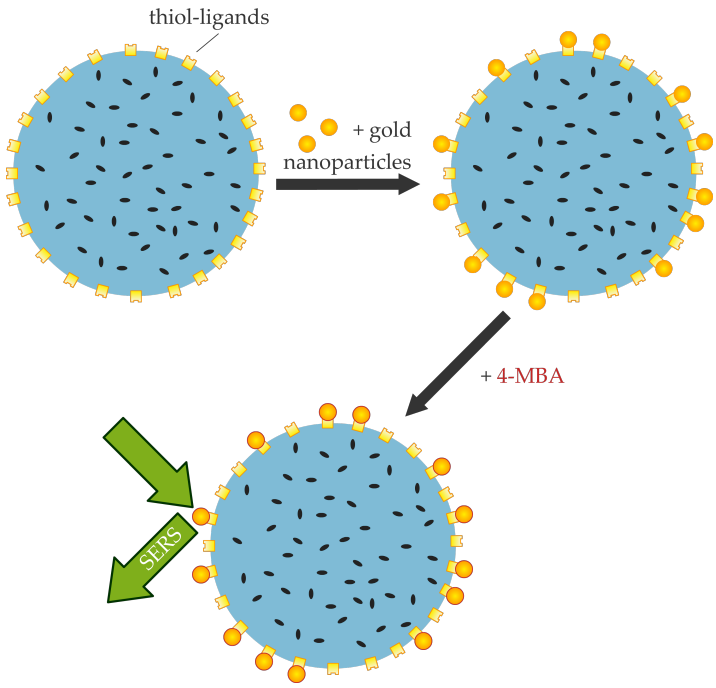

Figure 8.3: To synthesize gold-covered, SERS-active beads, gold nanoparticles were mixed with microbeads with a thiolized surface. The thiol groups form chemical bonds with the gold surface, thus binding the gold nanoparticles on the bead surface. Afterwards, 4-MBA is added, which attaches itself to the gold nanoparticles through thiol bonds. SERS probing of the nanoparticle surface should then yield SERS spectra of 4-MBA.

8.1 Materials and Methods

The superparamagnetic beads used for these experiments were SiMAG-Thiol beads (chemicell). These beads consist of silica spheres of 1 µm diameter (polydispersity index[1] of 0.24-0.26) and have a thiol-functionalized surface.

1 The polydispersity index is defined as the ratio of the weight-average molar mass M_w and the number-average molar mass M_n.

Their mass saturation magnetization is $2.9\,\mathrm{A\,m^2\,kg^{-1}}$. The gold nanoparticles (average diameter: (25 ± 12) nm) were obtained from Particular, as their laser ablation synthesis method produces nanoparticles that can be stabilized with a minimum amount of surface ligands, thus making binding between the thiol groups on the beads and the gold surface of the nanoparticles easier.

The spectroscopical analysis was performed by Lena Böhling from the Physical Chemistry I group of Bielefeld University. The data was collected using a UV2501PC spectrometer (Shimadzu). The path length was 1 cm.

The SERS experiments were performed by Elina Oberlander in the group Biomolecular Photonics of Bielefeld University. The Raman spectroscopy setup is described in section 3.5.

4-MBA was obtained from Sigma-Aldrich.

8.2 Experiments

The experimental section is divided into three subdivisions. The first section describes the fabrication of the gold-nanoparticle-covered beads. The second section describes the addition of 4-MBA to the nanoparticle surface and the recording of the SERS spectra. The last section gives the protocol for the recording of SERS spectra in solutions of different pH values to test whether the beads could be used as local pH sensors.

8.2.1 Fabrication of gold-nanoparticle covered beads

To fabricate the gold-nanoparticle covered beads, several batches containing a mixture of 10 µL SiMAG-Thiol beads and 150 µL gold nanoparticles each were prepared in 1.5 mL Eppendorf tubes. They were kept on a shaking plate (Thermo Twister Comfort, quantifoil instruments) at 20 °C at a shaking speed setting of 7. After 1,2,3 and 4 days, one Eppendorf tube was taken from the plate. The beads inside of the tube were separated with a magnet and the supernatant was analyzed with absorption spectroscopy to determine the concentration of the remaining nanoparticles. The remaining, unseparated vials were vortexed to stir up the beads that had settled in spite of the constant shaking and placed onto the shaking plate.

For the absorption spectroscopy analysis, 100 µL of the supernatant were mixed with 1.9 mL H_2O (bidest) and measured in a UV2501PC spectrometer (Shimadzu). To calculate the extinction coefficient of the nanoparticle solution, 10 µL of the stock solution (500 mg mL^{-1}) were mixed with 1.99 mL H_2O (bidest).

The nanoparticle-covered beads were analyzed with energy-dispersive X-ray spectroscopy (EDX) to show the presence of the gold nanoparticles. For this, the EDX system EDAX Apollo 10, integrated into a FEI Helios NanoLab 600 DualBeam focused ion beam device, was used. The device also allowed SEM imaging of the particles. For the measurements, a voltage of 20 kV and a current of 86 pA were used. The measurements were performed by Karsten Rott.

To deposit 4-MBA on the nanoparticle surface, the nanoparticle-covered beads obtained at day 4 were mixed with 40 µL of a saturated 4-MBA ethanol solution. The beads were put on a shaking plate over night. The next morning, the beads were separated with a magnet and the supernatant with the remaining 4-MBA was removed. The beads were washed by adding 50 µL H_2O (tridest), separating the beads and removing the supernatant. Finally, the beads were taken up in another 50 µL of H_2O (tridest).

To test the SERS activity of the beads, bead samples with and without 4-MBA were introduced into a Raman laser setup. For this, 10 µL of the bead dispersion were diluted with 150 µL H_2O (tridest). 2 µL droplets of the resulting dispersion were deposited on a glass slide and analysed with the previously described SERS setup (see section 3.5). Detailed parameters for the spectra, e.g. laser power, diffraction grating, exposure time etc., are given in the results and discussion section together with the spectra. Basically, three different spatial arrangements that were expected to change the characteristics of the spectrum need to be distinguished. In arrangement one, the beads settled onto the underlying glass substrate by gravitational forces, resulting in a random, non-uniform, patchy pattern of beads. In arrangement two, the beads were forced onto the substrate by a permanent magnet that was positioned underneath the substrate. This resulted in a tight but mainly amorphous packing of beads. The third method used the formation of bead monolayers in rotating magnetic fields (see chapter 2.2 or the work by Weddemann *et al.*[43]). For this, the sample

was put on an IKA RCT basic magnetic stirrer with 690 Oe maximum field strength. The rotation frequency was set to 500 rpm. Note, however, that while the first and second method could be used in dispersion, the third method required that the sample was dried on the stirrer, otherwise the crystalline arrangement would have been destroyed by the removal of the magnetic field. Exchanging the magnetic field of the stirrer with that of a permanent magnet put underneath the sample was not an option, either, as the introduction of the magnet would have destroyed the monolayers through the formation of large, multi-layered agglomerates. The method with which the spectra were obtained is mentioned in the figure captions.

To test whether the spectra would show a pH-dependence, dispersions with different pH-values were prepared by mixing 2 µL of the washed sample of beads with gold-nanoparticles and 4-MBA covering (preparation: see above) with 150 µL of a solution which was pH adjusted with HCl and NaOH. It was assumed that the low volume of the bead dispersion would not significantly influence the pH value. These dispersions were evaluated as described above.

8.3 Results and Discussion

SEM imaging of the beads after the addition of gold nanoparticles shows gold nanoparticles that are attached to the bead surface. However, the beads themselves lose their spherical shape under the influence of the vacuum, as water is drawn out of the silica matrix. The beads collapse and form amorphous agglomerates, as can be seen in Figure 8.4. Nevertheless, the presence of gold can be seen in the EDX spectrum that is shown in Figure 8.5. The measurement over the area of several beads clearly shows signals for Fe (from the superparamagnetic iron oxide nanoparticles inside the beads), Si (from the silica sphere and the silicon substrate underneath the beads) and Au (from the gold nanoparticles). A measurement of the substrate without beads (inlet in Figure 8.5) proves that the Fe and Au signals are caused by the beads and not by the substrate.

The absorption spectra of the supernatant from the nanoparticle binding experiments are shown in Figure 8.6. As can be seen from the spectra,

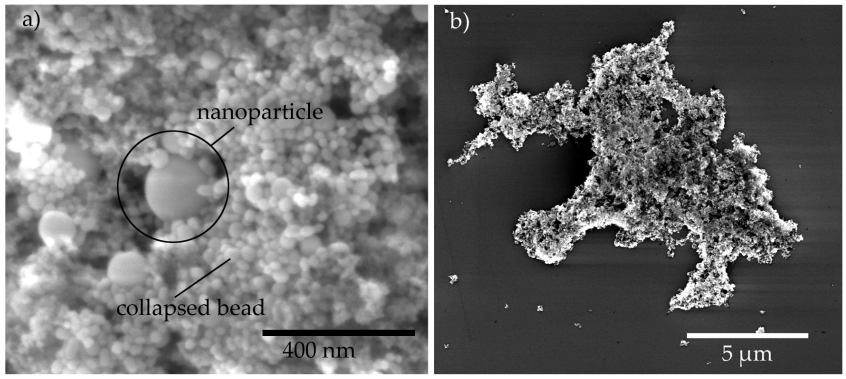

Figure 8.4: a) REM image of gold-nanoparticles on SiMAG Thiol beads. The silica beads collapsed as the REM vacuum drained the water from the silica matrix. b) REM image of a cluster agglomerate. Under the influence of the vacuum, the silica beads collapse and form amorphous agglomerates. Both images do not mirror the native states of the silica beads in dispersion, but show that gold nanoparticles did indeed bind to the bead surface.

the nanoparticles show a strong absorption at 536 nm (see the spectrum of the diluted stock solution). The decrease in signal intensity with each day proves that nanoparticles were bound by the thiol-covered silica beads. At day 3 and 4 the binding was complete and 100 % of the nanoparticles were bound to the surface[1]. These two samples were used for the following experiments.

The SERS probing of the beads gave Raman spectra of 4-MBA. Figure 8.7 shows such a SERS spectrum of 4-MBA with assignment of the peaks that are most relevant for this work. The signal intensity clearly indicates a SERS effect, as the intensities would otherwise be significantly lower. For further information about the 4-MBA spectrum, the reader is referred to the literature[153,154,155]. Figure 8.8 shows a comparison between the spectra

1 It has to be noted, however, that the scattering background was substracted from the spectra. If nanoparticles have agglomerated during the experiment, they were not detected in the supernatant and therefore the real percentage of bound nanoparticles would be slightly lower.

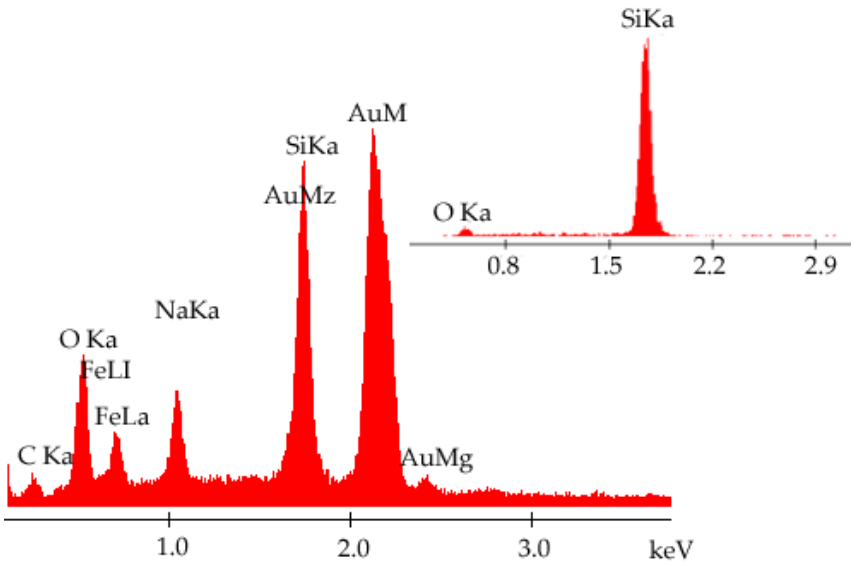

Figure 8.5: EDX spectrum of the SiMAG-Thiol beads covered with gold nanoparticles. The spectrum contains the Fe peaks of the superparamagnetic iron oxide nanoparticles, the Si peaks of the silica sphere and the silicon substrate and the Au signal of the gold nanoparticles on the surface. The inlet shows a measurement of an area of substrate without beads. The absence of Fe and Au peaks shows that the signals are caused by the presence of beads. The spectra were collected by Karsten Rott with a focused ion beam device (Helios Nanolab Dual Beam 600i, FEI) that contained an EDAX Apollo 10 EDX system. The data was obtained at 20 keV and 86 pA.

of beads with and beads without 4-MBA on the nanoparticle surface. As can be seen from the marked peaks, the main peaks of 4-MBA do not show up in the spectrum of the blind, thus proving that 4-MBA can be detected with this method.

The three agglomeration states (dispersion, amorphous agglomerate and crystalline monolayer) that were tested yielded different results concerning the signal-to-noise ratio. Figure 8.11 shows spectra obtained from these three states. Note that the signal of the spectrum obtained from the

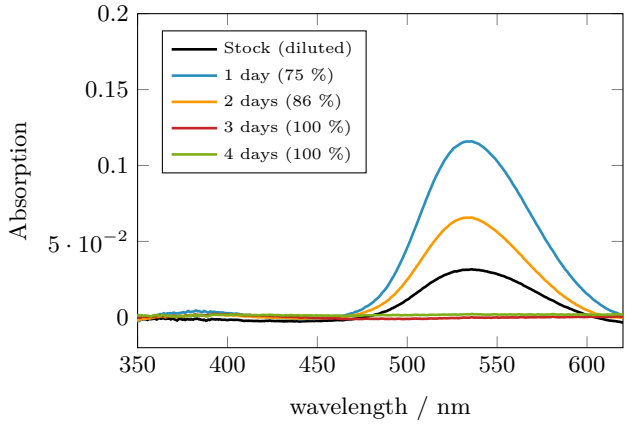

Figure 8.6: Absorption spectra of the diluted gold nanoparticle stock solution (black) and the supernatant from the bead synthesis process (colors). As can be seen from the decrease in signal intensity, the amount of remaining, unbound nanoparticles decreased with each day, until nearly 100 % of all particles have been bound to the surface on day 3 and 4. The calculated ratio of particles bound to the beads is given in the legend.

dispersion was multiplied with a factor of 10. As can be seen from these results, good signal-to-noise ratios require bead agglomerates. However, whether these agglomerates are amorphous or ordered monolayers hardly influences the signal (the differences between the two according spectra are within the error margin of the measurement. The reason for this is probably as follows: Research on the SERS effect revealed that the best signal enhancements are usually obtained in the region between two metal surfaces, in so-called hot spots [156,157] (see Figure 8.9). It would be possible that the nanoparticles on one bead are not as densely packed as when two beads and their nanoparticle surfaces contact each other. In the latter case, the resulting hot spots give a superior signal enhancement. Thus, for final applications, bead agglomerates could be created through rotating homogeneous magnetic fields (resulting in monolayers) or simply by local gradient fields that create amorphous agglomerates, without loss in signal enhancement.

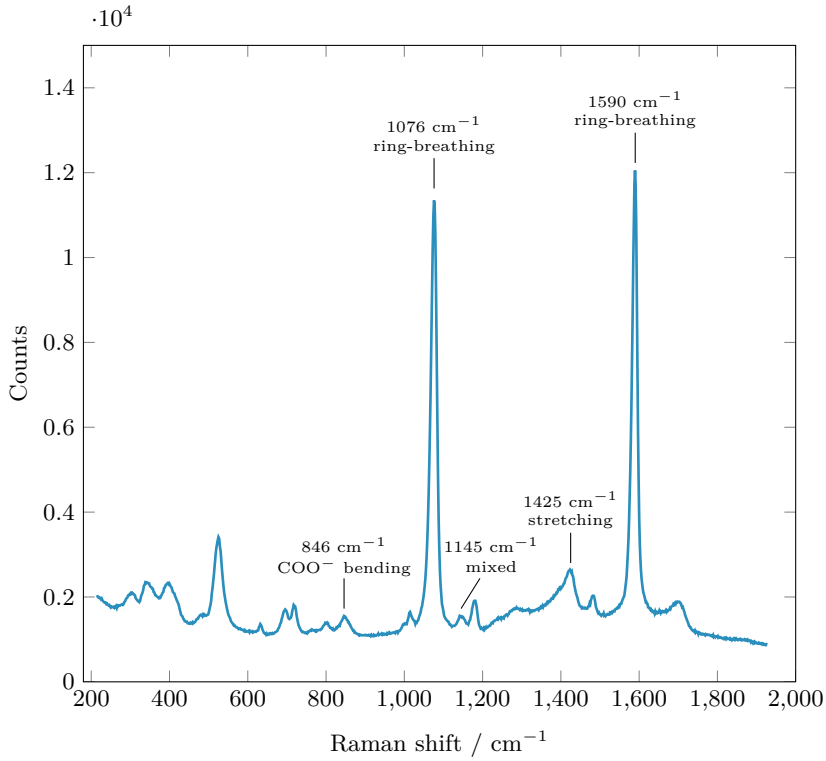

Figure 8.7: Surface Enhanced Raman spectrum of the 4-MBA covered gold nanoparticles bound to beads. The prominent peaks at 1076 cm^{-1} and 1590 cm^{-1} correspond to breathing modes of the benzene ring. The spectrum shows several peaks that are influenced by a deprotonation of the acid group and are therefore dependent on the pH value of the surrounding medium, namely the COO^- bending mode at 846 cm^{-1}, a mixed mode at 1145 cm^{-1} and a stretching mode at 1425 cm^{-1}. More details about the structure of the spectrum, including spectra of pure 4-MBA, can be found in the literature[153,154,155]. The spectrum was obtained at a wavelength of 785 nm and a power of 9.5 mW using a diffraction grating with 600 grooves mm^{-1}. It was accumulated from 3 measurements of 3 s, each.

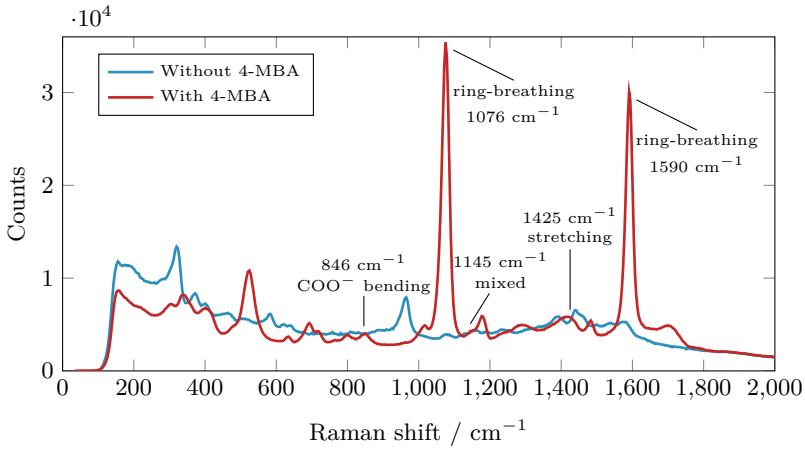

Figure 8.8: Spectra of bead dispersions with and without 4-MBA covering the nanoparticle surface. It can clearly be seen that the presence of 4-MBA in the sample yields strong signals of the ring-breathing mode at 1076 cm^{-1} and 1590 cm^{-1}. Other, less intense peaks can be found in the spectrum as well. The absence of these peaks in the blind proves that the signals are caused by the 4-MBA molecules on the nanoparticle surface. For the red curve, a power of 19.2 mW was used, the blue curve was collected with 29.2 mW output. The spectra were accumulated from 3 measurements of 3 s, each, using a diffraction grating with 300 grooves mm^{-1}. The spectrum without 4-MBA was obtained from solution, the spectrum with 4-MBA was obtained from a dried monolayer that was arranged with the stirring device.

Admittedly, however, it has to be said that it cannot be proven that the microparticles did indeed arrange in a crystalline monolayer. Compared to the particles used in a previous study [43], the size distribution of the silica particles is rather broad (polydispersity index of 0.24-0.26), making the arrangement into an ordered layer difficult. In microscopy images gathered with a common light microscope, the beads cannot be completely resolved (see Figure 8.10). However, the images show an even distribution of the particles that resembles the shape of the monolayers obtained in [43]. High-resolution microscopy like TEM or SEM imaging, however, was not possible, as the vacuum removes the water from the silica matrix and

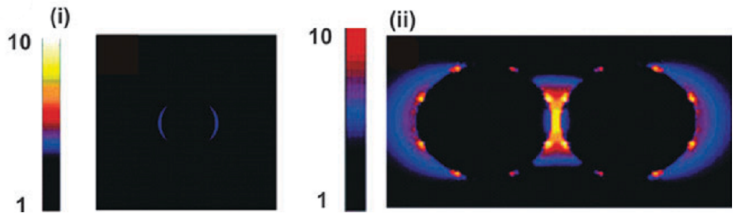

Figure 8.9: Electromagnetic near-field enhancement at an excitation wavelength of 633 nm for (i) an isolated Au nanosphere and (ii) a nanosphere pair with interparticle axis parallel to the incident polarization [157]. It can clearly be seen that the enhancement effect is significantly stronger in the hot spot region between two spheres. Reprinted with permission. Copyright 2005, American Chemical Society.

leads to a collapse of the particle shell (see Figure 8.4). Experiments with re-functionalized Dynabeads (low size deviation) are planned, but have not been performed, yet. For these experiments, MyOne beads with a carboxylate surface are to be functionalized with cytosine which binds to gold surfaces.

When comparing the spectra of the 4-MBA beads at different pH values (see Figure 8.12), a change in the intensity of the COO^- stretching vibration at 1425 cm^{-1} can be observed. As the pH increases, an increasing percentage of the 4-MBA molecules becomes deprotonated. Thus, more COO^- groups are formed which leads to an increase in the corresponding Raman signal. This provides a method to determine the pH value of unknown aqueous solutions. For this, the relative peak area of the pH-sensitive peak at 1425 cm^{-1} and the non-pH-sensitive peak at 1590 cm^{-1} (a ring breathing mode from the benzene ring) is measured. The ratio of the two values is then compared to the pH value of the solution (see Figure 8.13).

The resulting plot shows a clear dependency of the signal ratio on the pH value. However, measurements taken at different spots of the same sample reveal a large standard deviation (see Figure 8.13). This standard deviation is likely to result from local variations of the pH value close to surfaces. Variations in the ion concentrations (e.g. caused by the electrical double layer) can lead to such local variations. In hot spots, the space

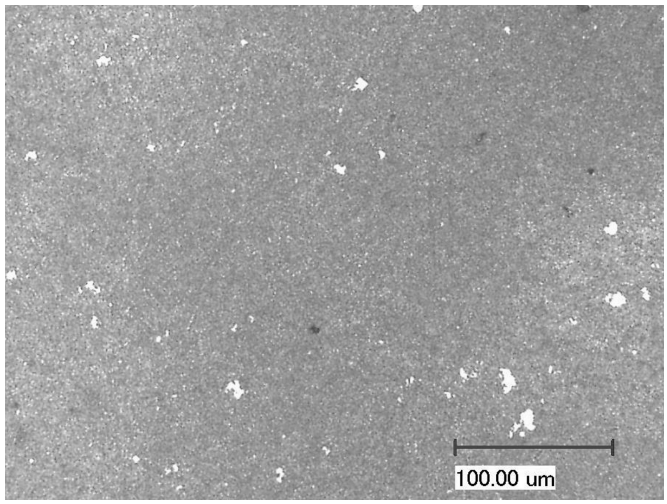

Figure 8.10: Image of a dispersion containing SiMAG Thiol beads that were clustered by a rotating magnetic field supplied by an IKA RCT magnetic stirrer. Although a nearly homogeneous covering is achieved, the monolayer quality is far inferior to the monolayers prepared with M-280 beads (see chapter 6).

between nanoparticle surfaces is very small. Thus, it can be assumed that such variations have a maximum of influence in such spots. Since 4-MBA molecules at hot spots between nanoparticles give the strongest signal enhancements, the signal is significantly altered by this effect. To utilize this method as a pH sensor, the reliability of the measurements needs to be increased, meaning that particle spacing would have to be optimized. Currently, the chaotic arrangement of nanoparticles on the bead surface creates hot-spots of arbitrary size. This could be solved by locating the hot spots inside or at the surface of the nanoparticles. The nanocrescents [158,159] developed by Luke P. Lee and co-workers at UC Berkeley, USA, would be an ideal candidate for this. Here, the hot spots are located near the opening of the cavity of the structure (see Figure 8.14).

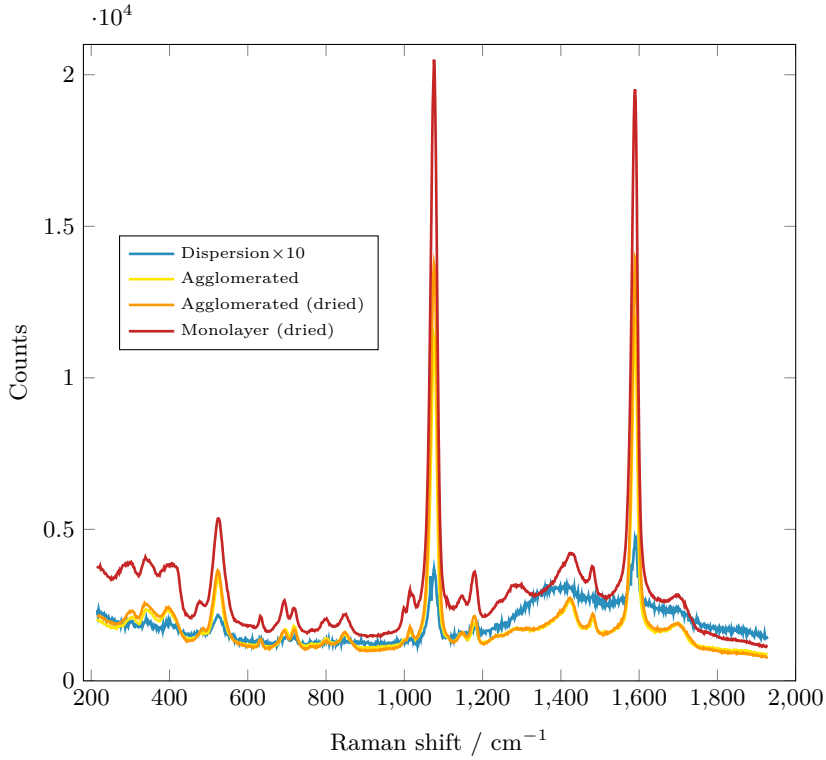

Figure 8.11: SERS spectra of the 4-MBA covered gold nanoparticles bound to beads at different stages of bead aggregation. First, the pure bead dispersion is examined (*dispersion*). Then, beads are agglomerated by holding a magnet underneath the glass slide (*agglomerated*). Spectra are recorded with and without (*dried*) surrounding liquid. Lastly, a monolayer of beads is formed in a rotating magnetic field of 600 rpm and 330 Oe. As the signal of the bead dispersion is very weak, it was multiplied with a factor of 10 to compare it with the other spectra. As can be seen from the graphs, the agglomerated and the monolayer spectra show similar signal intensities. There is no noticeable difference between the signal for the *agglomerated* sample in the dried or the liquid state. All spectra were recorded at a wavelength of 785 nm and a power of 9.5 mW. They were accumulated from 3 measurements of 3 s, each.

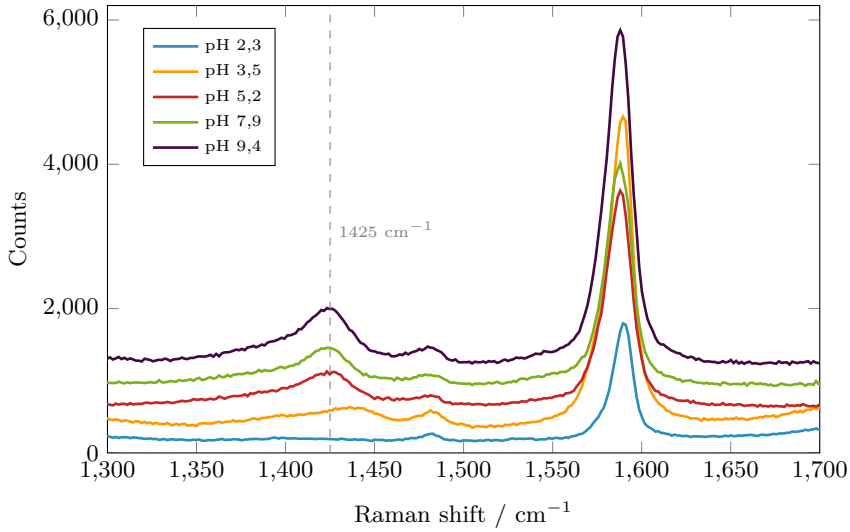

Figure 8.12: SERS spectra of 4-MBA-Beads at different pH values. As can be seen from the spectra, the signal strength of the COO^- stretching vibration at 1425 cm^{-1} depends strongly on the pH. As the benzene ring is not influenced by the pH, the signals from this region (here: the breathing mode at 1590 cm^{-1}) are not pH sensitive. Thus, the ratio of the 1425 cm^{-1} peak to the 1590 cm^{-1} peak can be used to measure the pH value of the surrounding liquid. Offsets were applied to the curves to obtain an ordering of the curves.

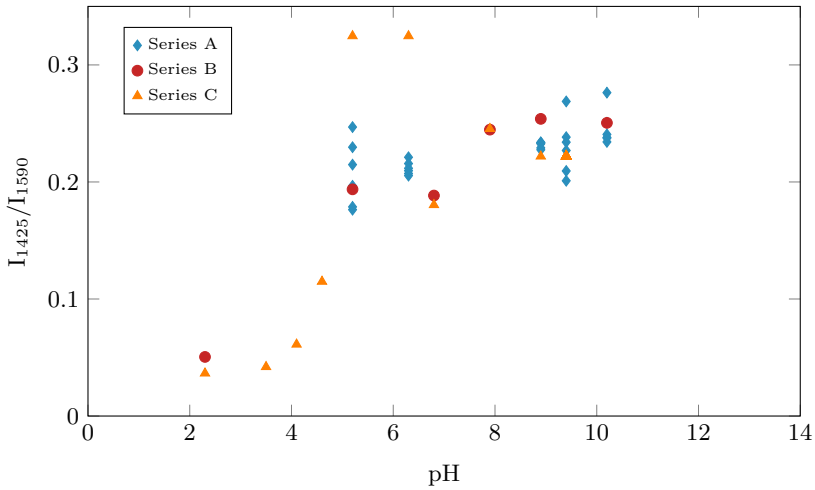

Figure 8.13: Ratio of the intensity of the signal at 1425 cm^{-1} and the signal at 1590 cm^{-1}. As can be seen from the plots, the ratio depends on the pH of the solution. For a method to test the pH with the help of the 4-MBA beads, however, a method to obtain more reliable results needs to be found.

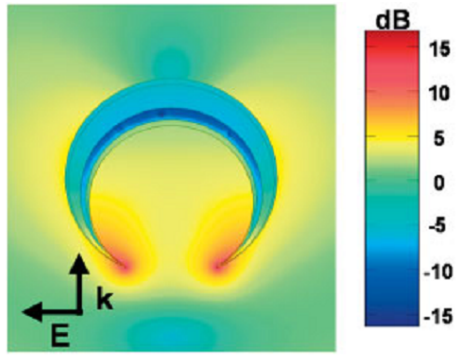

Figure 8.14: Simulated local electric-field-amplitude enhancement in dB by a single nanocrescent [158]. The nanocrescent is oriented 0° with respect to the 785 nm light-incident direction. Reprinted with permission. Copyright 2005, John Wiley and Sons.

8.4 Conclusion

It was successfully shown that gold nanoparticles could be bound to the surface of superparamagnetic beads that are functionalized with thiol-groups. Attaching 4-MBA to the nanoparticle surface gave rise to Raman spectra when probing the bead surface in a SERS setup. As the signal intensity can only be explained through the SERS effect, it was successfully shown that nanoparticle covered beads can be used as a SERS sensing surface, offering new possibilities for self-assembling sensor surfaces in microfluidic systems. Beads arranged in clusters gave better signal-to-noise ratios than non-agglomerated beads. However, it did not matter whether the clusters were crystalline or amorphous.

Additionally, it was shown that the signal intensity of the COO^- vibration at 1425 cm^{-1} depends on the pH of the surrounding medium. When the signal intensity was normalized with the intensity of the ring-breathing mode at 1590 cm^{-1}, the resulting value was directly related to the pH of the solution. Thus, nanoparticle covered beads could be used as local pH sensors that can be guided by magnetic fields, theoretically enabling the pH testing within cells or at different locations in/near a biofilm. However, repeated measurements showed a low reproducibility of the obtained values. This problem was already encountered by Talley *et al.*[152].

8.5 Outlook

At the current state of the project, the reproducibility of the pH measurements is not high enough to give reliable results. As mentioned in the discussion, the chaotic arrangement of the nanoparticles on the bead surface might be a reason, as it creates arbitrary hot-spots with different interparticle spacing. This effect could be reduced by utilizing nanoparticles where the hot spots are not on the surface (or in between) of particles, but within the particle itself, like the previously mentioned nanocrescents[158,159]. The use of such structures would make the hot-spot geometry independent of the nanoparticle arrangement on the bead. Although the local pH might still be varied by the presence of the gold surface, the variation will not depend

on the arrangement, thus giving more reliable results. Thus, the next step would be to obtain or fabricate beads that have such hollow gold spheres bound to their surface, attach 4-MBA to the gold surface and measure the SERS spectra depending on the pH value.

Alternatively, the use of superparamagnetic beads as means of magnetic assembly could be rendered unnecessary if the SERS active nanoparticles are made magnetic themselves. To the knowledge of the author, the group of Wilhelm Glomm at the Norwegian University of Science and Technology (NTNU), Trondheim, has synthesized Fe_3O_4/Au Core-Shell nanoparticles of about 30 nm size[1] that would be ideal candidates. In this case, the magnetic core of the particles would allow the formation of monolayers of the nanoparticles. Assuming a small size distribution, the hot spot size would be significantly more defined compared to the use of nanoparticle-covered superparamagnetic beads. Thus, magnetic core-shell particles could yield more reliable results.

Furthermore, microfluidic applications of the self-assembling sensor surfaces have to be tested. For this, a monolayer or amorphous agglomerate of beads needs to be assembled inside of a microfluidic channel. The layer then has to be probed while an analyte solution is pumped over or through it, testing whether the analyte molecules will bind to the gold surface and thus show SERS signals in the spectrum.

1 This information was obtained from a third party. At the point of publication of this thesis, the group has not yet published the results in a journal. For more information on this topic, the reader is referred to the webpage of Wilhelm Glomm at NTNU where the paper citation will appear once the results have been published: http://www.ntnu.edu/employees/wilhelm.r.glomm

9 Summary

In summary, it was shown that the agglomeration of superparamagnetic beads into supraparticle structures (SPS) through external static or rotating magnetic fields can be used to reduce the complexity of microfluidic devices or enable new applications. The SPS can be differentiated into one-dimensional chains and two-dimensional cluster structures. The formation of these two structure types depends strongly on the parameters of the external magnetic field. Thus, the beads can be used as self-assembling matter in microfluidic devices. While the formation of single beads into chains, chains into clusters and clusters into single beads had already been achieved, the formation of clusters into chains has previously not been possible. In this work, a method to realize this reformation process for MyOne beads has been developed. Thus, the versatility of beads as self-assembling matter has been greatly increased.

To build the base for a theoretical model that is able to predict the SPS formation, dynamical studies have been performed. In these, the initial SPS formation in dependence of bead concentration, field strength and rotation frequency has been investigated. It was found that the formation is independent of the rotation frequency but depends on the field strength and strongly on the bead concentration. Additionally, average threshold rotation frequencies above which chains fracture or form into cluster structures have been determined. The results agree with the findings of Petousis *et al.*[42] and Melle *et al.*[41]: the length L of stable SPS chains is proportional to the inverse square root of the Mason number.

Furthermore, novel applications for superparamagnetic beads and SPS in lab-on-a-chip systems have been developed. In one application, the rotation of SPS in a microfluidic channel in combination with a steric interaction with a separation barrier lead to a directed, selective movement of the SPS in one of two daughter channels. Thus, it was possible to limit the

colloidal flow of beads to one of the two channels. The system allows for the continuous-flow separation of biomolecules from a sample stream by binding them to the bead surface and separating the beads from the sample stream, as shown by the separation of biotin-coated microspheres by SPS of streptavidin-coated MyOne beads. The system has been characterized and the influence of flow velocity, rotation frequency, magnetic field strength and channel dimensions have been evaluated. Additionally, it was shown that the rotation of the SPS inside the channel enhanced the mixing between two parallel liquid flows. With the given parameters, the increase of diffusivity of FAD into a parallel water stream was found to be 32 % compared to free diffusion.

The formation of two-dimensional cluster structures in rotating magnetic fields can also be used to form highly ordered monolayers of beads. When the surface of the beads is functionalized with single-stranded DNA that is complementary to a second strand in solution, these monolayers can be passivated by hybridization between the strands. This connection between the beads of a monolayer increases the monolayer stability. The passivated monolayers then retain their stability even in the absence of a magnetic field. In addition, the process is thermoreversible, as the hybridized DNA strands can be melted by an increase in the temperature, without destroying the DNA strands. Thus, this method can be used to form robust structures that self-assemble on demand within microfluidic structures and execute various tasks, e.g. colloidal separation as presented in this work. The structures can be disassembled by a temperature increase and reassembled afterwards by a reactivation of the magnetic field. However, the reassembly process currently only yields monolayers of reduced quality.

Another application of superparamagnetic beads uses the formation of one-dimensional chains above an anchored bead that is bound to the surface *via* APTES molecules on the channel wall. These chains can be turned into or out of the flow by changing the direction of the magnetic field. With the right choice of surface functions on the beads, this system can serve as a switchable filtration network, controlled through an external magnetic field.

The final application that was developed in this work is the use of beads with gold nanoparticles bound to the surface as a mobile, magnetically controllable surface enhanced Raman scattering (SERS) sensor surface.

The beads can be assembled into a monolayer through the use of rotating magnetic fields. Analyte molecules from a sample can bind to the gold surface of the nanoparticles. Thus, the monolayer acts as an on-demand sensor surface for SERS measurements. Subsequent to the measurement, the monolayer can be disassembled to be exchanged for a fresh monolayer with beads that have an uncontaminated surface. Using 4-mercaptobenzoic acid to coat the gold nanoparticles, the system can also be used as a pH indicator, as the SERS spectrum of the 4-MBA depends on the pH value of the surrounding medium. However, further development of the system is needed to obtain reliable results.

Acknowledgments

There are a great many persons and institutions without whom this work would not have been possible. I would therefore like to use this section to give my utmost thanks to the following people and organizations:

First of all, I would like to thank my supervisor *Andreas Hütten* for his constant support, his trust in my work and the opportunity to work in his group, as a chemist among physicists.

Further thanks go towards *Frank Wittbracht* and *Alexander Weddemann* who taught me the mystic secrets of microfluidics and writing papers. May you always find steaks and cigars wherever you go.

I would also like to thank the *German National Academic Foundation* that financed my PhD scholarship and, thus, made this thesis possible. I very much enjoyed the friendly and open atmosphere of the foundation, both among the scholars and in interaction with the members of the foundation. In addition to financing my scientific studies, the GNAF scholarship gave me the freedom to skip the normally obligatory teaching and instead work on a side-project that I cherish dearly - the animus project of animated chemistry teaching.

The first few months of my thesis were financed by a scholarship by the rectorate of Bielefeld University, for which I am very thankful. Without this financial support, this work would have been over before it even began.

Huge thanks also go towards *Katharina Kohse-Höinghaus*, Professor at the PC1 group of Bielefeld University, for writing the report on my project that helped me to obtain the scholarship funding.

The results presented in this work would not have been achieved without the help of the Master students *Marianne Bartke* and *Patrick Stohmann* who showed skill, motivation and the more-than-necessary patience during their work on their thesis projects. Thank you for your effort, your interest and your help in this project.

Furthermore, I'd like to thank the people who helped out with measurements or general technical guidance: *Nadine Mill* was always there when help was needed, not limited to chemical preparations in the lab. *Karsten Rott* helped in preparing the FIB images of the SERS beads and was always there to answer technical questions concerning the lab equipment. *Markus Schäfers* introduced me to the UV laser lithography setup. Being the person in charge of an equipment that tends to break more than the Most Broken Equipment (MBE) is not a fun job, so I have to thank him all the more for investing a lot of work in a machine that was so vital for my projects. *Fabian Schmid-Michels* and *Peter Hedwig* developed the Helmholtz coil setup that was used in some of the experiments in this work. May it rest in pieces. I promise, I'll make a new one. *Lena Böhling* from the PC1 group supplied the knowledge and the means for the absorption spectroscopy measurements that were performed within the scope of this work. Last, but definitely not least, there were *Elina Oberlander* and her supervisor *Thomas Huser*. I have to thank Elina for being a kind and motivated contributor to the SERS chapter of this work. Without her knowledge and work in the area of SERS spectroscopy, this project would not have been possible. The same goes for Thomas, who was of more help in answering questions and arranging helpful contacts to third parties than I could have wished for.

I already mentioned the animus project, the eLearning project I did as a side project to my PhD thesis, and I would like to thank the people who helped me realize this project. First of all, there were *Florian Sprengel* and *Felix Selzer* who were wonderful, dedicated co-workers. Their ideas, critique and their skills were essential assets to the project. *Anne Reh* and *Marvin Kronsbein* also contributed a lot to this project within the scope of their bachelor theses, and the whole project would not have been possible without the financial aid that was organized by the *chemistry department*, the *service center media* and the *SL_K5* department.

One of the things I came to enjoy most over the course of the three years in the group was the wonderful, companionable atmosphere in my office. For this I would like to thank *Annalena Wolff*, *Dieter Akemeier*, *Daniel Kappe*, *Fabian Schmid-Michels*, *Jennifer-Rose Schubert* and *Thomas Weiß*. Further thanks go to *Alexander Auge*: He has been a wonderful co-worker, roommate and friend for 7 years. Without him, I would never have had

the idea of joining the microfluidics (and actually would probably not have studied in Bielefeld, but that's another story). To all of you: Wherever the journey will lead me, it will not be the same without you by my side.

Last, but most definitely not least, I would like to thank my family, consisting of my mother *Elke*, my grandfather *Ferdinand* and my grandmother *Hilde* as well as my life companion *Lisa Kuhlmann* for their support. Lisa probably needed a lot of patience during the time that I spent writing this thesis. And she had it. Thank you, you were wonderful!

"Touch a scientist and you touch a child."
Ray Bradbury

Bibliography

[1] A. Manz, N. Graber, and H.M. Widmer. Miniaturized total chemical analysis systems: A novel concept for chemical sensing. *Sensors and Actuators B: Chemical*, 1(1-6):244–248, 1990. URL `http://linkinghub.elsevier.com/retrieve/pii/092540059080209I`.

[2] S.C. Jacobson, R. Hergenroder, A.W. Moore, and J.M. Ramsey. Precolumn reactions with electrophoretic analysis integrated on a microchip. *Analytical Chemistry*, 66:4127–4132, 1994.

[3] D.R. Reyes, D. Iossifidis, P.A. Auroux, and A. Manz. Micro total analysis systems. 1. introduction, theory, and technology. *Analytical Chemistry*, 74:2623–2636, 2002.

[4] D.J. Beebe, G.A. Mensing, and G.M. Walker. Physics and applications of microfluidics in biology. *Annual Review of Biomedical Engineering*, 4:261–286, 2002.

[5] J.C. McDonald and G.M. Whitesides. Poly(dimethylsiloxane) as a material for fabricating microfluidic devices. *Accounts of Chemical Research*, 35:491–499, 2002.

[6] J.C. McDonald, D.C. Duffy, J.R. Anderson, D.T. Chiu, H. Wu, O.J.A. Schueller, and G.M. Whitesides. Fabrication of microfluidic systems in poly(dimethylsiloxane). *Electrophoresis*, 21:27–40, 2000.

[7] S.K. Sia and G.M. Whitesides. Microfluidic devices fabricated in poly(dimethylsiloxane) for biological studies. *Electrophoresis*, 24: 3563–3576, 2003.

[8] D.C. Duffy, J.C. McDonald, O.J.A. Schueller, and G.M. Whitesides. Rapid prototyping of microfluidic systems in poly(dimethylsiloxane). *Analytical Chemistry*, 70:4974–4984, 1998.

[9] M.M. Stephan. Survival in the microfluidics market. *The Scientist*, 18:38–40, 2004.

[10] P. Gould. Microfluidics realizes potential. *Materials Today*, 7:48–52, 2004.

[11] N. Blow. Microfluidics: in search of a killer application. *Nature Methods*, 4:666–670, 2007.

[12] H. Becker. It's the economy... *Lab on a Chip*, 9:2759–2763, 2009.

[13] E. Verpoorte. Beads and chips: new recipes for analysis. *Lab on a Chip*, 3:60N–68N, 2003.

[14] P.J. Halling, R.V. Ulijin, and S.L. Flitsch. Understanding enzyme reaction on immobilised substrates. *Current Opinion in Biotechnology*, 16:385–392, 2005.

[15] S.A. Peyman, A. Iles, and N. Pamme. Mobile magnetic particles as solid-supports for rapid surface-based bioanalysis in continuous flow. *Lab on a Chip*, 9:3110–3117, 2009.

[16] N. Pamme. Magnetism and microfluidics. *Lab on a Chip*, 6:24–28, 2005.

[17] M. Karle, J. Miwa, G. Czilwik, V. Auwärter, G. Roth, R. Zengerle, and FF von Stetten. Continuous microfluidic dna extraction using phase-transfer magnetophoresis. *Lab on a Chip*, 10:3284–3290, 2010.

[18] B.B. Yellen, R.M. Erb, H.S. Son, R. Hewlin, H. Shang, and G.U. Lee. Traveling wave magnetophoresis for high resolution chip based separations. *Lab on a Chip*, 7:1681–1688, 2007.

[19] N. Pamme, J.C. Eijkel, and A. Manz. On-chip free-flow magnetophoresis: Separation and detection of mixtures of magnetic particles in

continuous flow. *Journa of Magnetism and Magnetic Materials*, 307: 237–244, 2006.

[20] D. Robert, N. Pamme, H. Conjeaud, F. Gazeau, A. Iles, and C. Wilhelm. Cell sorting by endocytotic capacity in a microfluidic magnetophoresis device. *Lab on a Chip*, 11:1902–1910, 2011.

[21] G. Reiss, H. Brückl, A. Hütten, J. Schotter, M. Brzeska, M. Panhorst, and D. Sudfeld. Magnetoresistive sensors and magnetic nanoparticles for biotechnology. *Journal of Materials Research*, 20:3294–3302, 2005.

[22] F. Li, C. Gooneratne, and J. Kosel. Magnetic biosensor system to detect biological targets. In *Proceedings of the 2012 International Conference on Electromagnetics in Advanced Applications*, pages 1238–1241, Cape Town, South Africa, Sept 2012.

[23] D.R. Baselt, G.U. Lee, M. Natesan, S.W. Metzger, P.E. Sheehan, and R.J. Colton. A biosensor based on magnetoresistive technology. *Biosensors and Bioelectronics*, 13:731–739, 1998.

[24] R.L. Edelstein, C.R. Tamanaha, P.E. Sheehan, M.M. Miller, D.R. Baselt, L.J. Whitman, and R.J. Colton. The barc biosensor applied to the detection of biological warfare agents. *Biosensors and Bioelectronics*, 14:805–813, 2000.

[25] J. Schotter, P.B. Kamp, A. Becker, A. Pühler, G. Reiss, and H. Brückl. Comparison of a prototype magnetoresistive biosensor to standard fluorescent dna detection. *Biosensors and Bioelectronics*, 19:1149–1156, 2004.

[26] M. Koets, T. van der Wijk, J.T.W.M. van Eemeren, A. van Amerongen, and M.W.J. Prins. Rapid dna multi-analyte immunoassay on a magneto-resistance biosensor. *Biosensors and Bioelectronics*, 24: 1893–1898, 2009.

[27] M. Mujika, S. Arana, E. Castano, M. Tijero, R. Vilares, J.M. Ruano-López, A. Cruz, L. Sainz, J.Magnetoresistive immunosensor for the

detection of Escherichia coli O157:H7 including a microfluidic network. Biosensors Berganza, and 1253-1258. Bioelectronics 2009, 24. Magnetoresistive immunosensor for the detection of escherichia coli o157:h7 including a microfluidic network. *Biosensors and Bioelectronics*, 24:1253–1258, 2009.

[28] A. Manteca, M. Mujika, and S. Arana. Gmr sensors: Magnetoresistive behavior optimization for biological detection by means of superparamagnetic nanoparticles. *Biosensors and Bioelectronics*, 26: 3705–3709, 2011.

[29] G.X. Li, V. Joshi, R.L. White, S.X. Wang, J.T. Kem, C. Webb, R.W. Davis, and S.H. Sun. Detection of single micron-sized magnetic bead and magnetic nanoparticles using spin valve sensors for biological applications. *Journal of Applied Physics*, 93:7557–7559, 2003.

[30] D.L. Graham, H. Ferreira, J. Bernardo, P.P. Freitas, and J.M.S. Cabral. Single magnetic microsphere placement and detection on-chip using current line designs with integrated spin valve sensors: Biotechnological applications. *Journal of Applied Physics*, 91:7786–7788, 2002.

[31] L. Lagae, R. Wirix-Speetjens, J. Das, D. Graham, H. Ferreira, P.P.P. Freitas, and G. Borghs. On-chip manipulation and magnetization assessment of magnetic bead ensembles by integrated spin-valve sensors. *Journal of Applied Physics*, 91:7445–7447, 2002.

[32] P.A. Besse, G. Boero, M. Demierre, V. Pott, and R. Popovic. Detection of a single magnetic microbead using a miniaturized hall sensor. *Applied Physics Letters*, 80:4199–4201, 2002.

[33] D. Karnaushenko, D. Makarov, Y. Chenglin, R. Streubel, and O.G. Schmidt. Printable giant magnetoresistive devices. *Advanced Materials*, 24:4518–4522, 2012.

[34] D.L. Graham, H.A. Ferreira, and P.P. Freitas. Magnetoresistive-based biosensors and biochips. *Trends in Biotechnology*, 22:455–462, 2004.

[35] M.A.M. Gijs, F. Lacharme, and U. Lehmann. Microfluidic applications of magnetic particles for biological analysis and catalysis. *Chemical Rev*, 110:1518–1563, 2010.

[36] F. Wittbracht, A. Weddemann, B. Eickenberg, and A. Hütten. On the direct employment of dipolar particle interaction in microfluidic systems. *Microfluidics and Nanofluidics*, 13:543–554, 2012.

[37] F. Wittbracht, B. Eickenberg, A. Weddemann, and A. Hütten. Towards a programmable microfluidic valve: Formation dynamics of two-dimensional magnetic bead arrays in transient magnetic fields. *Journal of Applied Physics*, 109:114503, 2011.

[38] F. Lacharme, C. Vandevyver, and M.A.M. Gijs. Magnetic beads retention device for sandwich immunoassay: comparison of off-chip and on-chip antibody incubation. *Microfluidics and Nanofluidics*, 7: 479–487, 2009.

[39] G. Helgesen, A.T. Skjeltorp, P.M. Mors, R. Botet, and R. Jullien. Aggregation of magnetic microspheres: Experiments and simulations. *Physical Review Letters*, 61:1736–1739, 1988.

[40] A.K. Vuppu, A.A. Garcia, M.A. Hayes, K. Booksh, P.E. Phelan, R. Calhoun, and S.K. Saha. Phase sensitive enhancement for biochemical detection using rotating paramagnetic particle chains. *Journal of Applied Physics*, 96:6831–6838, 2004.

[41] S. Melle, O.G. Calderon, M.A. Rubio, and G.G. Fuller. Microstructure evolution in magnetorheological suspensions governed by mason number. *Physical Review E*, 68:041503, 2003.

[42] I. Petousis, E. Homburg, R. Derks, and A. Dietzel. Transient behaviour of magnetic micro-bead chains rotating in a fluid by external fields. *Lab on a Chip*, 7:1746–1751, 2007.

[43] A. Weddemann, F. Wittbracht, B. Eickenberg, and A. Hütten. Magnetic field induced assembly of highly ordered two-dimensional particle arrays. *Langmuir*, 26:19225–19229, 2010.

[44] S. Jäger, H. Schmidle, and S.H.L. Klapp. Non-equilibrium condensation and coarsening of field-driven dipolar colloids. *Physical Review E*, 86:011402, 2012.

[45] M.A.M. Gijs. Magnetic bead handling on-chip: new opportunities for analytical applications. *Microfluidics and Nanofluidics*, 1:22–40, 2004.

[46] A. Weddemann, F. Wittbracht, A. Auge, and A. Hütten. Particle flow control by induced dipolar interaction of superparamagnetic microbeads. *Microfluidics*, 10:459–463, 2011.

[47] A. Rida and M.A.M. Gijs. Manipulation of self-assembled structures of magnetic beads for microfluidic mixing and assaying. *Analytical Chemistry*, 76:6239–6246, 2004.

[48] S.H. Lee, D. van Noort, J.Y. Lee, B.T. Zhang, and T.H. Park. Effective mixing in a microfluidic chip using magnetic particles. *Lab on a Chip*, 9:479–482, 2008.

[49] R.J. Derks, A.J. Frijns, M.W. Prins, and A. Dietzel. Multibody interactions of actuated magnetic particles used as fluid drivers in microchannels. *Microfluidics and Nanofluidics*, 9:357–364, 2010.

[50] H. Bruus. *Theoretical microfluidics*. Oxford University Press, 2011.

[51] F. Boyer and P. Fabrie. *Mathematical Tools for the Study of the Incompressible Navier-Stokes Equations and Related Models*. Springer, 2013.

[52] R.K. Zeytounian. *Navier-Stokes-Fourier equations: a rational asymptotic modelling point of view*. Springer, 2012.

[53] P.G. Drazin and N. Riley. *The Navier-Stokes equations: a classification of flows and exact solutions*. Cam, 2006.

[54] P. Tabeling. *Introduction to Microfluidics*. Oxford University Press, 2005.

[55] J.P. Brody, P. Yager, R.E. Goldstein, and R.H. Austin. Biotechnology at low reynolds numbers. *Biophysical Journal*, 71:3430–3441, 1996.

[56] L. Capretto, W. Cheng, M. Hill, and X. Zhang. Micromixing within microfluidic devices. *Topics in Current Chemistry*, 304:27–68, 2011.

[57] J. Ottino and S. Wiggins. Introduction: mixing in microfluidics. *Philosophical Transactions A*, 362:923–35, 2004.

[58] E.A. Mansur, M. Ye, Y.D. Wang, and Y.Y. Dai. A state-of-the-art review of mixing in microfluidic mixers. *Chinese Journal of Ch*, 16: 503–516, 2008.

[59] J.B. Knight, A. Vishwanath, J.P. Brody, and R.H. Austin. Hydrodynamic focusing on a silicon chip: Mixing nanoliters in microseconds. *Physical Review Letters*, 80:3863–3866, 1998.

[60] C. Erbacher, F. Bessoth, M. Busch, E. Verpoorte, and A. Manz. Towards integrated continuous-flow chemical reactors. *Microchimica Acta*, 131:19–24, 1999.

[61] P. Lob, K. Drese, V. Hessel, S. Hardt, C. Hofmann, H. Löwe, R. Schenk, F. Schönfeld, and B. Werner. Steering of liquid mixing speed in interdigital micro mixers-from very fast to deliberately slow mixing. *Chemical Engineering & Technology*, 27:340–345, 2004.

[62] J. Ottino. *The Kinematics of Mixing: Streching, Chaos and Transport*. Cambridge University Press, 1989.

[63] A.D. Stroock, S.K.W. Dertinger, A. Ajdari, I. Mezic, H.A. Stone, and G.M. Whitesides. Chaotic mixer for microchannels. *Science*, 295: 647–651, 2002.

[64] N.T. Nguyen and Z. Wu. Micromixers-a review. *Journal of Micromechanics and Microengineering*, 15:R1–R16, 2005.

[65] V. Hessel, H. Löwe, and F. Schönfeld. Micromixers-a review on passive and active mixing principles. *Chemical Engineering Science*, 60:2479–2501, 2005.

[66] Z. Yang, S. Matsumoto, H. Goto, M. Matsumoto, and R. Maeda. Ultrasonic micromixer for microfluidic systems. *Sensors and Actuators A: Physical*, 93:266–272, 2001.

[67] H.H. Bau, J. Zhong, and M. Yi. A minute magneto hydro dynamic (mhd) mixer. *Sensors and Actuators B*, 79:207–215, 2001.

[68] Z. Wu and N.T. Nguyen. Convective-diffusive transport in parallel lamination micromixers. *Microfluidics and Nanofluidics*, 1:208–217, 2005.

[69] M. Zborowski, S. Liping, L.R. Moore, P.S. Williams, and J.J. Chalmers. Continuous cell separation using novel magnetic quadrupole flow sorter. *Journal of Magnetism and Magnetic Materials*, 194:224–230, 1999.

[70] C. Liu, T. Stakenborg, S. Peeters, and L. Lagae. Cell manipulation with magnetic particles toward microfluidic cytometry. *Journal of Applied Physics*, 105:102014, 2009.

[71] N.T. Nguyen. Micro-magnetofluidics: interactions between magnetism and fluid flow on the microscale. *Microfluidi*, 12:1–16, 2012.

[72] I Ennen. *Magnetische Nanopartikel als Bausteine für granulare Systeme: Mikrostruktur, Magnetismus und Transporteigenschaften.* PhD thesis, Bielefeld University, 2008.

[73] G. Fonnum, C. Johansson, A. Molteberg, S. Morup, and E. Aksnes. Characterisation of dynabeads by magnetization measurements and mössbauer spectroscopy. *Journa of Magnetism and Magnetic Materials*, 293:41–47, 2005.

[74] T. Deng, G.M. Whitesides, M. Radhakrishnan, G. Zabow, and M. Prentiss. Manipulation of magnetic microbeads in suspension using micromagnetic systems fabricated with soft lithography. *Applied Physics Letters*, 78:1775–1777, 2001.

[75] C.S. Lee, H. Lee, and R.M. Westervelt. Microelectromagnets for the control of magnetic nanoparticles. *Applied Physics Letters*, 79: 3308–3310, 2001.

[76] S. Ostergaard, G. Blankenstein, H. Dirac, and O. Liestiko. A novel approach to the automation of clinical chemistry by controlled manipulation of magnetic particles. *Journal of Magnetism and Magnetic Materials*, 194:156–162, 1999.

[77] A. Sinha, R. Ganguly, and I.K. Puri. Magnetic separation from superparamagnetic particle suspensions. *Journal of Magnetism and Magnetic Materials*, 321:2251–2256, 2009.

[78] A. Weddemann, F. Wittbracht, A. Auge, and A. Hütten. A hydrodynamic switch: Microfluidic separation system for magnetic beads. *Applied Physics Letters*, 94:173501:1–173501:3, 2009.

[79] V. Kourilov and M. Steinitz. Magnetic-bead enzyme-linked immunosorbent assay verifies adsorption of ligand and epitope accessibility. *Analytical Biochemistry*, 311:166–170, 2002.

[80] S. Miltenyi, W. Müller, W. Weichel, and A. Radbruch. High gradient magnetic cell separation with macs. *Cytometry*, 11:231–238, 1990.

[81] J. Meyer, T. Rempel, M. Schäfers, F. Wittbracht, C. Müller, A.V. Patel, and A. Hütten. Giant magnetoresistance effects in gel-like matrices. *Smart Materials and Structures*, 22:025032, 2013.

[82] E.M. Furst and A.P. Gast. Micromechanics of dipolar chains using optical tweezers. *Physical Review Letters*, 82:4130–4133, 1999.

[83] S. Melle, O.G. Calderon, G.G. Fuller, and M.A. Rubio. Polarizable particle aggregation under rotating magnetic fields using scattering dichroism. *Journal of Colloid and Interface Science*, 247:200–209, 2002.

[84] U. Sahoo, A.K. Seth, and R. Chawla. *UV/Visible Spectroscopy: Absorption Spectroscopy*. Lambert Academic Publishing, 2012.

[85] J.M. Hollas. *Modern Spectroscopy.* Jon Wiley & Sons, 2003.

[86] G. Gauglitz and D.S. Moore, editors. *Handbook of Spectroscopy.* Wiley-VCH, 2014.

[87] P. Vandenablee. *Practical Raman Spectroscopy: An Introduction.* John Wiley & Sons, 2013.

[88] D.A. Long. *Raman Spectroscopy.* McGraw Hill Higher Education, 1977.

[89] C.V. Raman. A new radiation. *Indian Journal of Physics*, 2:387–398, 1928.

[90] K. Kneipp, H. Kneipp, I. Itzkan, R.R. Dasari, and M.S. Feld. Surface-enhanced raman scattering and biophysics. *Journal of Physics: Condensed Matter*, 14:R597–R624, 2002.

[91] E.C. Le Ru, E. Blackie, M. Meyer, and P.G. Etchegoin. Surface enhanced raman scattering enhancement factors: A comprehensive study. *Journal of Physical Chemistry C*, 111:13794–13803, 2007.

[92] E. Le Ru and P. Etchegoin. *Principles of Surface Enhanced Raman Spectroscopy and Related Plasmonic Effects.* Elsevier, 2009.

[93] M. Fleischmann, P.J. Hendra, and A.J. McQuillan. Raman spectra of pyridine adsorbed at a silver electrode. *Chemical Physics Letters*, 26:163–166, 1974.

[94] D.L. Jeanmaire and R.P. van Duyne. Surface raman spectroelectrochemistry part i. heterocyclic, aromatic, and aliphatic amines adsorbed on the anodized silver electrode. *Journal of Electr*, 84:1–20, 1977.

[95] K. Kneipp, Y. Wang, H. Kneipp, L.T. Perelman, I. Itzkan, R.R. Dasari, and M. Feld. Single molecule detection using surface-enhanced raman scattering (sers). *Physical Review Letters*, 78:1667–1670, 1997.

[96] S. Nie and S.R. Emory. Probing single molecules and single nanoparticles by surface-enhanced raman scattering. *Science*, 275:1102–1106, 1997.

[97] K. Kneipp, H. Kneipp, V.B. Kartha, R. Manoharan, G. Deinum, I. Itzkan, R.R. Dasari, and M.S. Feld. Detection and identification of a single dna base molecule using surface-enhanced raman scattering (sers). *Physical Review E*, 57:R6281–R6284, 1998.

[98] A.M. Michaels, M. Nirmal, and L.E. Brus. Surface enhanced raman spectroscopy of individual rhodamine 6g molecules on large ag nanocrystals. *Journal of the American Chemical Society*, 121: 9932–9939, 1999.

[99] G. McNay, D. Eustace, W.E. Smith, K. Faulds, and D. Graham. Surface-enhanced raman scattering (sers) and surface-enhanced resonance raman scattering (serrs): A review of applications. *Applied Spectroscopy*, 65:825–37, 2011.

[100] P. Hildebrandt and M. Stockburger. Surface-enhanced resonance raman-spectroscopy of rhodamine-6g adsorbed on colloidal silver. *Journal of Physical Chemistry*, 88:5935–5944, 1984.

[101] J.A. Creighton, C.G. Blatchford, and M.G. Albrecht. Plasma resonance enhancement of raman-scattering by pyridine adsorbed on silver or gold sol particles of size comparable to the excitation wavelength. *Journal of the Chemical Society-Faraday Transactions*, 75:790–798, 1979.

[102] C.G. Blatchford, J.R. Campbell, and J.A. Greighton. Plasma resonance enhanced raman-scattering by adsorbates on gold colloids - the effects of aggregation. *Surface Science*, 120:435–455, 1982.

[103] K.C. Grabar, K.R. Brown, C.D. Keating, S.J. Stranic, S.L. Tang, and M.J. Natan. Nanoscale characterization of gold colloid monolayers: A comparison of four techniques. *Analytical Chemistry*, 69:471–477, 1997.

[104] A.C. Curtis, D.G. Duff, P.P. Edwards, D.A. Jefferson, B.F.G. Johnson, A.I. Kirkland, and A.S. Wallace. Preparation and structural characterisation of an unprotected copper sol. *Journal of Ph*, 92: 2270–2275, 1988.

[105] H.H. Huang, F.Q. Yan, Y.M. Kek, C.H. Chew, G.Q. Xu, W. Ji, P.S. Oh, and S.H. Tang. Synthesis, characterization, and nonlinear optical properties of copper nanoparticles. *Langmuir*, 13:172–175, 1997.

[106] M. Moskovits. Surface-enhanced spectroscopy. *Reviews of Modern Physics*, 57:783–826, 1985.

[107] J. Friend and L. Yeo. Fabrication of microfluidic devices using polydimethylsiloxane. *Biomicrofluidics*, 4:026502, 2010.

[108] J. Ng, I. Gitlin, A. Stroock, and G.M. Whitesides. Components for integrated poly(dimethylsiloxane) microfluidic systems. *Electrophoresis*, 23:3461–3473, 2002.

[109] W. Hellmich. *Einzelzellanalytik in Mikrofluidik-Systemen*. PhD thesis, Bielefeld University, 2006.

[110] Avidemux. URL `http://avidemux.sourceforge.net/`.

[111] W. Rasband. Imagej. URL `http://rsbweb.nih.gov/ij/`.

[112] E. Meijering, O. Dzyubachyk, and I. Smal. Methods for cell and particle tracking. *Methods in Enzymology*, 504:183–200, 2012.

[113] F.C. Frank. Supercooling of liquids. *Proceedings of the Royal Society of London, Series A*, 215:43–46, 1952.

[114] E.K. Bigg. The supercooling of water. *Proceedings of the Physical Society, Section B*, 66:688–694, 1953.

[115] T. Koop, B. Luo, A. Tsias, and T. Peter. Water activity as the determinant for homogeneous ice nucleation in aqueous solutions. *Letters to nature*, 406:611–614, 2000.

[116] B. Riechers, F. Wittbracht, A. Hütten, and T. Koop. The homogeneous ice nucleation rate of water droplets produced in a microfluidic device and the role of temperature uncertainty. *Physical Chemistry & Chemical Physics*, 15:5873–5887, 2013.

[117] B. Eickenberg, F. Wittbracht, P. Stohmann, J.R. Schubert, C. Brill, A. Weddemann, and A. Hütten. Continuous-flow particle guiding based on dipolar coupled magnetic superstructures in rotating magnetic fields. *Lab on a Chip*, 13:920–927, 2013.

[118] B. Eickenberg, F. Wittbracht, A. Hütten, and A. Weddemann. Utilization of self-assembling, free-flowing superstructures of superparamagnetic beads for enhanced mixing and colloidal separation. In *Proceedings of the Fifth International Conference on Quantum, Nano and Micro Technologies*, pages 94–98, Nice/Saint Laurent du Var, France, August 21-27 2011. IARIA.

[119] F. Wittbracht. *Interaction of magnetic beads in microfluidic systems: fundamentals and applications.* PhD thesis, Bielefeld University, 2012.

[120] F. Wittbracht, A. Weddemann, B. Eickenberg, M. Zahn, and A. Hütten. Enhanced fluid mixing and separation of magnetic bead agglomerates based on dipolar interaction in rotating magnetic fields. *Applied Physics Letters*, 100:123507, 2012.

[121] L. Radoszkowicz, I. Presiado, Y. Erez, E. Nachliel, D. Huppert, and M. Gutman. Time-resolved emission of flavin adenine dinucleotide in water and water-methanol mixtures. *Physical Chemistry Chemical Physics*, 13:12058–12066, 2011.

[122] R. Jin, G. Wu, Z. Li, C.A. Mirkin, and G.C. Schatz. What controls the melting properties of dna-linked gold nanoparticle asssemblies? *Journal of the American Chemical Society*, 125:1643–1654, 2003.

[123] R. Dreyfus, M.E. Leunissen, R. Sha, A.V. Tkachenko, N.C. Seeman, D.J. Pine, and P.M. Chaikin. Simple quantitative model for the reversible association of dna coated colloids. *Physical Review Letters*, 102:048301, 2009.

[124] P. Herdewijn, editor. *Oligonucleotide Synthesis: Methods and Applications*. Humana Press, 2010.

[125] M.J. Gait, editor. *Oligonucleotide Synthesis: A Practical Approach*. Oxford University Press, 1984.

[126] E. Ohtsuka. Nucleic acid synthesis and molecular recognition. *Journal of the Pharmaceutical Society of Japan*, 119:625–636, 1999.

[127] S. Iwai. Chemical synthesis of oligonucleotides containing damaged bases for biological studies. *Nucleosides, Nucleotides & Nucleic Acids*, 25:561–582, 2006.

[128] J. Zhang, Z. Sun, and B. Yang. Self-assembly of photonic crystals from polymer colloids. *Current Opinion in Colloid & Interface Science*, 14: 103–114, 2009.

[129] M.H. Kim, S.H. Im, and O.O. Park. Rapid fabrication of two- and three-dimensional colloidal crystal films via confined convective assembly. *Advanced Functional Materials*, 15:1329–1335, 2005.

[130] K.Q. Zhang and X.Y. Liu. In situ observation of colloidal monolayer nucleation driven by an alternating electric field. *Nature*, 429:739–743, 2004.

[131] R. Xie and X.Y. Liu. Epitaxial assembly and ordering of two-dimensional colloidal crystals. *Applied Physics Letters*, 92:083106, 2008.

[132] Z. Zheng, X. Lui, Y. Luo, B. Cheng, D. Zhang, Q. Meng, and Y. Wang. Pressure controlled self-assembly of high quality three-dimensional colloidal photonic crystals. *Applied Physics Letters*, 90:051910, 2007.

[133] H.L. Li and F. Marlow. Solvent effects in colloidal crystal deposition. *Chemistry of Materials*, 18:1803–1810, 2006.

[134] Y.G. Ko and D.H. Shin. Effects of liquid between colloidal spheres and evaporation temperature on fabrication of colloidal multilayers. *Journal of Physical Chemistry B*, 111:1545–1551, 2007.

[135] Y. Liu, J. Goebl, and Y. Yin. Templated synthesis of nanostructured materials. *Chemical Society Reviews*, 42:2610–2653, 2013.

[136] G. von Freymann, V. Kitaev, B.V. Lotsch, and G.A. Ozin. Bottom-up assembly of photonic crystals. *Chemical Society Reviews*, 42: 2528–2554, 2013.

[137] T. Ding, Z. Liu, and K. Song. Preparation of 3d photonic crystals. *Progress in Chemistry*, 20:1283–1293, 2008.

[138] S. Cabrini, A. Carpentiero, R. Kumar, L. Businaro, P. Candeloro, M. Prasciolu, A. Gosparini, C. Andreani, M. De Vittorio, T. Stomeo, and E. Di Fabrizio. Focused ion beam lithography for two dimensional array structures for photonic applications. *Microelectronic Engineering*, 78-79:11–15, 2005.

[139] S. Takahashi, K. Suzuki, M. Okano, M. Imada, T. Nakamori, Y. Ota, K.I. Susumu, and S. Noda. Direct creation of three-dimensional photonic crystals by a top-down approach. *Nature Materials*, 8: 721–725, 2009.

[140] Z. Wang, J. Zhang, J. Xie, Y. Yin, Z. Wang, H. Shen, Y. Li, J. Li, S.L.L. Cui, L. Zhang, H. Zhang, and B. Yang. Patterning organic/inorganic hybrid bragg stacks by integrating one-dimensional photonic crystals and microcavities through photolithography: Toward tunable colorful patterns as highly selective sensors. *ACS Applied Materials & Interfaces*, 4:1297–1403, 2012.

[141] K. Suzuki, K. Ishizaki, Y. Ota, and S. Noda. Surface modes of three-dimensional photonic crystals constructed using a top-down approach. *Optics Express*, 19:25651–25656, 2011.

[142] G.R. Yi, D.J. Pine, and S. Sacanna. Recent progress on patchy colloids and their self-assembly. *Journal of Physics*, 25:193101, 2013.

[143] Milam. V.T., A.L. Hiddessen, J.C. Crocker, D.J. Graves, and D.A. Hammer. Dna-driven assembly of bidisperse, micron-sized colloids. *Langmuir*, 19:10317–10323, 2003.

[144] P.H. Rogers, E. Michel, C.A. Bauer, S. Vanderet, D. Hansen, B.K. Roberts, A. Calvez, J.B. Crews, K.O. Lau, A. Wood, D.J. Pine, and P.V. Schwartz. Selective, controllable, and reversible aggregation of polystyrene latex microspheres via dna hybridization. *Langmuir*, 21: 5562–5569, 2005.

[145] C.A. Mirkin, R.L. Letsinger, R.C. Mucic, and J.J. Storhoff. A dna-based method for rationally assembling nanoparticles into macroscopic materials. *Nature*, 382:607–609, 1996.

[146] A.P. Alivisatos, K.P. Johnsson, X. Peng, T.E. Wilson, C.J. Loweth, M.P. Bruchez, and P.G. Schultz. Organization of 'nanocrystal molecules' using dna. *Nature*, 382:609–611, 1996.

[147] P.L. Biancaniello, A.J. Kim, and J.C. Crocker. Colloidal interactions and self-assembly using dna hybridization. *Physical Review Letters*, 94:058302, 2005.

[148] N. Geerts and E. Eiser. Flying colloidal carpets. *Soft Matter*, 6: 664–669, 2010.

[149] M. Bartke. Reversible clusterbildung durch dna-hybridisierung. Master's thesis, Universität Bielefeld, 2013.

[150] K. Sivashanar, W. Hu, P.W. Huber, G.H. Bernstein, and M. Lieberman. Direct molecular level measurements of the electrostatic properties of a protein surface. *PNAS*, 95:12961–12966, 1998.

[151] V. Sivagnanam, A. Sayah, C. Vandevyver, and M.A.M. Gijs. Micropatterning of protein-functionalized magnetic beads on glass using electrostatic self-assembly. *Sensors and Actuators B: Chemical*, 132: 361–367, 2008.

[152] C.E. Talley, L. Jusinski, C.W. Hollars, S.M. Lane, and T. Huser. Intracellular ph sensors based on surface-enhanced raman scattering. *Analytical Chemistry*, 76:7064–7068, 2004.

[153] S.B. Lee, K. Kim, and M.S. Kim. Surface-enhanced raman-scattering of ortho-mercaptobenzoic acid in silver sol. *Journal of Raman Spectroscopy*, 22:811–817, 1991.

[154] A. Michota and J. Bukowska. Surface-enhanced raman scattering (sers) of 4-mercaptobenzoic acid on silver and gold substrates. *Journal of Raman Spectroscopy*, 34:21–25, 2003.

[155] J.S. Suh and J. Kim. Three distinct geometries of surface-adsorbed carboxylate groups. *Journal of Raman Spectroscopy*, 29:143–148, 1998.

[156] M.J. Banholzer, J.E. Millstone, L. Qin, and C.A. Mirkin. Rationally designed nanostructures for surface-enhanced raman spectroscopy. *Tutorial Review*, 37:885–897, 2008.

[157] C.E. Talley, J.B. Jackson, C. Oubre, N.K. Grady, C.W. Hollars, S.M. Lane, T.R. Huser, P. Nordlander, and N.J. Halas. Surface-enhanced raman scattering from individual au nanoparticles and nanoparticle dimer substrates. *Nano Letters*, 5:1569–1574, 2005.

[158] G.L. Liu, Y. Lu, J. Kim, J.C. Doll, and L.P. Lee. Magnetic nanocrescents as controllable surface-enhanced raman scattering nanoprobes for biomolecular imaging. *Advanced Materials*, 17:2683–2688, 2005.

[159] B.M. Ross and L.P. Lee. Plasmon tuning and local field enhancement maximization of the nanocrescent. *Nanotechnology*, 19:275201, 2008.